EPFL

Thèse n° 8819

Impact of battery energy storage systems on the dynamic behavior of low-inertia power grids

Présentée le 10 décembre 2021

Faculté des sciences et techniques de l'ingénieur
Laboratoire des systèmes électriques distribués
Programme doctoral en énergie

pour l'obtention du grade de Docteur ès Sciences

par

Yihui ZUO

Acceptée sur proposition du jury

Prof. D. Dujic, président du jury
Prof. M. Paolone, Dr F. Sossan, directeurs de thèse
Prof. X. Guillaud, rapporteur
Prof. A. Monti, rapporteur
Dr S.-R. Cherkaoui, rapporteur

École
polytechnique
fédérale
de Lausanne

2021

We have found it of paramount importance that in order to progress,
we must recognize our ignorance and leave room for doubt.
Scientific knowledge is a body of statements of varying degrees of certainty
— some most unsure, some nearly sure, but none absolutely certain.

— Richard P. Feynman

To my parents

Acknowledgements

This thesis has been made possible thanks to the help and support of many people, whom I hereby want to acknowledge and thank.

Firstly, I would like to thank my supervisor Prof. Mario Paolone for the continuous support throughout my Ph.D. study and related researches, for your patience, motivation, and immense knowledge. Your insightful feedback pushed me to sharpen my thinking and brought my work to a higher level. Your intelligence and spirit of responsibility have always been an example for me as a researcher and as a person. Then, my sincere thanks to my co-supervisor Prof. Fabrizio Sossan for the support and advice during the years. You inspired me with perspectives and provided me with the tools that I needed to solve scientific problems. Your guidance helped me in all the time of research and writing of this thesis.

Then, I would like to offer my special thanks to Dr. Rachid Cherkaoui for all the scientific advice you gave me, but also for your enthusiasm and endless positiveness. I would like to extend my sincere thanks to the member of my Ph.D. committee, Prof. Antonello Monti, Prof. Guillaud Xavier, and Prof. Drazen Dujic, for their insightful comments that incented me to widen my research from various perspectives.

This thesis was carried out within the frame of the EU H2020 project "Optimal System-Mix Of flexibility Solutions for European electricity" (OSMOSE) and "the Swiss Centre for Competence in Energy Research on the Future Swiss Electrical Infrastructure (SCCER-FURIES). Their financial support is acknowledged.

I would like to express my thanks to my friends and colleagues. Your passionate enthusiasm inside and outside of work enriched my Ph.D. life. Particularly, I am grateful to Dr. Asja Derviškadić, Dr. Gugliemo Frig, Dr. Antonio Zecchino, and Dr. Zhao Yuan for their support and advice that inspired and enlightened my research, and to Dr. Mokhtar Bozorg, Giacomo Schiapparelli, Francesco Genrini, and Rahul Guptar, who I had the opportunity to collaborate with. I am grateful to my fellow labmates for the stimulating discussions and for all the fun we had: Dr. Marco Pignati, Dr. Emil Namor, Dr. Enrica Scolari, Dr. Andreas Kettner, Dr. Zhaoyang Wang, Mohsen Kalantar, Sherif Fahmy, Ji-Hyun Yi, Johanna Becker, Alexandra Karpillow, Plouton Grammatikos, Willem Lambrichts, Vladimir Sovljanski, Simone Rametti and anyone I forgot to mention.

I would also like to thank Dr. Guillaume Denis and Dr. Carmen Cardozo from Réseau de Transport d'Électricité (RTE) for insightful technical discussions and bringing the industry perspective into my research.

My sincere thanks to my basketball teammate and friend Ping Che for the wonderful time in different sports and the delicious food you brought with your fantastic cooking skills. To my friend and flatmate Xiaoyu Dai, thank you for sharing with me a lot of happy times. To my friends in Paris, thank you for bringing me to the adventure of snowboarding. Also, to all my friends in China, for all the precious time we had.

To Yu Wu, thank you simply for being in my life. You brighten my days with your kindness and strength.

Finally, my heartfelt gratitude goes to my beloved parents, Xuemei Feng and Yunlong Zuo, for your constant encouragement and unconditional support. Your love gives me the courage to explore the world and take any challenge in my life.

Abstract

The extensive deployment of non-synchronous generation determines a lower level of grid inertia resulting in deteriorated frequency containment performance and abnormal frequency excursions in case of contingency. This calls for identifying assets, controls, and relaying schemes capable to ensure acceptable grid frequency containment and dynamics satisfying the requirements of existing grid codes. A potential way to counterbalance this lack of inertia is to use large-scale battery energy storage systems (BESSs) since they provide large ramping rates and fast power control. As known, there are generally two main approaches to control converter-interfaced BESSs: *grid-following* and *grid-forming* controls. As BESSs may provide significant value to system frequency containment, it is of fundamental importance to quantitatively evaluate the dynamics of low-inertia power grids hosting large-scale BESSs. Within this context, it is also of importance to study the behavior of low-inertia power systems subsequent to large contingencies in order to develop appropriate under-frequency load shedding (UFLS) relaying schemes that may take advantage of nowadays distributed sensing technologies enabled by the Phasor Measurement Units (PMUs).

Framed within the EU H2020 project "Optimal System-Mix Of flexibility Solutions for European electricity," the Thesis first characterizes the interplay between converter-interfaced BESSs and low-inertia power grids and then provides quantitative assessments of system dynamics and quantifies the benefits associated with different control strategies of BESSs. For this purpose, state-of-the-art detailed dynamic simulation models of power grids, BESS, and controls are implemented on a real-time simulator for detailed numerical analyses. At first, contingency tests are conducted. The results verify the substantial influence of inertia reduction on post-contingency dynamics of power systems and quantitatively prove that converter-interfaced BESSs can effectively limit the frequency decreasing and damp the frequency oscillations. In addition, analyses on the grid voltages at the BESSs' point of common coupling (PCC) demonstrate the advantage of the grid-forming converter to sustain the PCC voltage during transients. Then, the proposed dynamic models are used for one-day-long simulations to assess the impact of converter-interfaced BESSs on the frequency containment of low-inertia power grids in normal operating conditions. For a practical operative context, a day-ahead schedule layer is considered where reserve levels for frequency containment and restoration are allocated considering the current practice required by European transmission system operators. Numerical analyses on suitably defined metrics applied to grid frequency show that the grid-forming control strategy outperforms the grid-following one, achieving better system frequency containment.

As large frequency excursions are more likely to occur due to decreased kinetic energy stored in rotating synchronous machines, fast adaptive UFLS schemes are necessary to secure low-inertia power systems under contingency. PMUs provide an effective tool to track the network state in any node of interest with reporting rates in tens of frames per second. In this respect, the Thesis proposes and validates two new UFLS schemes suitable for low-inertia power grids. The first scheme is a centralized UFLS that leverages PMU-fed situational awareness systems and is coupled with an Optimal Power Flow (OPF) problem. The OPF problem is formulated to constrain nodal voltages and branch currents in combination with a model capable of predicting the system response. The performance of the proposed method is assessed using numerical simulations of the fully modeled low-inertia power grids, demonstrating that the proposed OPF-UFLS can minimize the amount of load to be shed and, at the same time, ensure a safe trajectory of the system frequency, preventing nodal voltages and branch currents from violating their feasible limits. A comparison against the UFLS strategy recommended by the European Network of Transmission System Operators (ENTSO-E) shows that the proposed OPF-driven UFLS better exploits the benefits associated to the presence of a large-scale BESS. The second proposed scheme is an effective local UFLS and Load-Restoration (LR) scheme that relies on Rate-of-Change-of-Frequency (RoCoF) and frequency measurements provided by PMUs. Since accurate synchrophasor measurements are required for the proposed UFLS methods to exploit the anticipative property of RoCoF in detecting system large electromechanical transients, the Thesis finally studies the impact of synchrophasor estimation algorithms on the performance of RoCoF-based UFLS schemes. Two consolidated window-based synchrophasor estimation algorithms are considered, i.e., the Enhanced Interpolated DFT (e-IpDFT) and the Compressive Sensing-based Taylor-Fourier Model (cs-TFM), as representative approaches based on static and dynamic signal models, respectively. The obtained results confirmed the benefit of PMU-based RoCoF measurements for UFLS applications and demonstrated the significant impact of synchrophasor estimation algorithms on RoCoF-based applications.

Keyword: low-inertia power grids, frequency containment, system inertia, battery energy storage, power-electronics converter, controls, under-frequency load shedding, modeling, synchrophasor estimation algorithms, phasor measurement units, optimal power flow, rate-of-change-of-frequency, unit commitment, IEEE 39-bus, dynamic simulation,.

Résumé

Le déploiement massif de la production d'énergie électrique moyennant des systèmes non-synchrones conduit à une diminution du niveau globale de l'inertie du réseau électrique, il en résulte une détérioration des performances par rapport au confinement de la fréquence du système ainsi que des excursions de fréquence anormales en cas contingences. Cela nécessite d'identifier les atouts, les schémas de contrôle et de protection capables d'assurer un confinement de fréquence du réseau acceptable et une dynamique satisfaisant les exigences des grid codes existants. Une technologie capable de contrebalancer ce manque d'inertie consiste à utiliser des systèmes de stockage d'énergie sous forme de batterie à grande échelle (Battery Energy Storage Systems – BESS). Ils offrent des coefficients de variation (ramp rates) en puissance relativement élevés et un contrôle de puissance rapide. Comme on le sait, il existe généralement deux approches principales pour contrôler les BESSs interfacés aux réseaux AC à travers de convertisseur de puissance : le contrôle grid-following et le contrôle grid-forming. Comme les BESSs peuvent apporter une contribution significative au confinement de la fréquence du système, il est d'une importance fondamentale d'évaluer quantitativement la dynamique des réseaux électriques à faible inertie intégrant des BESS à grande échelle. Dans ce contexte, il est également important d'étudier le comportement des systèmes électriques à faible inertie suite à des contingences sévères afin de développer des schémas de relais de délestage de charge sous-fréquence (Under Frequency Load Shedding – UFLS) appropriés profitant notamment des avantages que pourraient offrir leur couplage à des Phasor Measurement Units (PMUs).

Dans le cadre du projet EU H2020 "Optimal System-Mix Of Flexibility Solutions for European electricity", la thèse étudie d'abord l'interaction entre les BESSs et les réseaux électriques à faible inertie. Ensuite, elle fournit des évaluations quantitatives de la dynamique du système et quantifie les avantages associés aux différentes stratégies de contrôle des BESS. Dans ce but, des modèles de simulation dynamique détaillés des composants et du système électrique, des BESSs et des commandes ont été développés et implémentés dans un simulateur en temps réel pour des analyses numériques détaillées. Dans un premier temps, des tests de contingence sont effectués. Les résultats confirment l'influence substantielle de la réduction de l'inertie sur la dynamique post-contingence des systèmes électriques et prouvent quantitativement que les BESSs peuvent efficacement limiter la diminution de fréquence et amortir ses oscillations. De plus, des analyses des tensions en relation avec les points de de couplage communs (Point of Common Coupling (PCC)) des BESSs démontrent l'avantage du convertisseur grid-forming pour maintenir la tension du PCC pendant les transitoires électromécaniques. Ensuite, les modèles dynamiques proposés sont utilisés pour des simulations d'une journée afin d'évaluer l'impact des BESSs sur le confinement en fréquence des réseaux électriques à faible inertie dans des conditions de fonctionnement normales. Dans un contexte opérationnel pratique, un horizon temporel journalier est considéré où les niveaux de réserve pour le confinement et le maintien de la fréquence sont définis compte tenu de la pratique actuelle suivie par les gestionnaires de réseau de transport européens ETNSO-E. Des analyses numériques sur des métriques convenablement définies et appliquées à la fréquence du réseau montrent que la stratégie de contrôle grid-forming surpasse celle du grid-folowing, ce qui permet d'obtenir un meilleur confinement de la fréquence du système.

Comme de grandes excursions de fréquence sont plus susceptibles de se produire en raison de la diminution de l'énergie cinétique stockée dans les machines synchrones tournantes, des schémas UFLS adaptatifs rapides sont nécessaires pour sécuriser les systèmes d'alimentation à faible inertie en cas d'urgence. Les PMUs fournissent une solution technologique efficace pour suivre l'état du réseau avec des fréquences de mesure de l'ordre de dizaines d'estimations par seconde. Dans ce contexte, la Thèse propose et valide deux nouveaux schémas UFLS adaptés aux réseaux électriques à faible inertie. Le premier système est un UFLS centralisé qui exploite la présence des estimateurs d'état (utilisant les mesures des PMUs) couplé à un modèle d'optimal power flow (OPF). Le problème OPF est formulé pour contraindre les tensions nodales et les courants de dérivation en combinaison avec un modèle capable de prédire la réponse du système. Les performances de la méthode proposée sont évaluées à l'aide de simulations numériques des réseaux électriques à faible inertie démontrant que l'OPF-UFLS proposé peut minimiser la quantité de charge à délester et, en même temps, assurer une trajectoire sûre de la fréquence du système, empêchant les tensions nodales et les courants des branches de dépasser leurs limites opérationnelles. Une comparaison avec la stratégie UFLS recommandée par le ENTSO-E montre que l'UFLS proposé exploite mieux les avantages associés à la présence d'un BESS à grande échelle. Le deuxième système proposé est composé d'un UFLS local et d'un schéma de Load Restoration (LR). Il repose sur les mesures du Rate-of-Change-of-Frequency (RoCoF) et les mesures de fréquence fournies par les PMUs. Étant donné que des mesures précises de synchrophaseurs sont nécessaires pour que les méthodes UFLS proposées exploitent la propriété anticipative du RoCoF dans la détection de grands transitoires électromécaniques du système, la thèse étudie l'impact des algorithmes d'estimation de synchrophaseurs sur les performances des schémas UFLS basés sur le RoCoF. Deux algorithmes consolidés d'estimation de synchrophaseurs sont considérés : la Enhanced Interpolated DFT (e-IpDFT) et le Compressive Sensing-based Taylor-Fourier Model (cs-TFM), en tant qu'approches représentatives basées sur des modèles de signaux statiques et dynamiques, respectivement. Les résultats obtenus ont confirmé l'avantage des mesures RoCoF basées sur les PMU pour les applications UFLS et ont démontré l'impact significatif des algorithmes d'estimation de synchrophaseurs sur les applications basées sur RoCoF.

Keyword : réseaux électriques à faible inertie, frequency containment, inertie du système, stockage d'énergie, batteries, convertisseurs électroniques de puissance, contrôles, délestage de charge à sous-fréquence, modélisation, algorithmes d'estimation de synchrophaseurs, phasor measurement units, optimal power flow, rate-of-change-of-frequency, unit committment, IEEE 39-bus, simulation dynamique.

Contents

List of Figures

List of Tables

1 Introduction

Context and Motivation

Power systems are rapidly evolving towards environmentally sustainable networks by accommodating substantial renewable power generation interfaced by power electronic converters. As broadly acknowledged in the power systems community, a large deployment of converter-interfaced generation (CIG) determines lower grid inertia levels and a decline of frequency containment delivered by conventional synchronous generators, posing challenges for the system's secure operation. Indeed, power systems not only have observed deteriorated frequency containment performance under normal operation condition [1], but also experienced extremely fast dynamics [2] in case of contingency associated to the lack of inertia and frequency containment response.

In this respect, network operators are motivated to incorporate additional assets with high power ramping capability to maintain adequate frequency containment performance. In recent years, Battery Energy Storage Systems (BESSs) have been advocated and increasingly deployed for grid frequency regulation, thanks to their large power ramping capacity, high round-trip efficiency, and commercial availability [3, 4]. BESSs interface with power systems through power converters, which can be controlled as either *grid-forming* or *grid-following* units. Even if most converter-interfaced resources are currently controlled as grid-following units [5, 6, 7], future low-inertia grids are advocated to host a substantial amount of grid-forming units providing support to both frequency/voltage regulation and system stability [8, 9]. Moreover, power systems are more likely to experience extremely fast frequency excursions under contingency due to the decline of system inertia power. This poses challenges to defense plans associated to Under Frequency Load shedding (UFLS) schemes as traditional UFLS relays are designed based on the assumption that synchronous generators are the dominant dynamic component of the power system.

Within this context, the Thesis characterizes the interaction between converter-interfaced BESSs and low-inertia power grids and provides quantitative assessments on dynamics of low-inertia power grids hosting large-scale BESSs. The assessments are conducted for both contingency and daily steady-state operation scenarios. Further, given the need of changing traditional UFLS schemes, the Thesis proposes and validates two advanced UFLS methods (one is centralized UFLS and another is local UFLS) suitable for low-inertia power grids. The benefits of BESSs and the impact of synchrophasor estimation algorithms on the effectiveness of UFLS schemes are also discussed in detail.

Thesis Outline

The Thesis is organized into seven main chapters and one appendix, whose content is summarized here below.

Chapter 2 reviews the state of the art of low-inertia power grids, with a particular emphasis on the deployment of BESSs providing frequency regulation and the demand for novel UFLS control schemes. As BESSs interfacing with power grids through power converters, the Chapter also recalls the classification of converters' controls.

Chapter 3 assesses the impact of converter-interfaced BESSs on the post-contingency dynamics of low-inertia grids. The Chapter quantitatively evaluates post-contingency dynamics of low-inertia power grids and compares responses of grid-forming and grid-following converter-interfaced BESSs. In addition, a sensitivity analysis of system frequency responses with respect to crucial converter control parameters is conducted.

Chapter 4 focuses on the impact of converter-interfaced BESSs on the frequency containment of low-inertia power grids under regular daily operation and compares the performance of the grid-forming with the grid-following control providing frequency containment to the system. The performance of system frequency containment is quantitatively assessed via 24-hour long time-domain simulations. In order to reproduce a practical operative context, a benchmark framework is proposed to couple a day-ahead schedule layer with the day-long simulation stage, where reserve levels for frequency containment and restoration are allocated considering the current practice of a Transmission System Operator (TSO) in Europe.

Chapter 5 formulates an Optimal Power Flow(OPF)-driven UFLS scheme for low-inertia power grids hosting large-scale BESSs. The proposed UFLS scheme is suitably coupled with an OPF problem that is properly defined to constrain nodal voltages and branch currents in combination with a model capable of predicting the frequency time-domain evolution along with asymptotic values of nodal voltages and branch currents. The performance of the proposed method is compared with the UFLS strategy recommended by the European Network of Transmission System Operators (ENTSO-E) in order to quantify its benefits. In addition, the potential benefit of large-scale BESSs on the power grid response when coupled with the proposed OPF-driven UFLS scheme is quantified.

Chapter 6 proposes an effective local UFLS and Load-Restoration (LR) scheme that relies on Rate-of-Change-of-Frequency (RoCoF) and frequency measurements provided by Phasor Measurement Units (PMUs). The Chapter investigates the impact of synchrophasor estimation algorithms implemented in PMUs on the behavior of the proposed local UFLS scheme. Two consolidated window-based synchrophasor estimation algorithms, as representative approaches of static and dynamic signal models, are compared with a focus on the appropriateness of using PMU-based RoCoF measurements.

Chapter 7 contains a summary of the main outcomes.

Appendix A presents details of dynamic models of IEEE 39-bus power systems.

Contributions

The original contribution of this Thesis are listed in the following.

- Full-replica dynamic simulation models of low-inertia large interconnected systems comprising a mix of rotating machines and converter-interfaced resources are proposed. Low-inertia IEEE 39-bus power grids are proposed as extensions of the original IEEE 39-bus benchmark system, where part of the synchronous generators is replaced by wind power plants to create a low-inertia configuration. The proposed models are created by including detailed dynamic models of all the devices to capture realistic responses of low-inertia power systems and their interaction with converter-interfaced BESSs. Converter-interfaced BESSs are modeled in detail such that the dynamics between the converter and the battery DC voltage response are considered. The proposed dynamic simulation models are implemented on a real-time simulator and made available open-source to the power systems community.
- The impact of converter-interfaced BESSs on the post-contingency dynamics of low-inertia power grids is identified. Numerical analyses for the contingency tests of the proposed low-inertia dynamic model are provided to validate the impact of inertia reduction and quantify the impact of converter-interfaced BESSs and their control laws on the post-contingency dynamics of low-inertia power grids. The dynamic interactions between converter-interfaced BESSs and low-inertia power grids are assessed to compare the post-contingency responses of grid-forming vs. grid-following converter-interfaced units. A detailed sensitivity analysis is presented to assess the influence of crucial parameters of converter controls on the post-contingency response of power converters.
- A quantitative comparison of the impact of grid-forming versus grid-following converter-interfaced BESS on the frequency containment of the low-inertia power is presented. A comprehensive benchmark framework that comprises a day-ahead schedule layer with procedures nowadays adopted by TSOs and a day-long real-time simulation stage is

proposed. It provides a way to assess the frequency containment performance of low-inertia power systems under normal daily operation. Numerical results are provided leveraging the proposed detailed dynamic model of the low-inertia 39-bus system, where fully characterized models of stochastic demand and generation are integrated.

- A centralized OPF-driven UFLS approach relying on PMU-fed system awareness is proposed and applied in a low-inertia power grid hosting large-scale BESSs. An accurate power system dynamic model is proposed, enabling the OPF-driven UFLS scheme to better predict the post-contingency frequency. Thanks to the accurate prediction of the system dynamics after large contingencies, the proposed OPF-UFLS can minimize the amount of load to be shed while satisfying all the grid constraints avoiding cascading relays tripping and blackouts. The performance of the proposed UFLS scheme is compared with the one recommended by the ENTSO-E to show its superiority. Furthermore, the benefit associated to the presence of a large-scale BESS is quantified.

- The impact of the synchrophasor estimation algorithms on RoCoF-based UFLS is evaluated. Following the analysis of the anticipatory property of RoCoF in detecting large electromechanical transients, an effective local UFLS and Load-Restoration scheme based on RoCoF and frequency measurements provided by PMUs is proposed. Two sets of RoCoF thresholds are considered to assess the impact of the parameter tuning on the load shedding results. The impact of the synchrophasor estimation algorithms is assessed by comparing two consolidated window-based synchrophasor estimators. In particular, the impact of the signal model (i.e., static or dynamic) and the window length on the action of RoCoF-based UFLS scheme outcomes are evaluated.

2 Review of the State-of-the-Art

Power systems are transitioning towards clean and environmentally sustainable infrastructures by accommodating substantial renewable power generation interfaced by converters. In 2020 in the European Union, 38% of gross electricity consumption was generated from renewable resources [10]. Particularly, wind and solar supplied 14% and 5% of Europe's electricity consumption, respectively. In Australia, the instantaneous penetration[1] of wind and solar generation has reached 45%, and it is expected to be larger than 75% by 2025 [2]. In the United States of America, the national installed capacity of renewable generation has reached 20% of the total power generation capacity, with the maximum hourly peak of utility-scale wind and solar generation reaching nearly 62.6% in the area operated by the California Independent System Operator (CAISO) and 54.3% in the area operated by the Electrical Reliability Council of Texas (ERCOT) [11].

The increasing penetration of CIG, and the displacement of conventional synchronous generators, have a widespread impact on power systems' operation and planning. TSOs have been observing a decline of system inertia and a lack of frequency containment delivered by conventional power plants [1, 12, 13]. In this context, system operators are motivated to incorporate additional assets with high power ramping capability in order to maintain adequate frequency containment performances [14, 15, 16]. BESSs, characterized by large power ramping rates, high round-trip efficiency, and commercial availability [3, 4], are advocated as a potential solution for grid frequency regulation. Indeed, utility-scale BESSs that can interface with interconnected power systems through grid-forming or grid-following converters are increasingly deployed in systems with a high share of renewable resources [17, 18, 19, 20].

Furthermore, in the presence of depleting inertial power, power systems are more likely to

[1] Instantaneous penetration of wind and solar is the half-hourly proportion of underlying demand that is met by wind and solar resources [2].

experience extreme and fast frequency excursions subsequent to contingencies, such that frequency containment reserves and even defense plans associated to UFLS schemes may fail to prevent the system from large blackouts [21]. In this respect, TSOs have reviewed their UFLS settings and approaches [21, 22, 23].

Within this context, this Chapter reviews the state of the art with respect to: (i) synchronous inertia and frequency containment response in power systems in presence of CIG, (ii) the importance of BESSs providing frequency control to low-inertia grids, (iii) the classification of converters' controls, and (iv) the necessity of updating UFLS control schemes.

2.1 Synchronous Inertia and Frequency Containment Response in Actual Power Systems in Presence of CIG

In synchronous machines, the turbines and rotating components exhibit mechanical inertia, hence they can store kinetic energy in the rotating masses. When synchronized with the interconnected system, the active power of synchronous machines is controlled through speed governors to regulate the system frequency. A load and generation disturbance is immediately served through the kinetic energy extracted from (or absorbed into) the rotating masses and is associated to the decrease (or increase) of the machine speed. Then, the rotational speed deviation is sensed by the speed governor that adjusts the mechanical power in real-time (seconds) to regulate the grid frequency near its nominal value (*frequency containment reserve*). On a slower time scale (minutes), *frequency restoration reserve intervenes* to regulate the frequency back to its nominal value. The Australian Energy Market Operator (AEMO) has observed that lower frequency containment provided by generators results in a lack of effective control of frequency under normal operating conditions [2]. CAISO has also observed a progressive deterioration of its frequency containment and restoration performance: the frequency response measure (FRM[2]) has steadily decreased from 263 MW/0.1 Hz in 2012 to 141 MW/0.1 Hz in 2016 [1]. In the case of contingency, the reduction of system inertia can lead to very fast system frequency excursions, as indicated in several TSO reports [21, 24, 25]. In this regard, system operators have been reviewing the requirement of system frequency responses, and exploring approaches and assets to preserve a reliable power system operations [26, 27, 28].

Converter-interfaced units utilize, instead, a fundamentally different set of technologies that manage the flow of power by controlling semiconductor devices at a fast timescale and do not contain any mechanical components or rotating masses. As the share of CIG becomes comparable to the one of synchronous generation in modern power systems, it becomes essential to consider these differences. In contrast to a synchronous generator with considerable kinetic energy stored in the rotating mass, CIG has a way small electric field

[2]The FRM, calculated in resources of MW/0.1Hz, is the change in net actual interchange on the inter-tie lines between the pre-event period (point A) and the stabilizing period after the event (point B) per 0.1 Hz of the frequency event measured between those two points.

energy stored in the converter DC side capacitor. The stored energy (E) for a device is usually normalized by the device's rated power (P_N) to be expressed in seconds, i.e., $H = E/P_N$, where H is known as the inertia constant of the device. For synchronous machines, H is typically in the order of 2 - 7 s, whereas for CIGs, the corresponding value is in the order of milliseconds. For this reason, a large installation of CIG in replacement of synchronous generators in an interconnected power system determines a low system inertia level.

Concerning frequency containment response, the dynamics of a traditional power system are associated with the synchronous generator prime mover controls. In this regard, the reduced capacity of synchronous generators poses a challenge to the definition and scheduling of adequacy frequency containment reserves, since renewable energy resources such as wind and solar have to operate de-loaded (thus continuously preserving a certain amount of power) when required to raise their generation to balance the load increase. Other essential assets for frequency containment response are BESSs, which are expected to play a crucial role in frequency regulation in power systems with high penetration of CIG. The adoption of BESSs to provide frequency regulation in low-inertia grids is discussed in Section 2.2.

2.2 On BESSs Providing Frequency Control to Low-inertia Grids

In the context framed in Section 2.1, BESSs, as fast-ramping devices, can provide fast frequency containment response and are advocated as a potential remedy for power grid frequency regulation [17, 18, 19, 20]. The integration of BESSs into power systems to provide energy and ancillary services is a relatively recent development. Recently installed large BESSs, like the 100 MW/129 MWh unit of the Hornsdale Power Reserve (HPR) in Australia [18] and the 300 MW/1200 MWh unit at Moss Landing in California [19], have shown the applicability of this technology in actual contexts. Furthermore, more than 18,000 MW of new battery energy storage capacity is currently in the ERCOT interconnection queue in addition to the existed 163 MW of battery energy capacity [20].

BESSs can provide highly flexible active and reactive power support with extremely fast response times due to lack of mechanical elements. The plant-level response time comprises the time of plant-level sensing, communication, and dispatch to individual inverters. Depending on when the event occurs during the control cycle, BESS developers conservatively estimate response times between 150-400 ms [17]. An example of the fast response of a BESS is the 1 MW/250kWh BESS commissioned at Hawi wind plant on the Hawaii Electric Light Company Grid [29]. This BESS can deliver 90% of the request set-point in 200 ms,with a power ramping rate of 4.5 MW/s.

The traditional approaches adopted to model power systems are based on the assumption that synchronous generators are the dominant dynamic component of the power system. As such, the system's response was considered to be driven by the (large) inertia of the synchronous machines, significantly limiting the RoCoF and the corresponding frequency nadir in case of contingencies. However, in power systems with high shares of converter-interfaced resources, the behavior of system response is also driven by converter control characteristics. Specifically, the early response of the system can be primarily impacted by the characteristics of the closed-loop control of converter-interfaced units, and the design of the converter controls may play an important role in determining the system dynamics.

In this regard, it is essential to study the impact of BESS and its converter control strategies on the grid frequency dynamics using a detailed model of a realistic low-inertia power system. Many publications discussed the impact of inertia reduction in power systems with significant penetration of renewable generation [30, 31, 32]. In contrast, few studies have attempted to assess the impact of BESSs and their controls on system dynamics using detailed models that consider the dynamic interactions between low-inertia power grids and converter-interfaced BESSs. The work in [33, 34] studies the impact of a BESS on grid frequency transients using a dynamic model of a simple low-inertia grid. However, the BESS is modeled as an ideal power source and falls short of capturing the dynamic interactions between the converter and the grid. In [35], BESS's and grid's dynamic models show that the BESS can reduce frequency oscillations after a disturbance. Yet, this work has not considered the possible influences of different converter controls.

2.3 Classification of Converters' controls

2.3.1 Definitions of Grid-following and Grid-forming Converters

There are generally two main approaches to achieve the power control for power converter-interfaced units: *grid-following* and *grid-forming* controls [36, 37, 38]. Here below recalls the definitions proposed in [36].

A grid-following unit is based on a power converter whose injected currents are controlled with a specific phase displacement with respect to the grid voltage at the point of common coupling (PCC). As a consequence, the knowledge of the fundamental frequency phasor of the grid voltage at the PCC is needed at any time for the correct calculation of the converter reference currents. The amplitude and angle of the reference currents with respect to the grid voltage phasor are properly modified by outer control loops to inject the required amount of active and reactive power. Figure 2.1a shows the classical structure of the grid-following control. The grid voltage angle $\tilde{\theta_g}$ is estimated thanks to a phase locked-loop (PLL) and used by the Park's transformation. The active current reference, $I_{d\ ref}$, is generated by an outer active power loop, where the frequency may participate in enabling frequency supporting (e.g., frequency containment response). The reactive current reference $I_{q\ ref}$ is the output of a reactive power loop, where voltage may participate in enabling voltage support. For the active and reactive current references (i.e., $I_{d\ ref}$ and $I_{q\ ref}$), the inner controller respectively generates the d- and q-axis components of the modulated voltage to be achieved by the converter.

A grid-forming unit is based on a power converter that controls the magnitude and angle of the voltage at the PCC. As a consequence, the knowledge of the fundamental frequency phasor

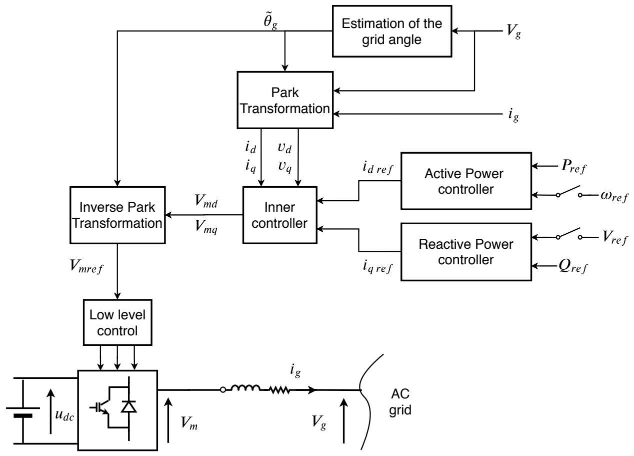

(a) General scheme of a grid-following control.

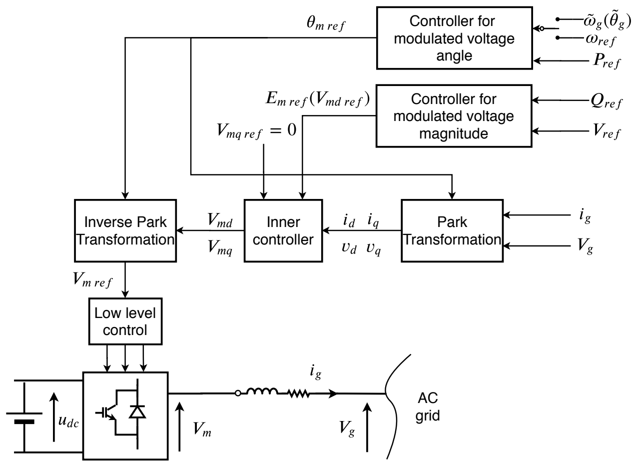

(b) General scheme of a grid-forming control.

Figure 2.1 – General schemes of grid-following and grid-forming controls adapted from [36].

of the grid voltage at the point of connection is not strictly necessary. In an isolated system, a grid-forming unit could behave itself like a slack-bus. When connected with other power sources, through an inductive line, the grid-forming converter controls the active power by modifying the modulated voltage angle, while the voltage magnitude is independent of the active power control. Figure 2.1b presents a general structure of the grid-forming control inspired by [36]. Since the active power is sensitive to the modulated voltage angle, the control has to generate an angle reference $\theta_{m\ ref}$ to control the active power. As shown in Figure 2.1b, the controller for the modulated voltage angle directly links the active power with the modulated voltage angle reference $\theta_{m\ ref}$, enabling the converter to control active power as well as deliver frequency containment response. It is worth noting that the controller for the modulated voltage angle does not strictly require the estimate of grid voltage angle $\tilde{\theta_g}$ or estimate of grid frequency $\tilde{\omega_g}$, which instead can be replaced by a constant frequency references ω_{ref}. With respect to the controller for modulated voltage magnitude, an easy way to control the voltage at the PCC is a simple reference on the d-axis, i.e., $V_{md\ ref} = E_{m\ ref}$ and $V_{mq\ ref} = 0$. In addition, voltage magnitude reference can be tuned to compensate the reactive power deviation from set-point Q_{ref}.

A BESS is connected to the power grid with a power converter that can be either controlled as a grid-following or a grid-forming unit. The Thesis focuses on assessing grid-forming vs grid-following converter-controlled BESS providing frequency containment reserve. Nevertheless, other resources may also be controlled as grid-forming or grid-following units to provide frequency containment reserve. For instance, voltage-source-converter high-voltage direct current (VSC-HVDC) transmission links allow one of the two terminal converters to implement grid-following [39] or grid-forming [40] controls to provide frequency regulation. Photo-voltaic (PV) and wind generation are still primarily relying on a grid-following control as it allows PV plants and wind turbines to easily implement maximum power point tracking controls. Nonetheless, some recent studies proposed grid-forming control schemes for two-stage PV systems [41] and Type-III/Type-IV wind turbines [42, 43]. It should also be noted that to provide a frequency containment service, PV and wind plants have to operate below their maximum power point.

The concept and characteristics of the grid-following and grid-forming converters are recalled in this Chapter in Section 2.3.

2.3.2 Progress of Converters' Controls

Grid-following controllers represent the most prevalent type of control strategy for grid-connected PV and wind turbines' inverters [5, 6, 7]. One of the limitations is that the grid-following converter work under the assumption that a stiff AC voltage at its PCC such that it can easily follow its local voltage and inject a controlled current [44]. Studies have shown that there are physical limitations to the highest PLL bandwidth of grid-following converters [45, 46]. Historically, this assumption holds relatively well as the share of CIG in interconnected power systems has been relatively small compared with conventional synchronous generators that provide sufficient frequency and voltage regulations.

In contrast to the grid-following control, whose concept has been widely accepted, several variants of control laws allowing the grid-forming capability have been recently proposed [47, 48]. Some new controllers have been proposed to make the converter behave like synchronous machine, e.g. Virtual Synchronous Generator (VSG) [49, 50, 51], Virtual Synchronous Machine (VSM) [52, 53], VISMA [54], Synchronverter [55, 56], droop-based control [57, 58]. Some of those controllers (e.g., VSG and VSM) use PLLs to decouple the power control from frequency control capability, while the droop-based controls are PLL-free. The benefit of using PLL-free controls is to avoid the stability issues caused by PLL and possibly the interaction between the PLL and power controller [59]. Another recently introduced grid-forming control law is the Virtual Oscillator (VOC) [60, 61]. It provides a way to synchronize and control the converter by acting as a non-linear oscillator. This control may be more advantageous in case of voltage unbalance and distortion due to its non-linear characteristics. However, its robustness of interacting with the grid, which comprises various generation resources (i.e., the mix of synchronous generations and power-electronics devices interfaced generations), has not yet been adequately studied and may be the subject of future studies. In this context, the droop-based PLL-free grid-forming controls are considered in this Thesis as it has been proved to be robust on a wide range of short circuit ratios (i.e., 1.2 to 20) [58, 62].

2.4 On the Under-Frequency Load Shedding Schemes

System inertia and frequency containment response are the initial responses in the power system to contain the frequency variation due to the imbalance between generation and load. In case of major contingency, for instance, due to a significant loss of generation, the system inertia and frequency containment reserves may not be sufficient to stabilize the system. Thus it requires the load shedding entering into action.

As known, UFLS is a technique that minimizes the risk of uncontrolled system separation, loss of generation, or shutdown in case of large power system disturbances, after the frequency containment reserve is exhausted [63]. Power systems with a large share of non-synchronous generation determining a low level of system inertia can lead to uncontrolled frequency excursion in case of contingency and consequently deteriorate the effectiveness of traditional UFLS schemes [21, 22]. In the 2016 South Australia blackout event, the loss of power in-feed from the wind farms and import from Victoria resulted in the system frequency falling so fast that load shedding schemes could not arrest the fall, resulting in a large blackout [21, 64]. Events described in [65, 66] also indicate that new, faster, and adaptive UFLS schemes are necessary since large frequency excursions are more likely to occur due to the decreasing system inertia. Moreover, these events have clearly documented the presence of line tripping associated to the violation of line ampacity limits subsequent to contingencies and the load shedding actions. In order to avoid such unintentional line tripping, UFLS schemes need to be coupled with Optimal Power Flow (OPF) and system situational awareness to maintain nodal voltages and branch currents within safety limits. In this context, it is necessary to explore adaptive and faster UFLS schemes for power systems in presence of large shares of non-synchronous renewable resources and investigate the potential benefit of BESSs to the effectiveness of UFLS controls.

The power systems literature has widely discussed the UFLS problem and proposed several solutions (e.g., [67]). Traditionally, UFLS plans solely rely on local frequency measurements and implement a pre-defined decision function (e.g., frequency thresholds vs the amount of shed loads) [68, 69]. As the frequency thresholds are network topology- and state-dependent, their setting is typically determined using simulation-based trial-and-error heuristics [70]. This approach neglects the dynamic contingency response and approximates the network via a purely static model [71]. In this context, PMUs provide an effective tool to track the network state in any node of interest with reporting rates in the order of tens of frames per second. The availability of such distributed measurement infrastructure has triggered the development of more sophisticated centralized [72, 73] and local [74] UFLS methods that exploit the frequency and RoCoF measurements.

Centralized UFLS methods embed the formulation of dedicated optimization problems with specific objectives that minimize the amount of shed loads [75], minimize the unnecessary activation of protection relays [76], etc. A similar contribution is [77], where a unified control framework allows managing frequency and the power imbalance. More specifically, by including the OPF equations within the optimization problem constraints, it is possible to restore the nominal frequency, maintaining nodal voltages, line currents, and power flows within the safety limits.

As for the local UFLS, it minimizes the need for communication equipment that may add delay and decrease reliability [78]. In contrast to frequency-based relays, RoCoF-based relays can provide a prompter and more effective response thanks to the anticipative effect inherent in their time-derivative formulation [79]. Indeed, recent literature advocates the adoption of RoCoF thresholds to trigger the load shedding action [80, 81, 82]. However, most studies only analyze and acknowledge the necessity of using RoCoF as an index for UFLS schemes without providing a strategy to measure it. In this respect, PMUs characterized by high reporting rate and remarkable measurement accuracy [79, 83] might represent a promising solution.

3 Impact of Converter-interfaced BESSs on Post-contingency Dynamics of Low-inertia Power Grids

The recent literature advocated the use of battery energy storage systems (BESSs) as a way to counterbalance the lack of inertia due to the massive deployment of converter-interfaced generation (CIG). In this context, it is essential to understand the impact of converter-interfaced BESSs on the dynamics of low-inertia grids, especially with respect to large interconnected systems interfacing a mix of rotating machines and converter-interfaced resources. In this regard, this Chapter proposes an extension of the IEEE 39-bus test network to quantify the impact of converter-interfaced BESSs on post-contingency frequency responses in low-inertia power grids. To this end, a low-inertia 39-bus system is obtained by replacing four synchronous generators in the original 10-synchronous machine system, with four wind power plants. Then, a large-scale converter-based BESS is integrated into such a low-inertia network to assess the impact of the BESS and its converter controls (grid-forming versus grid-following) on the dynamics of the low-inertia power system. The proposed models are implemented on a real-time simulator to conduct post-contingency analysis, respectively, for the original IEEE 39-bus power system and the low-inertia one, with and without the BESS.

This Chapter includes results of publication [84].

3.1 Introduction

As discussed in Chapter 2, displacing a significant share of conventional synchronous generation with massive renewable resources determines the inertia reduction of power systems and may lead to very fast dynamics in case of contingency. BESSs are broadly advocated as one of the potential solutions to address the challenges related to reduced levels of system inertia interface with power systems via converter suitably controlled as a grid-forming or grid-following unit.

In this context, quantitatively evaluating the impact of converter-interfaced BESSs as well as their control strategies in the dynamics of low-inertia power grids can provide valuable insights for system planning and the design of operational protections. An accurate representation of power electronics converters and their controls is required to study the dynamics of low-inertia power systems interfacing a mix of rotating machine and converter-interfaced resources. To this end, the low-inertia IEEE 39-bus power grids are proposed as extensions of the IEEE 39-bus benchmark power grid [85, 86], where part of the synchronous generators are replaced with type-III wind power plants to obtain low-inertia configurations. The IEEE 39-bus benchmark power grid and its extensions are fully modeled to capture realistic responses of power systems, the interaction between the converter-interfaced BESS and the low-inertia power grid, and the closed-loop dynamics between the converter and the battery DC voltage model.

In this Chapter, the proposed dynamic models are used to quantitatively assess the impact of inertia reduction in power systems' post-contingency dynamics and analyze the response of grid-forming and grid-following converter-interfaced BESSs to a sudden significant power imbalance in the low-inertia power grids. The considered contingency events, i.e., generator tripping causing a significant loss of generation power, are reproduced in time-domain simulations. In addition, sensitivity analysis of system frequency responses with respect to specific converter control parameters is conducted.

The Chapter is structured as follows. Section 3.2 describes the extension of the IEEE 39-bus benchmark network and summarizes the dynamic simulation models of the low-inertia 39-bus power grids. Section 3.3 presents the considered grid-forming and grid-following control approaches for the converter-interfaced BESSs. Section 3.4 presents and discusses the simulation results of the contingency tests. Section 3.5 provides a sensitivity analysis of the system frequency response with respect to the critical converter control parameters. Finally, Section 3.6 provides a discussion and some remarks.

3.2 Extension of the IEEE 39-bus Test Network for the Study of Dynamics of Low-inertia Power Grids

This section presents the extension of the original IEEE 39-bus benchmark power system to a low-inertia setting for studying fundamental dynamics of low-inertia power grids in presence of CIG. The proposed low-inertia configurations are described in Section 3.2.1 while the models of the devices are summarized in Section 3.2.2. The modeling details and parameters used in the proposed models are all provided in the Appendix A.

3.2.1 Low-inertia Configurations

The IEEE 39-bus benchmark test network, shown in Figure 3.1a, has been widely adopted for studies of power system dynamics since it first appeared in [85]. This benchmark systems, also referred to as "New England test system", has 39 buses, 10 synchronous generators, and 19 loads. Starting from the original configuration of the 39-bus benchmark system (referred to as Config. I), Two new system configurations are derived to evaluate the system behavior in a low-inertia setting while considering the converter-interfaced BESS. These two new configurations are:

- a low-inertia 39-bus power system obtained by replacing 4 synchronous generators with 4 aggregated type-III wind power plants (referred to as Config. II);
- a low-inertia 39-bus power system obtained by replacing 4 synchronous generators with 4 aggregated type-III wind power plants and introducing a converter-interfaced BESS (referred to as Config. III).

More specifically, the Config. II is obtained by modifying the IEEE 39-bus benchmark power system through replacing 4 synchronous generators (denoted in Figure 3.1a as G1, G5, G8, and G9) with 4 wind power plants (denoted in Figure 3.1b as WP1, WP4, WP2, and WP3). The inertia constant of the low-inertia 39-bus power grid (referred to as a 10 GW base and obtained by summing the inertia constant of all the conventional power plants) is 1.98 s. Such a value is quite low if compared to the initial constant of 7.85 s characterizing the original IEEE 39-bus benchmark power system. The Config. III, as shown in Figure 3.1c, is created by integrating a BESS at bus 17 into the low-inertia 39-bus power system.

3.2.2 Summary of the Dynamic Models Adopted in the Extended 39-bus Power Systems

The studies discussed in the following sections are based on the detailed dynamic models of grids, converters, and controls to analyze the impact of inertia reduction, converter-based BESS and its control approaches (grid-following versus grid-forming) on the post-contingency dynamics of low-inertia power systems. All dynamic models described in this section are built in MATLAB/ Simulink and executed in an OPAL-RT eMEGAsim real-time simulator. For the sake of reproducibility, all of the proposed models are open-source and available online [87], and the modeling details and parameters used in the proposed models are provided in Appendix A.

The dynamic models of all devices in the extended IEEE 39-bus power systems are also used in Chapter 4, Chapter 5 and Chapter 6. Therefore, it is worth to summarize once the main feature of the dynamic models here below. Nevertheless, the inputs and control approaches adopted by the devices in the extended IEEE 39-bus power systems will be specified in each chapter.

Conventional generators are simulated with a sixth-order model for the synchronous generator [85, 88, 89, 90], a prime mover and governor model [91, 92, 93, 94, 95], and an excitation system associated with an Automatic Voltage Regulator (AVR) [96, 86]. Each generator's governor includes a frequency containment regulator with a droop coefficient of 5%. Each wind farm is simulated by scaling up a detailed model of a type-III wind turbine, including a sixth-order

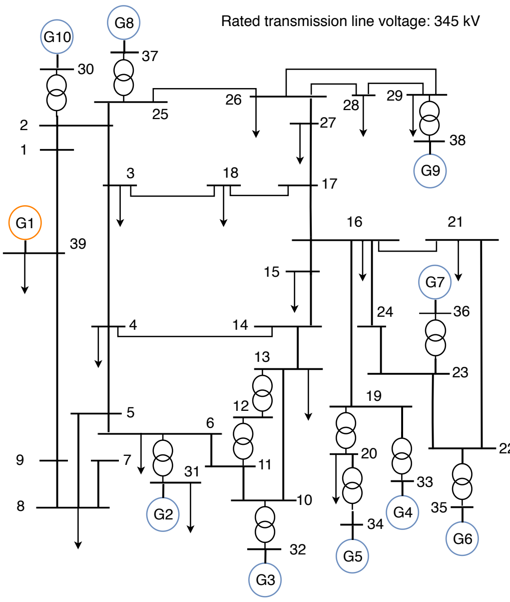

(a) Topology of the IEEE 39-bus benchmark test network (Config. I).

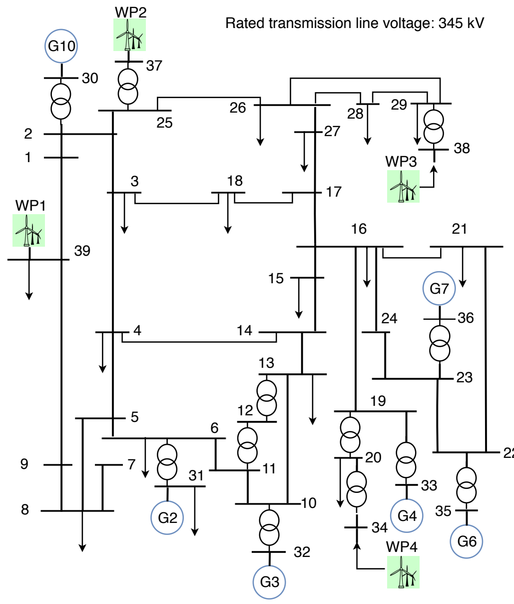

(b) Topology of the low-inertia 39-bus benchmark power system (Config. II).

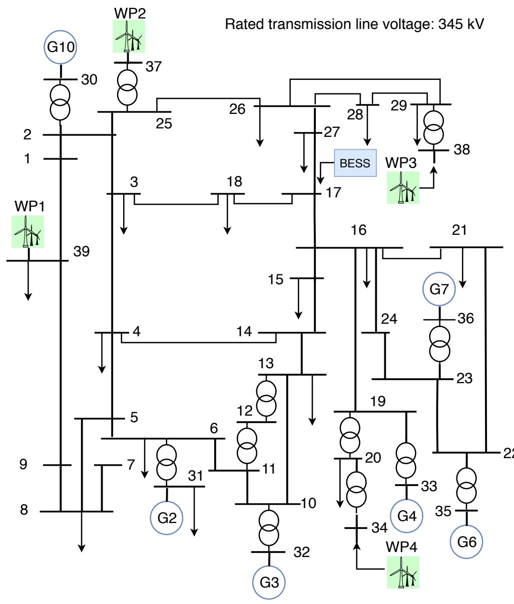

(c) Topology of the low-inertia 39-bus benchmark power system with the presence of the BESS (Config. III).

Figure 3.1 – Topologies of the extended IEEE 39-bus power systems.

model for the double-fed induction generator (DFIG) and the averaged model for the AC/DC back-to-back converter [97, 98]. This is done in order to retain a relatively good dynamic modeling representation of interactions among the wind turbines and the power grid [99]. Loads are reproduced with a three-phase frequency and voltage-dependent EPRI LOADSYN load model [100] associated with the input of realistic power demand measurements. A single equivalent system with a power rating of 225 MVA and an energy capacity of 175 MWh is considered for the BESS. Its model consists of multiple battery packs and a four-quadrant DC/AC power converter. Each battery pack is simulated with a three-time-constant equivalent circuit model with SOC-dependent parameters. This Thesis uses the model proposed in [101, 102] for a Lithium-Titanate-Oxide battery, assuming a 2s156p[1] configuration of the battery packs (with identical parameters) feeding a single DC bus. The power converter is a fully modeled three-level neutral-point clamped (NPC) converter.

The detailed dynamic models implemented in this simulation setup are to reproduce the dynamic interactions among the low-inertia power grid, the converter-based BESS, and the battery DC voltage model. Particularly, the power converter is modeled in detail to preserve the DC voltage dynamics and their interactions with the AC grid. Especially, the DC voltage dynamics are associated to the battery voltage which is modeled by a three-time constant model, where the lowest time constant is in the order of a few milliseconds (see in appendix A.5). In this respect, the detailed model is capable to capture the whole spectrum of DC dynamics. Moreover, in the model, there are synthetic PMUs implementing the same signal processing used in real devices. Therefore, the modeling of the power converter switching allows obtaining waveforms of current and voltages that are corrupted by harmonics and high switching frequency components. In this view, the detailed model allows reproducing high-fidelity and realistic waveforms to be processed by PMUs to provide phasors estimation for the quantitative assessment of frequency containment performance and for various control actions such as UFLS.

It is also worth noting that the Hornsdale BESS developed by AEMO has been used to determine the energy rating of the BESS adopted in the model, as the AEMO's BESS is the only one so far used for frequency containment response in a transmission system. Conversely, the power rate has been selected to be meaningful for the size of the IEEE 39-bus network, i.e., approximately 5% of the peak load.

3.3 Power Converter Controls of the BESSs

The main approaches, i.e., *grid-following* and *grid-forming*, to control converter-interfaced BESSs are investigated. By means of outer loops, the converter-based units can adapt the injected active and reactive power to provide frequency and voltage support. In this respect, we consider the grid-forming and grid-following controls that are capable of providing frequency containment support by regulating the active power in response to the frequency variation.

[1] Two battery packs in series, and 156 series in parallel.

It should be noted that the presented grid-following and grid-forming units shown in Figure 3.2, 3.3 and 3.4, comprise identical electrical parameters, where L_f, C_f, R_f are the inductance, capacitance and resistance of converter's AC filter, respectively, and L_c and R_c are the equivalent inductance and resistance of the step-up transformer connecting with the low-inertia 39-bus power grid at the PCC.

In the following of this section, the considered PLL-free grid-forming converter controls [58, 62] are described in Section 3.3.1 and the grid-following control operated with the grid-supporting mode is introduced in Section 3.3.2.

3.3.1 PLL-free Grid-forming Converter Controls

The grid-forming control allows the converters operating as synchronized voltage sources. Thereby, they can use the angle difference between the grid voltage and the modulated voltage to control the converter power output. As introduced in Section 2.3, the estimate of the grid voltage angle is necessary and can be achieved in two ways: use a PLL or, instead, directly link the active power exchange to the angle difference between the grid voltage (θ_g) and the modulated voltage (θ_m) to create a PLL-free controller. We opt for the PLL-free grid-forming control as it allows to explicitly choose the inertia and also provide frequency droop regulation [36]. Specifically, we consider the PLL-free grid-forming converter control with coupled functionalities proposed in [58] and the PLL-free grid-forming converter control with decoupled functionalities proposed in [62].

PLL-free Grid-forming Converter Control with Coupled Functionalities

As discussed in [58], the active power control layout, highlighted in blue in Figure 3.2, is an effective and simple scheme that allows the converter to synchronize with the grid while intrinsically provide the frequency containment response. In this regard, the synchronization functionality is coupled with the frequency containment. Specifically, the frequency droop coefficient m_p corresponds to the active power-frequency $p-f$ droop coefficient; a first-order low-pass filter with cut-off frequency ω_{LP} is usually added to avoid fast frequency variations imposed by the control of the converter's switches and filter out the power measurements noise; a lead-lag filter with time constants T_1 and T_2 is usually applied to the power measurements to improve the converter dynamics [103]. The reactive power compensation with droop n_q adjusts the voltage magnitude reference according to the difference between actual reactive power output and the reference reactive power. P_{meas} and Q_{meas} are the active and reactive power measured before the step up transformer, which is represented by the equivalent inductance L_c and resistance R_c. ω_{ref} and E_{ref_dq} are respectively the frequency and voltage set-points of the grid-forming converter. The adopted grid-forming control aligns the modulated voltage with the d-axis, thus the q-axis component of the voltage reference E_{ref_q} is set to 0. With this scheme, the value of equivalent inertia constant of the grid-forming

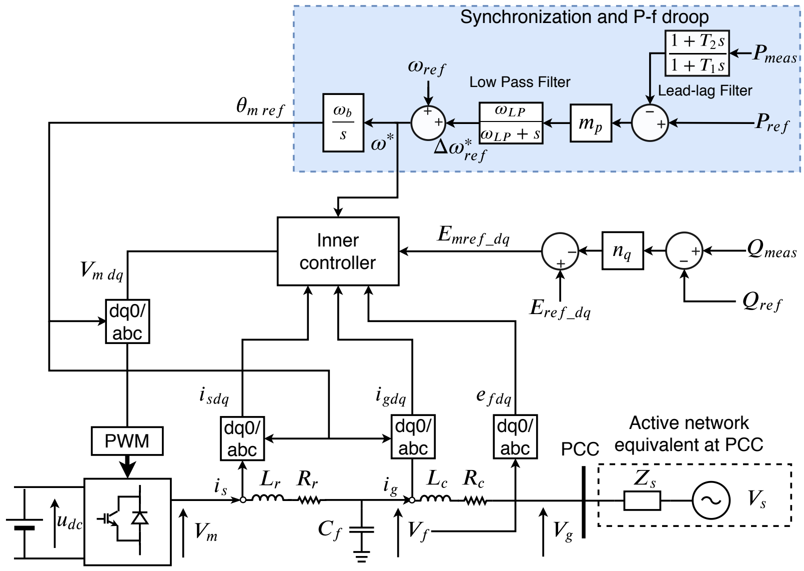

Figure 3.2 – PLL-free grid-forming converter with coupled functionalities.

control H_{GFM} is linked with m_p and ω_{LP} [58, 36] as follows:

$$H_{GFM} = \frac{1}{2\omega_{LP} m_p} \tag{3.1}$$

PLL-free Grid-forming Converter Control with Decoupled Functionalities

As shown in Figure 3.3, the PLL-free grid-forming control with decoupled functionalities is able to decouple the two control functionalities, the synchronization and the frequency containment controls, without any dedicated PLL. It allows to explicitly define the inertia constant H_{GFM} for the synchronization functionality, as well as the droop coefficient m_p for the frequency containment control. In order to make a fair comparison between the two grid-forming controls, the inertia constant of the grid-forming control with decoupled functionalities are selected to be equal to the inertia constant of the grid-forming control with coupled functionalities. A proportional action k_p on the active power is added to damp the oscillation, which results in a specific formulation of the PI controller, as depicted in the blue sub-diagram of Figure 3.3. The reactive power compensation with droop n_q adjusts the voltage magnitude reference according to the difference between actual reactive power output and the reference reactive power. P_{meas} and Q_{meas} are the active and reactive power measured before the step-up transformer. ω_{ref} and E_{ref_dq} are respectively the frequency and voltage set-points of the grid-forming converter. As the modulated voltage is aligned with the d-axis, the q-axis component of the voltage reference E_{ref_q} is set to 0.

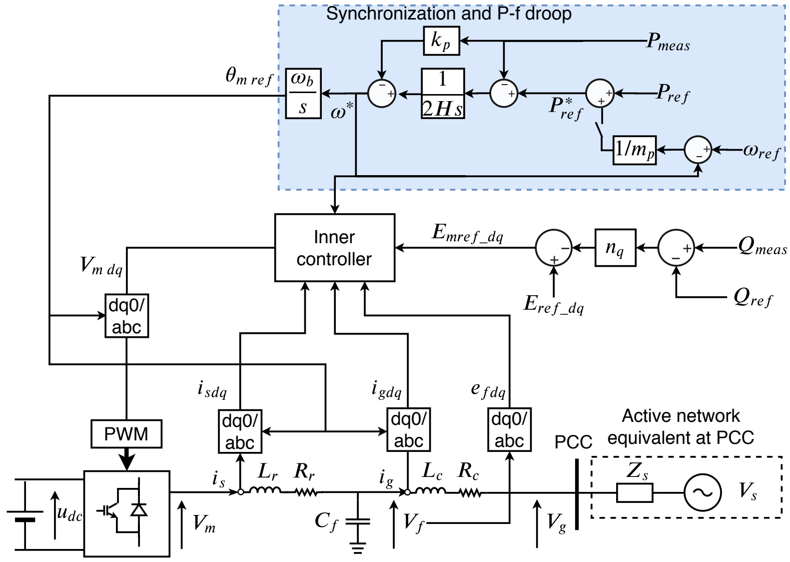

Figure 3.3 – PLL-free grid-forming converter with decoupled functionalities.

Coupling of Active and Reactive Power

The two PLL-free grid-forming controls described above are with effective simple schemes that enable the converter to synchronize with the main grid and provide the frequency containment service respectively in a coupled or decoupled way. Nevertheless, it is worth to note that, for both of the two grid-forming controls, the active and reactive power are not decoupled. The coupling of active and reactive power can be easily quantified using the power exchange at the PCC that can be expressed using the general expression for power transmitting between two ends (here, the PCC is considered as receiving end):

$$P = \frac{V_g V_m}{|Z|}\cos(\theta-\delta) - \frac{V_g^2}{|Z|}cos\theta \tag{3.2}$$

$$Q = \frac{V_g V_m}{|Z|}\sin(\theta-\delta) - \frac{V_g^2}{|Z|}sin\theta \tag{3.3}$$

where V_g and V_m are the magnitude of the PCC voltage and the modulated voltage, respectively, δ is the angle difference between grid voltage and the modulated voltage ($\theta_g - \theta_m$), $Z = X + jR$ represents the impedance between the converter and the PCC, and θ is the angle of impedance Z. In the adopted PLL-free grid-forming controls, the angle of the modulated voltage θ_m is dedicated to regulate the active power commanded from the outer loop (i.e., the synchronization and $p - f$ droop controller). As a consequence, the reactive power, as expressed in Figure 3.3, varies due to the change of $\delta = \theta_g - \theta_m$. The magnitude of the modulated voltage is a controllable variable to regulate the reactive power, whereas its tuning range is rather limited as voltage magnitudes in interconnected systems are generally required to be within ±5% p.u. during normal operating state and within ±10% p.u. after the occurrence

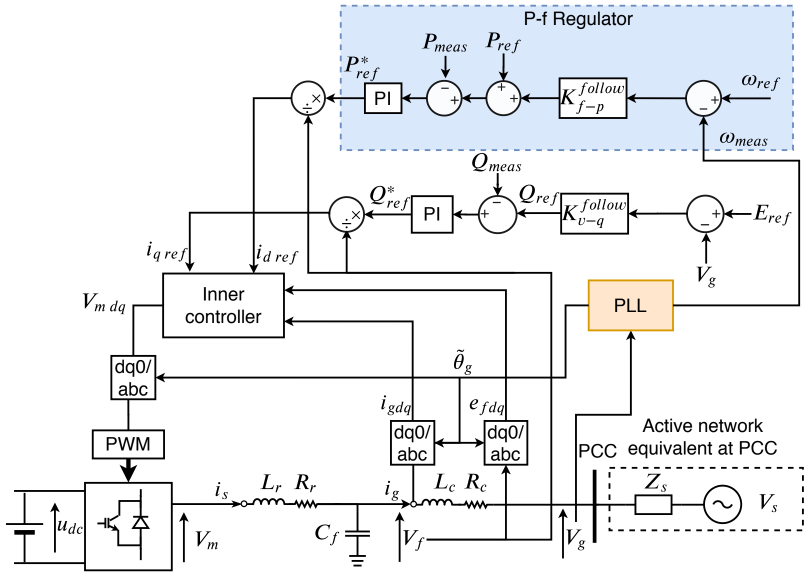

Figure 3.4 – Grid-following converter with grid-supporting mode.

of a contingency [104].

3.3.2 Grid-following Control Operated with Grid-supporting Mode

As known, the grid-following converter controls the values of active and reactive power by controlling the amplitude and phase of the injected current with respect to the grid-voltage at the PCC. In this case, a three-phase PLL is required to estimate the fundamental frequency phasor of the grid voltage (usually the tracking referes to the direct sequence component), so as to generate the instantaneous value of the current reference and, eventually, the voltage reference. In this regard, the active and reactive power are controlled independently.

As shown in Figure 3.4, the adopted grid-following converter is operated with grid-supporting mode by adding higher-level frequency and voltage droop regulators. The active power is regulated according to the $f-p$ control gain $K_{f-p}^{following}$, as the frequency deviates from the reference value. The reactive power is regulated according to the $v-q$ control gain $K_{v-q}^{following}$, as the difference between the measured voltage and the voltage reference exceeds the dead-band of ΔV_{tr}.

A three-phase Moving Average Filter-based PLL (MAF-PLL) [105] is used for tracking the fundamental frequency phasor of the grid voltage at the PCC. As shown in Figure 3.5, it consists of a phase detector, a loop filter and a voltage controlled oscillator. The loop filter includes a frequency-adaptive MAF and a PI controller so as to enhance the PLL's filtering capability [106]. The MAF receives the input from the phase detector and has been designed in such a way that it let pass the DC components and blocks the sinusoidal disturbances

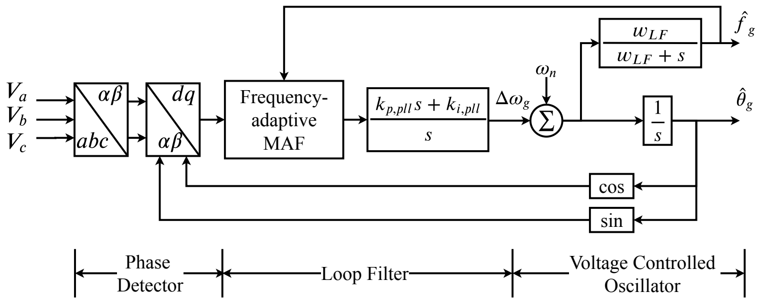

Figure 3.5 – PLL implemented in grid-following converter with grid-supporting mode.

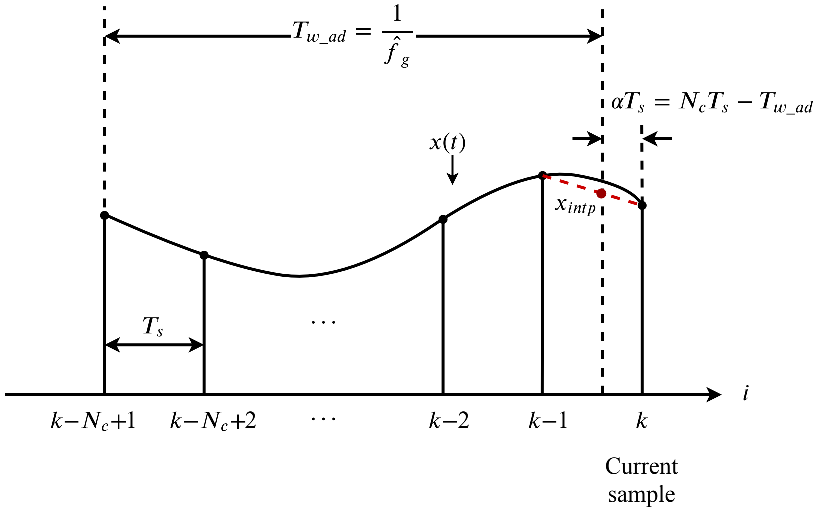

Figure 3.6 – Incorporating the linear interpolation method into the MAF. The dashed red line shows the linear interpolation to estimate the inter-sample value.

associated to integer multiples of the frequency f_d in hertz, i.e., $T_w = 1/f_d$, where T_w is the length of the moving average window. It's discrete-time expression is:

$$\overline{x}(k) = \frac{1}{N}\sum_{i=0}^{N-1} x(k-i) \tag{3.4}$$

where N is the number of sample contained in the window T_w, i.e., $T_w = NT_s = 1/f_d$ and T_s is the PLL sampling time step. However, a non-ideal behaviour of the PLL may take place for fast frequency variations and, as a consequence, the MAF would not completely block the disturbance components. In this regard, inspired by [106], the frequency-adaptive MAF is used to adjust the moving average time window T_{w_ad} according to the frequency variation. An approach to make the MAF frequency adaptive is to incorporate the linear interpolation method into the MAF, as shown in Figure 3.6. The MAF order, N, is adjusted by rounding-up T_{w_ad}/T_s to the nearest integer, i.e.,

$$N = N_c = \mathrm{ceil}(T_{w\_ad}/T_s) \tag{3.5}$$

where $T_{w\_ad} = 1/\hat{f}_g$, and $\hat{f}_g$ is the PLL estimated frequency at the last time-step. Then, the inter-sampled value x_{intp} is interpolated according to the the rounding-up residual

$$\alpha T_s = N_c T_s - T_{w\_ad} \tag{3.6}$$

By using this approach, the MAF is defined as

$$\overline{x}(k) = \frac{T_s}{T_{w\_ad}}\Big(\sum_{i=0}^{N_c-1} x(k-i) - \alpha x(k) + \frac{1}{2}\alpha^2[x(k) - x(k-1)]\Big) \tag{3.7}$$

Finally, the parameter w_{LF} in Figure 3.6 is the cut-off frequency of the low-pass filter applied to reduce the oscillation of $\hat{f}_g$, which is used by both the frequency-adaptive MAF and upper-level frequency droop controller.

3.4 Post-contingency Dynamics in Low-inertia Power Grids

This section illustrates and discusses dynamic simulation results of contingency tests conducted on the original 39-bus power grid and on the low-inertia 39-bus power grid, without or with the converter-interfaced BESS. Specifically, Section 3.4.1 demonstrates the impact of inertia reduction on the system's post-contingency frequency containment. Section 3.4.2 quantitatively assesses the enhancing performance of post-contingency frequency containment by integrating a large-scale converter-interfaced BESS in the low-inertia power grid, as well as compares the grid-forming with the grid-following converters in view of supporting the power system under contingency. Section 3.5 provided a sensitivity analysis of the post-contingency frequency containment with respect to the critical converter control parameters.

3.4.1 Impact of Inertia Reduction

This subsection first evaluates the system response under contingency without the presence of converter-interfaced BESS to show the impact of inertia reduction in the 39-bus power system. To this end, the same contingency (i.e., the tripping of generator G6) is reproduced in both Config. I and Config. II. Table 3.1 reports the initial nodal power injections[2] (i.e., pre-contingency power injections) for Config. I and Config. II. It shows that the nodal active power injection of G6 in Config. I and Config. II are very close. Therefore it is suitable to compare the post-contingency frequency containment of Config. I and Config. II under the contingency of the tripping of G6. It also shows that, in Config. II, the wind generation accounts for more than half of the total active power injection, i.e., 3789 MW versus 7129 MW.

Figure 3.7 shows the system frequency (here quantified by the rotor speed of synchronous generators) for Config. I and Config. iI. It can be seen that, after the tripping of G6, the grid frequency decreases way faster in Config. II than in Config. I. The frequency nadir for

[2]The reactive power provided by the wind power plants are generated by shunt capacitors.

Table 3.1 – Initial nodal power injections.

Unit	Active Power [MW]		Reactive Power [MVar]	
	Config. I	Config. II	Config. I	Config. II
G1/WP1	1353	1335	253	86
G2	816	579	115	56
G3	597	509	70	-61
G4	697	545	-56	10
G5/WP4	406	501	64	14
G6	799	816	113	67
G7	446	530	-25	-46
G8/WP2	698	1145	-108	57
G9/WP3	699	803	-73	29
G10	598	414	41	-87
Total	7129	7147	295	206

Config. II is 46.77 Hz, 2.44 Hz lower than 49.21 Hz for Config. I. In addition, the frequency transient is much longer in Config. II (80 s) than in Config. I (30 s). This is to be expected since Config. II has much lower system inertia than Config. I. Due to the lack of inertia, Config. II experiences a much faster frequency decreasing velocity, a way lower frequency nadir, and a longer oscillation duration.

Figure 3.8 shows the RoCoF for Config. I and Config. II. The RoCoF values illustrated in this Chapter are all computed using the rotor speed of each synchronous generators. The rotor speed is filtered by a moving average filter with a window length of 200 ms and the time difference for computing the RoCoF is 60 ms. The RoCoF dynamics for the 5 synchronous generators exhibits more heterogeneity than the corresponding frequency values. The sources of such difference include various inertia constants, parameters for the governing systems and the synchronous machines, as well as the electrical distances to the contingency node. For instance, the RoCoF of generator 7, which is the closest to the contingency node, experiences higher RoCoF and RoCoF oscillating amplitude that than generators. Nevertheless, when compare the RoCoF of the same generator for Config. I versus for Config. II, the RoCoF results are consistent, showing that the RoCoF values for Config. I are lower than those for Config. II. Specifically, the maximum RoCoF for G2 is 0.54 Hz/s in Config. I vs 1.47 Hz/s in Config. II, the maximum RoCoF for G3 is 0.38 Hz/s in Config. I vs 1.19 Hz/s in Config. II, the maximum RoCoF for G4 is 0.75 Hz/s in Config. I vs 1.56 Hz/s in Config. II, the maximum RoCoF for G7 is 1.18 Hz/s in Config. I vs 1.73 Hz/s in Config. II, and the maximum RoCoF for G10 is 0.42 Hz/s in Config. I vs 1.36 Hz/s in Config. II.

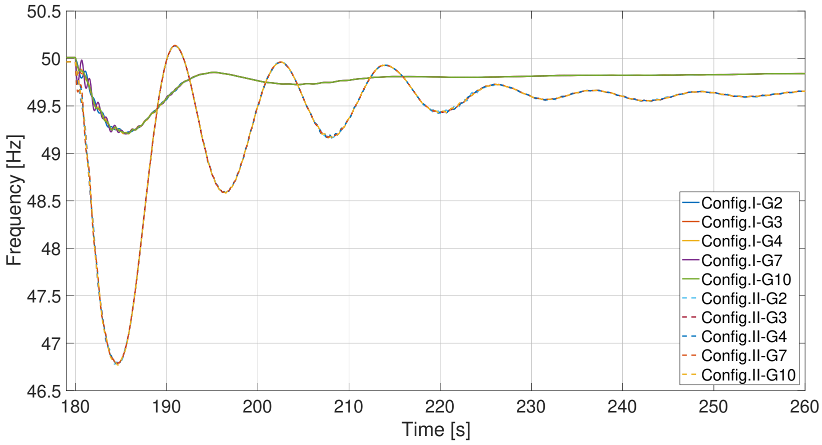

Figure 3.7 – Frequency for Config. I and Config. II (represented by the rotor speed of synchronous generators).

3.4.2 Impact of Converter-interfaced BESS

In Config. III, a converter-interfaced BESS, modeled as introduced in Section 3.2.2 and detailed in Appendix A.5, is integrated into the low-inertia 39-bus power grid. The grid-forming and grid-following converter controls described in Section 3.3 are individually implemented in the BESS converter. For the sake of brevity, the PLL-free grid-forming control with coupled functionalities is denoted as GFM1, the PLL-free grid-forming control with decoupled functionalities is denoted as GFM2, and the grid-following control with grid-supporting mode is denoted as GFL. Thereby, Config. III is used to assess the impact of converter-interfaced BESS and compare the performance of grid-forming and grid-following controllers in the low-inertia 39-bus power grid in two study cases:

- *Case 1*: same contingency as in Section 3.4.1, tripping of G6 (816 MW generation loss).
- *Case 2*: tripping of G4 (545MW generation loss).

Case 1: tripping of generator G6

Figure 3.9 shows a comparison of the frequency containment and RoCoF for Config. II vs Config. III under the contingency of tripping G6. Figure 3.9a, 3.9c, 3.9e. 3.9g and 3.9i show that the converter-interfaced BESS achieves to increase frequency nadir from 46.8 Hz for Config II to 47.4 Hz for Config. III. Figure 3.9b, 3.9d, 3.9f, 3.9h, and 3.9j illustrate that the converter-interfaced units are capable to limit the RoCoF. Specifically, the maximum RoCoF in Config. II and Config. III varies the following way:

- from 1.49 Hz/s to 1.37 Hz/s for G2
- from 1.21 Hz/s to 1.12 Hz/s for G3

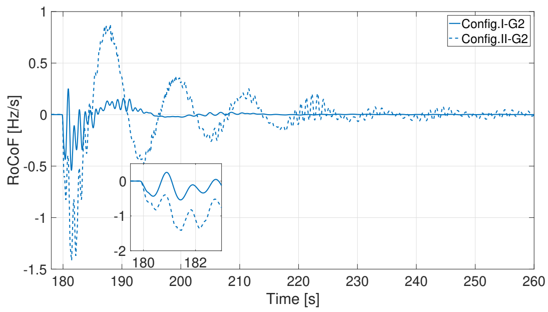

(a) RoCoF for G2

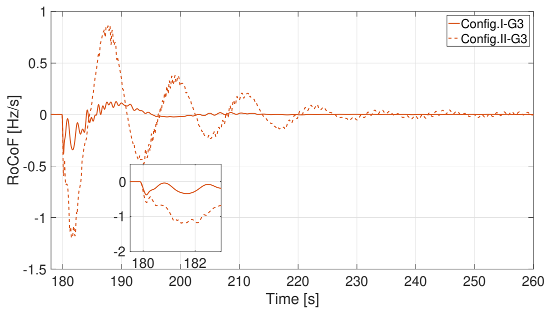

(b) RoCoF for G3

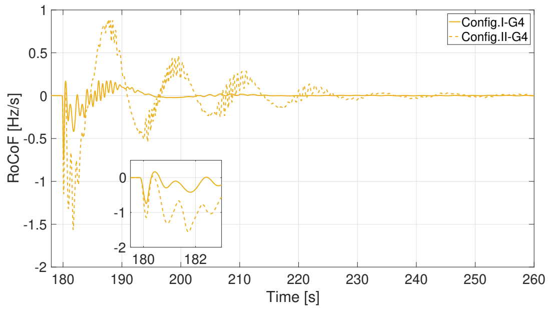

(c) RoCoF for G4

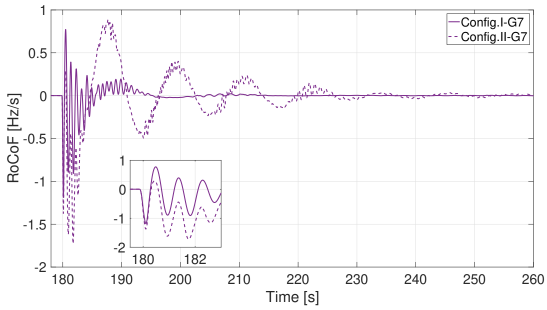

(d) RoCoF for G7

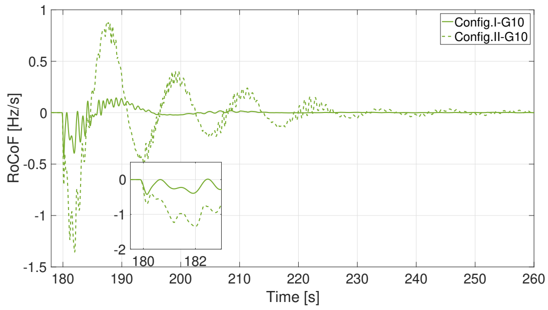

(e) RoCoF for G10

Figure 3.8 – RoCoF for Config. I and Config. II.

- from 1.62 Hz/s to 1.42 Hz/s for G4
- from 1.79 Hz/s to 1.58 Hz/s for G7
- from 1.38 Hz/s to 1.18 Hz/s for G10

Also, Config. III exhibits a better damping of the frequency oscillations by decreasing the overall transient interval from 80 s to 40 s.

Figure 3.10 shows the active power for the installed converter unit. The grid-following and the grid-forming controllers use the same frequency droop coefficient 5%, thus both controllers inject active power into the power system following the same droop characteristic. It is worth noting that, for the two adopted grid-forming controls (i.e., with coupled and decoupled functionalities), the inertia constants are identical, where $H_{GFM} = \frac{1}{2\omega_{LP} m_p} = 0.3185$ s. Concerning the comparison among the converter controls, although it is not notably distinguishable from the frequency nadir, the voltage response immediate after the contingency exhibits differences. To this end, the analysis on the voltage response of the converter unit is provided here below.

In order to better indicate the location of the measured voltages and reactive power illustrated in *Case 1* and *Case 2*, the electrical diagram of the AC side of the converter is shown in Figure 3.11. The whole electrical diagram of the converter are provided in the Appendix A.5.

In Figure 3.11, L_c and R_c are the equivalent inductance and resistance of the step-up transformer, V_f and θ_f are the voltage phasor and angle of at the node before the transformer, V_g and θ_g are the PCC voltage phasor and angle, P_{LV} and Q_{LV} are the active power and reactive power before the transformer, and P_{MV} and Q_{MV} are the active power and reactive power at the PCC. Figure 3.12a shows the magnitude of the voltage before the transformer denoted as V_f in Figure 3.11. Figure 3.12b presents the magnitude of the PCC voltage denoted as V_g in Figure 3.11. After the contingency, there is a voltage sag within 500 ms and the grid-following unit experiences a higher voltage drop (i.e., decrease 6% and 9% of nominal voltage for V_f and V_g, respectively) than the grid-forming units (i.e., decrease of 4.5% and 8% of nominal voltage for V_f and V_g, respectively).

The reactive power before and after the transformer (denoted as Q_{LV} and Q_{MV}, respectively) is shown in Figure 3.12c and Figure 3.12d, respectively. Two observations on the change of reactive power immediate after the contingency are worth to be noted: 1) the change of the active power before the transformer Q_{LV} are very similar for the grid-forming and grid-following controls, i.e., $\Delta Q_{LV}^{GFM1} = 0.34$ p.u., $\Delta Q_{LV}^{GFM2} = 0.31$ p.u. and $\Delta Q_{LV}^{GFL} = 0.31$ p.u., whereas the converter voltage magnitude of the grid-following control experiences a considerable larger decrease; 2) the reactive power after the transformer Q_{MV} injected by the grid-forming units is much higher than the one by grid-following. These phenomenons are explained by the fact that the grid-forming controls allow the converter operating as a voltage source which creates its own voltage phasor reference, whereas the grid-following control follows the phasor of the grid voltage at PCC. Such a difference influences the reactive power injected into the grid since

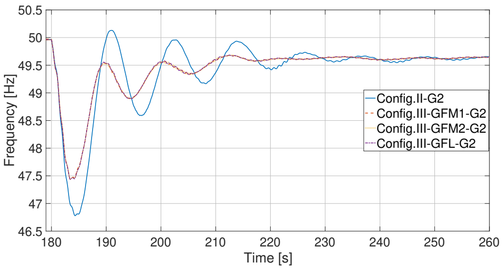

(a) Frequency for G2

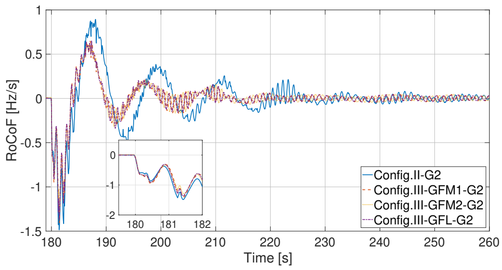

(b) RoCoF for G2

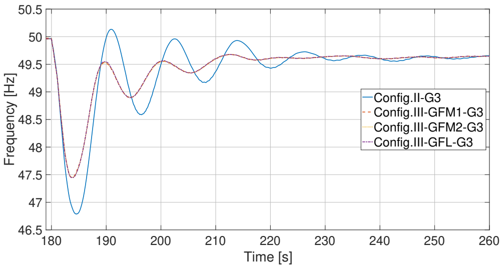

(c) Frequency for G3

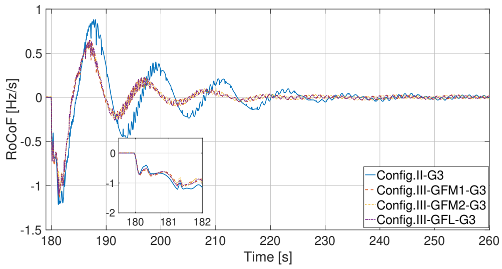

(d) RoCoF for G3

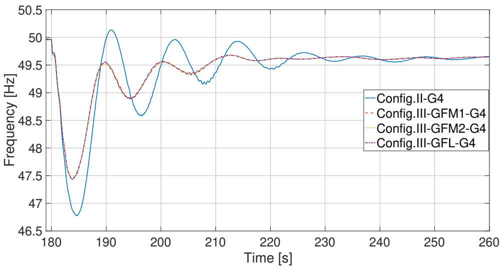

(e) Frequency for G4

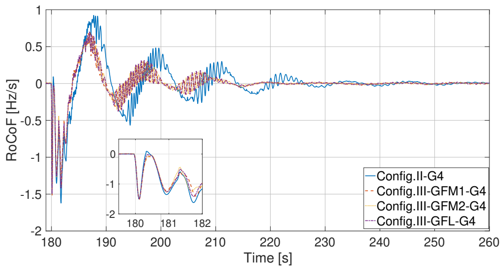

(f) RoCoF for G4

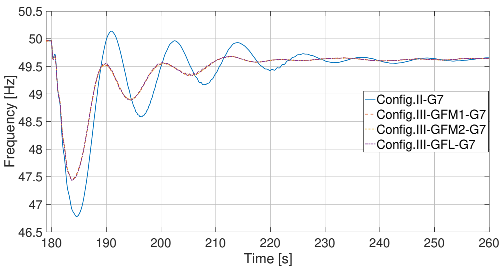

(g) Frequency for G7

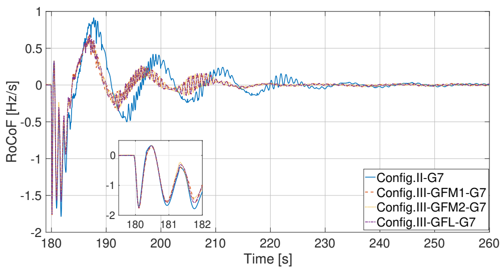

(h) RoCoF for G7

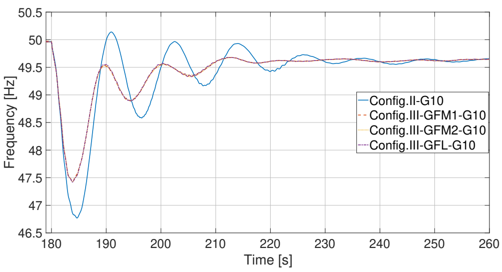

(i) Frequency for G10

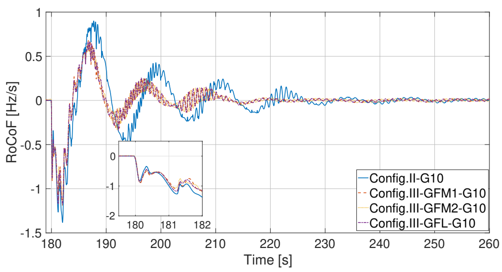

(j) RoCoF for G10

Figure 3.9 – Frequency and RoCoF of low-inertia 39-bus power grids for *Case 1*.

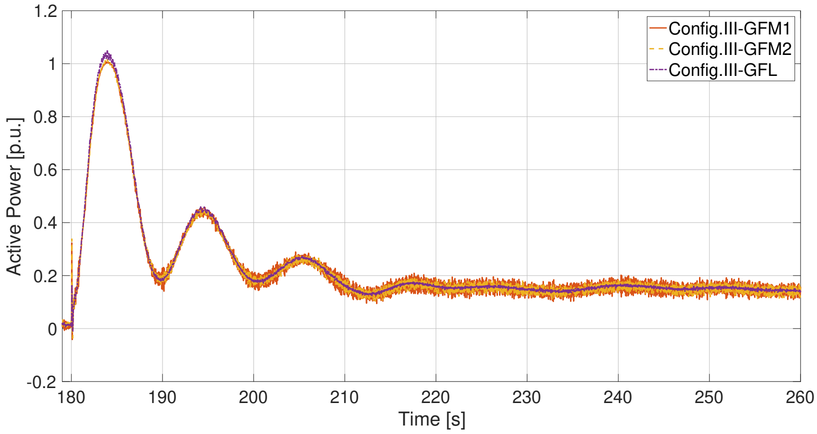

Figure 3.10 – Active power injected by converter-interfaced BESS for *Case 1*

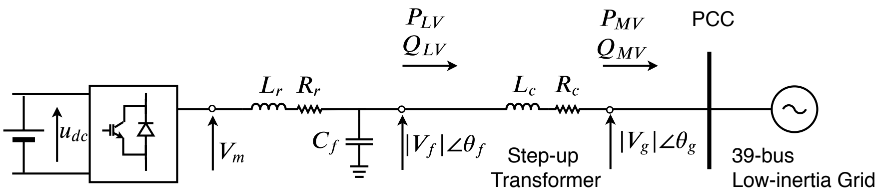

Figure 3.11 – Diagram of the AC side of the converter.

it is also coupled with the angle difference between the converter and the PCC voltage phasors (i.e., $\theta_f - \theta_g$). More specifically, the reactive power before and after the transformer can be expressed as

$$Q_{LV} = \frac{|V_g|}{X_T}\big(|V_f|cos(\theta_f - \theta_g) - |V_g|\big) \tag{3.8}$$

$$Q_{MV} = \frac{|V_f|}{X_T}\big(|V_f| - |V_g|cos(\theta_f - \theta_g)\big) \tag{3.9}$$

where X_T is the inductance of the transformer, $|V_f|$ and $|V_g|$ is the magnitude of voltage phasors V_f and V_g, respectively.

As illustrated in Figure 3.12e, within the first 200 ms after the contingency, the maximum angle difference $\theta_f - \theta_g$ for the grid-forming units (0.058 rad for GMF1 and 0.064 rad for GFM2) are significantly larger than the one for the grid-following unit (0.028 rad). Small angle differences are observed for the grid-following converter because, as a grid "follower", the control keeps tracking the phasor angle of the grid voltage as soon as possible. In contrast, the grid-forming control first maintains its modulated voltage angle right after a sudden system disturbance. Then, the modulated voltage angle is modified by the synchronization controller (linked with the converter's active power output) such that the grid-forming converter re-synchronizes with the grid. Therefore, as in contrast to the grid-following unit, the grid-forming unit can better maintaining the converter voltage following a sudden system disturbance.

Figure 3.13 shows converter DC voltage, DC current, and battery SOC for *Case 1*. The DC voltage varies as a function of the DC current and according to the response of the three-time constant model used to represent the BESS dynamics. The SOC of the BESS is decreasing in a way that corresponds to the integration of the injected power into the grid due to the frequency regulation.

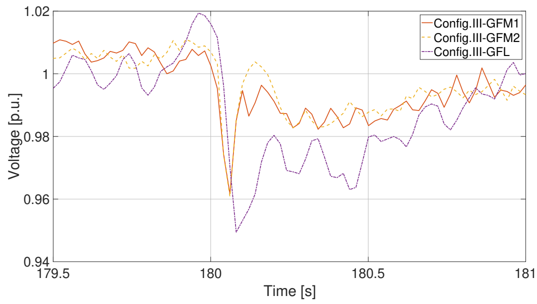

(a) Voltage before transformer

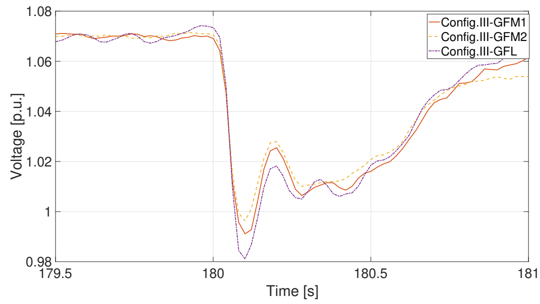

(b) Voltage after transformer

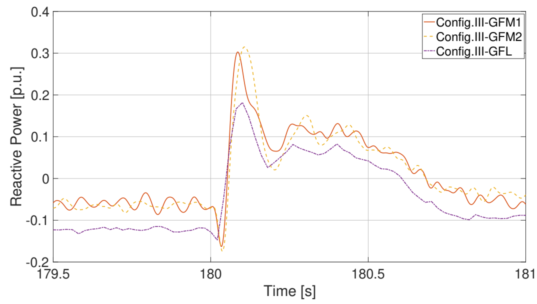

(c) Reactive power before transformer

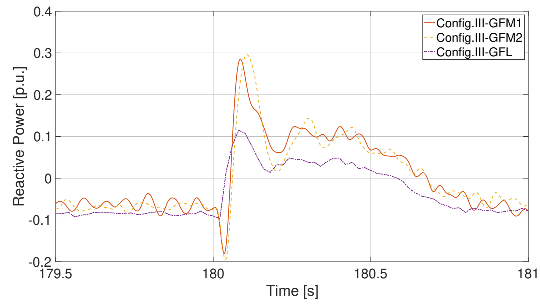

(d) Reactive power after tansformer

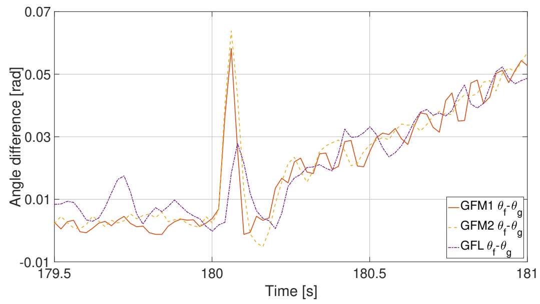

(e) Voltage angle difference between the two sides of converter's transformer

Figure 3.12 – Voltage before the transformer (i.e., V_f in Figure 3.11), voltage after the transformer (i.e., V_g in Figure 3.11), reactive power before and after the transformer (i.e., Q_{LV} and Q_{MV} in Figure 3.11, respectively), and voltage angle difference between the two sides of the transformer (i.e., $\theta_f - \theta_g$) for *Case 1*.

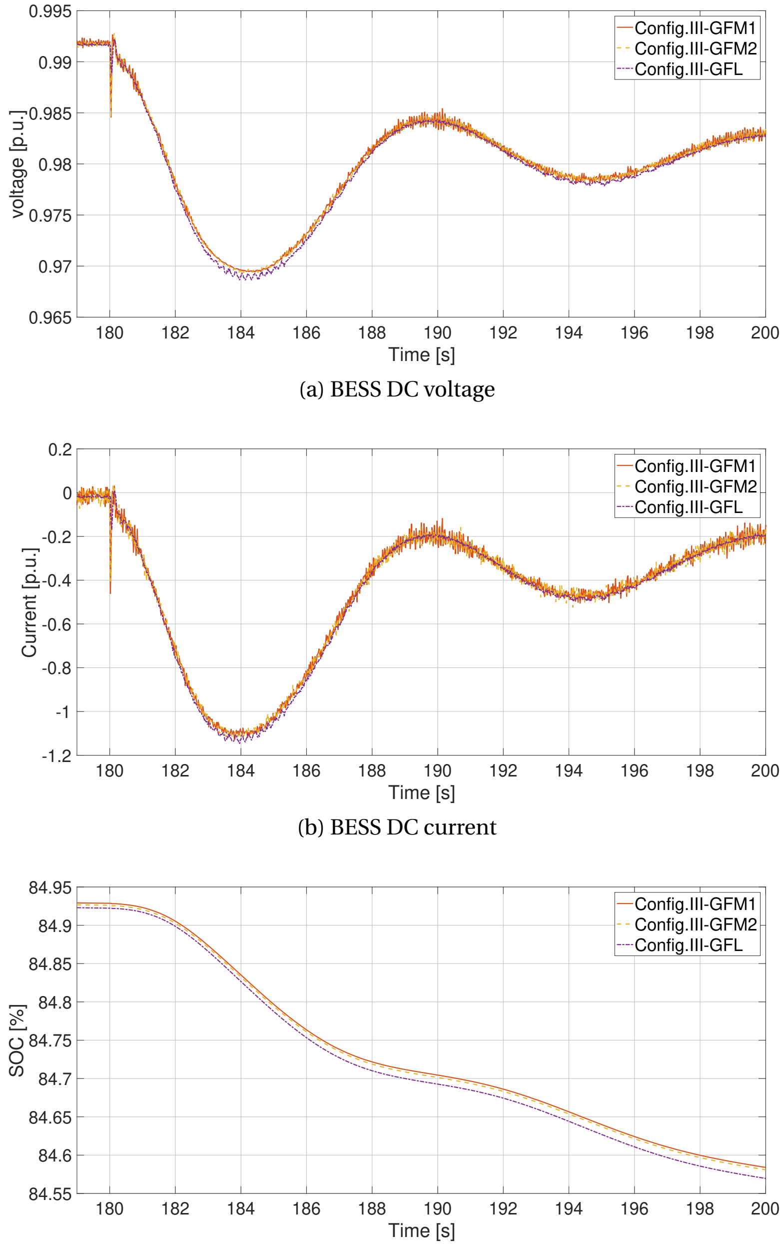

(a) BESS DC voltage

(b) BESS DC current

(c) BESS SOC

Figure 3.13 – Converter DC voltage, DC current and BESS SOC in Config. III for *Case 1*.

***Case 2*: tripping of generator G4**

Case 2 reproduces a less extreme contingency, with the tripping of G4 causing less generation loss. The same frequency droop coefficient 5% as in *Case 1* has been implemented for the three converter controls. Figure 3.14 shows the system frequency responses and RoCoF values for Config. II and Config. III under such a contingency. It illustrates that the converter unit increases the frequency nadir from 47.9 Hz for Config. II to 48.3 Hz for Config. III. Regarding the capacity to limit RoCoF, the maximum RoCoF in Config. II and Config. III varies the following way:

- from 0.83 Hz/s to 0.76 Hz/s for G2
- from 0.85 Hz/s to 0.76 Hz/s for G3
- from 0.82 Hz/s to 0.77 Hz/s for G6
- from 0.88 Hz/s to 0.76 Hz/s for G7
- from 0.86 Hz/s to 0.78 Hz/s for G10

Frequency oscillations are also improved since there is a decrease of the transient duration from 75 s to 40 s. Figure 3.15 shows the active power injected by the converter unit. As expected, for both grid-following and grid-forming controls, the injected active power tracks frequency deviations accordingly with their droop coefficients.

Figure 3.16 shows the converter voltage, the PCC voltage and the reactive power injected by the converter-interfaced units for *Case 2*. Figure 3.16a and Figure 3.16b show the magnitudes of converter voltage V_f and the PCC voltage V_g, respectively. Similarly to *Case 1*, it can be observed that, after the contingency, there is a voltage sag within 500 ms for both grid-forming and grid-following units. The grid-following unit experiences a higher drop (i.e., decrease 5.5% and 8.7% of nominal voltage for converter voltage and PCC voltage, respectively) than the grid-forming units (i.e., decrease of 4.2% and 7.5% of nominal voltage for converter voltage and PCC voltage, respectively). The reactive power before and after the transformer are shown in Figure 3.16c and Figure 3.16d, respectively. Similar results are observed as in *Case 1*: 1) the change of reactive power before transformer are very similar for the grid-forming and grid-following controls, i.e., $\Delta Q_{GFM1} = 0.32$ p.u., $\Delta Q_{GFM2} = 0.31$ p.u. and $\Delta Q_{GFL} = 0.30$ p.u., whereas the magnitude of converter voltage for the grid-following unit exhibits considerably larger decrease than the ones for the grid-forming units; 2) the reactive power after the transformer injected by the grid-forming units are much higher than the one by the grid-following unit. As specifically analyzed in *Case 1*, the grid-forming units, operating as voltage sources, perform better in maintaining the transient magnitude and phase angle of the converter voltage V_f. It is shown in Figure 3.16e that, within the first 200 ms after the contingency, the maximum angle difference between the converter voltage and the PCC voltage for the grid-forming units (0.046 rad) are much higher than the one for the grid-following unit (0.030 rad).

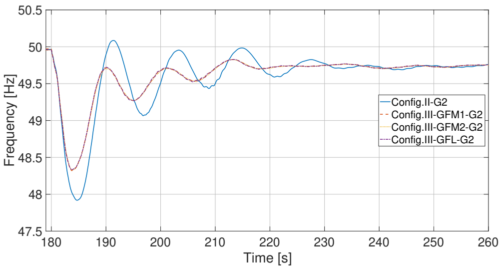

(a) Frequency for G2

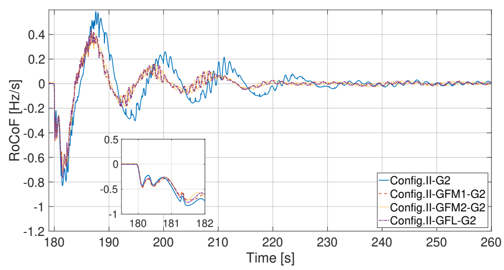

(b) RoCoF for G2

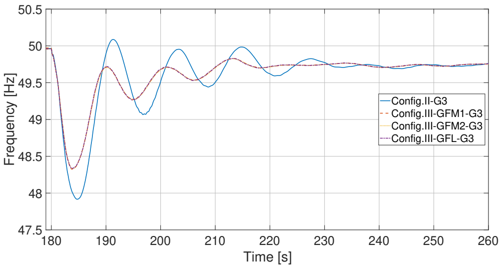

(c) Frequency for G3

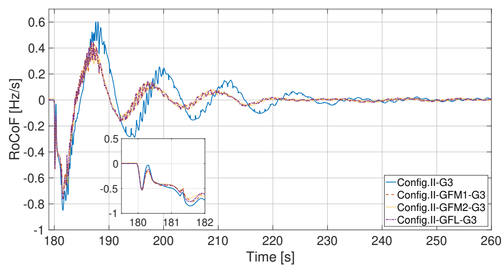

(d) RoCoF for G3

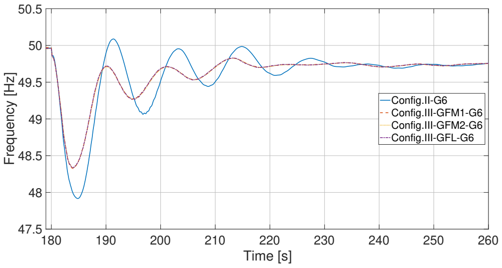

(e) Frequency for G6

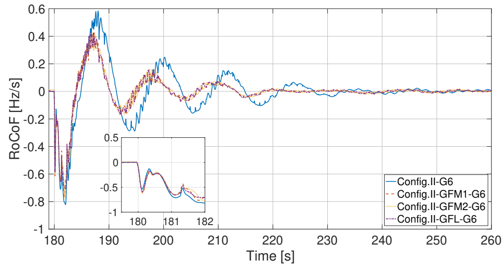

(f) RoCoF for G6

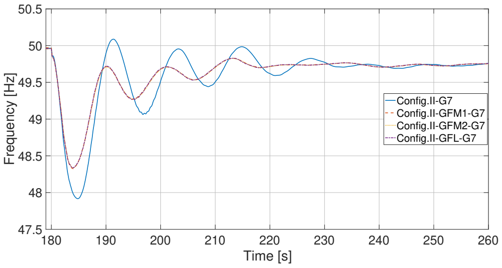

(g) Frequency for G7

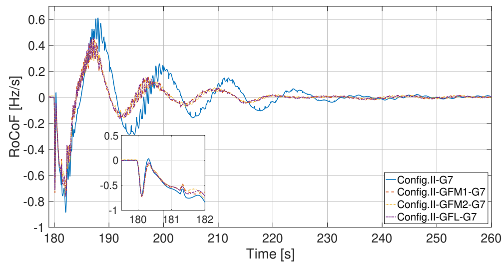

(h) RoCoF for G7

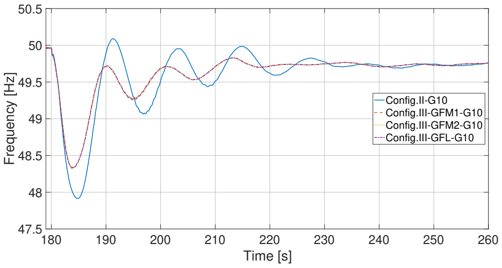

(i) Frequency for G10

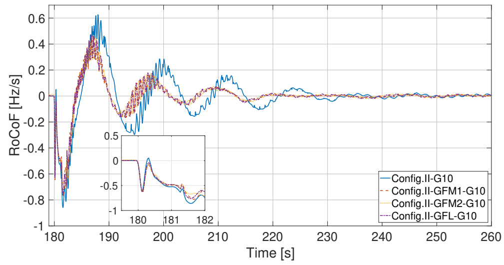

(j) RoCoF for G10

Figure 3.14 – Frequency and RoCoF of low-inertia 39-bus power grids for *Case 2*.

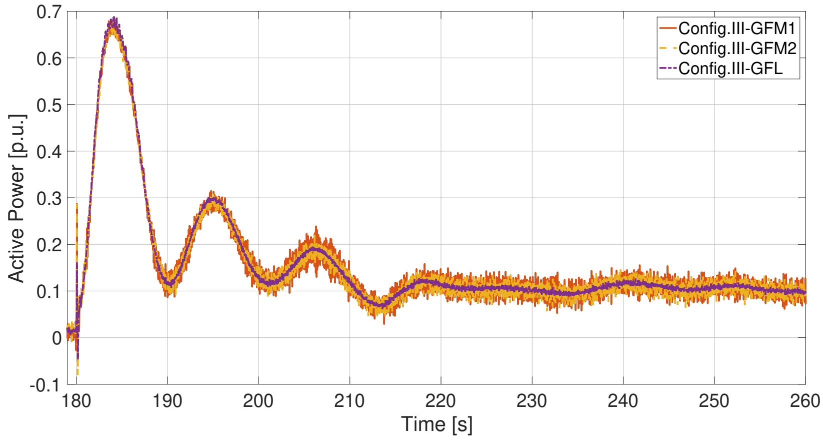

Figure 3.15 – Active power injected by converter-interfaced BESS for *Case 2*

Figure 3.17 shows converter DC voltage, DC current, and battery SOC for *Case 2*. As for the previous *Case 1*, the DC voltage varies as a function of DC current and the SOC of BESS decreases as a result of the BESS frequency regulating action.

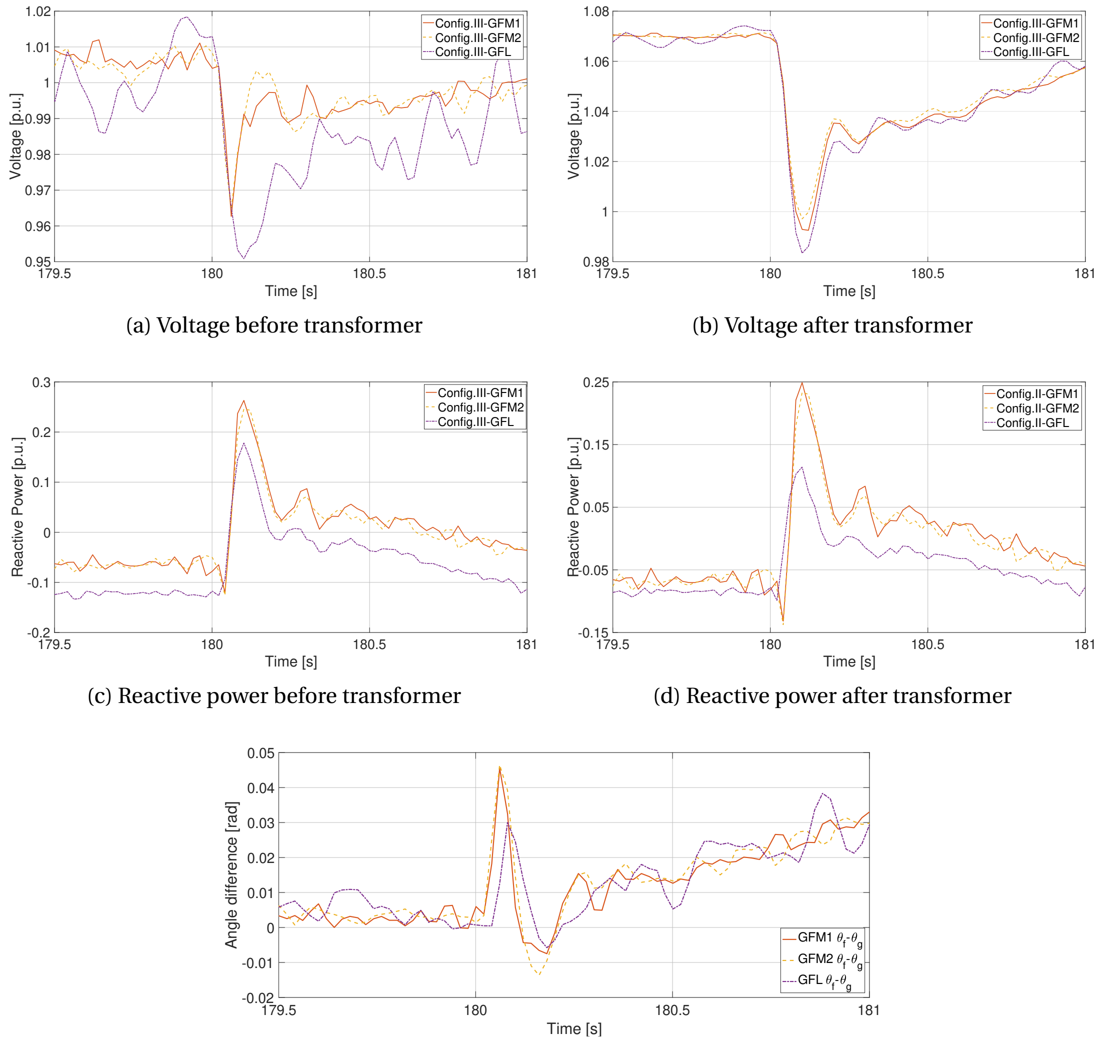

(a) Voltage before transformer

(b) Voltage after transformer

(c) Reactive power before transformer

(d) Reactive power after transformer

(e) Voltage angle difference between the two sides of converter's transformer

Figure 3.16 – Voltage before the transformer (i.e., V_f in Figure 3.11), voltage after the transformer (i.e., V_g in Figure 3.11), reactive power before and after the transformer (i.e., Q_{LV} and Q_{MV} in Figure 3.11, respectively), and voltage angle difference between the two sides of the transformer (i.e., $\theta_f - \theta_g$) for *Case 2*.

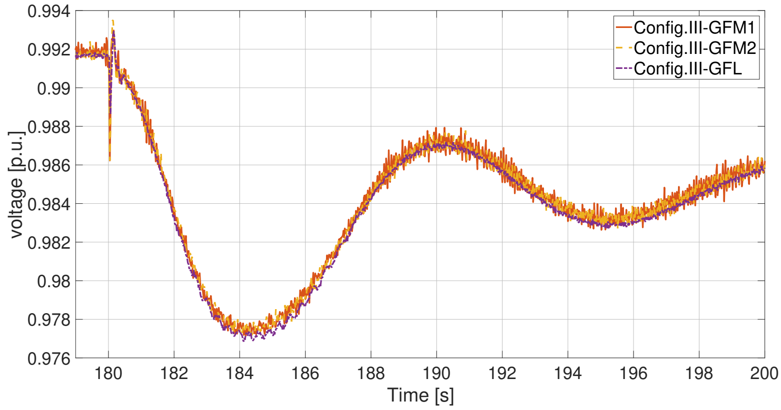

(a) BESS DC voltage

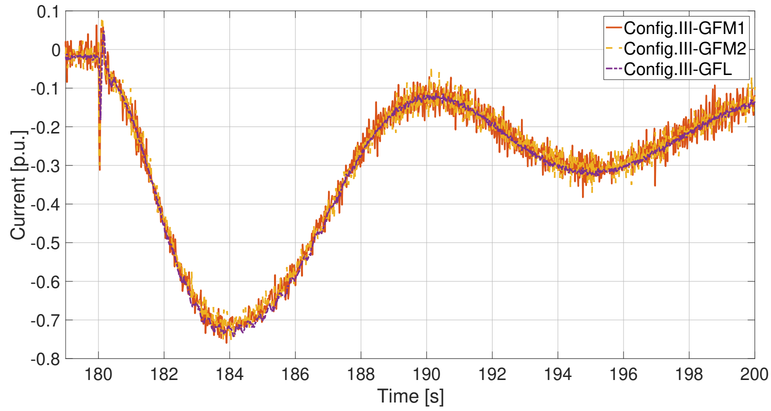

(b) BESS DC current

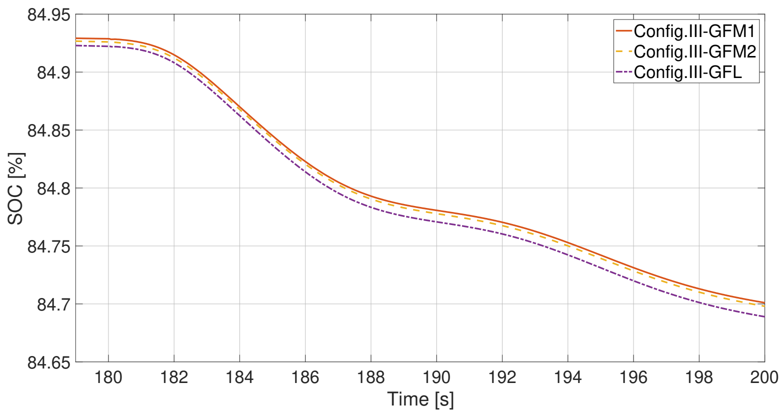

(c) BESS SOC

Figure 3.17 – Converter DC voltage, DC current and BESS SOC in Config. III for *Case 2*.

3.5 Sensitivity Analysis

A sensitivity analysis is conducted to evaluate the system frequency response for different values of the controller's critical parameters. Regarding the grid-forming controls, the critical parameter to be investigated is the inertia constant H, which is equal to $\frac{1}{2\omega_{LP} m_p}$. As for the grid-following control, the influence of the low-pass filter inside the PLL (see Figure 3.6) is investigated as it has impact on the measured frequency. To excite the converter controls' response, the same contingency as in *Case 1*, i.e., tripping of generation G6, is considered for different converter control parameters.

For the grid-forming controls, in addition to the inertia constant H_{GFM} = 0.3185 s used in *Case 1*, two larger inertia constants (i.e., 0.7958 s and 1.5915 s) are considered. As for the grid-following control, in addition to the cut-off frequency ω_{LF} = 25 Hz implemented in *Case 1*, two smaller values (i.e., 10 Hz and 5 Hz) are selected. Figure 3.18 shows the post-contingency RoCoF for Config. III with the grid-forming units and for Config. III with the grid-following unit. Indeed, the values of post-contingency RoCoF are presented to better highlight the differences of the system frequency performance.

As shown in Figure 3.18a, 3.18c, 3.18e, 3.18g, and 3.18i, for the grid-forming controls, the increase of inertia constant enhances the converter's capability to limit the RoCoF, thanks to the inertia effect emulated by the controllers. Figure 3.19a shows that a large amount of active power is injected into the low-inertia system as a result of the inertia effect embedded in the controllers. For both grid-forming controls, a higher inertia constant corresponds to higher active power and energy injected into the system, which consequently results in a better containment of the RoCoF. It is also observed that when lower H_{GFM} (i.e., 0.3185 s and 0.7589 s) are used the GFM 2 injects higher active power than the GFM 1. Whereas, when high H_{GFM} (i.e., 1.5915 s) are implemented, the GFM 1 injects higher active power to the system. Quantitatively, the peak value of the active power for grid-forming with coupled functionalities with H_{GFM} = 0.3185 s, H_{GFM} = 0.7958 s, and H_{GFM} = 1.5915 s are 0.344 p.u., 0.435 p.u. and 0.507 p.u., respectively, whereas the peak value of the active power for grid-forming with decoupled functionalities with H_{GFM} = 0.3185 s, H_{GFM} = 0.7958 s, and H_{GFM}= 1.5915 s are 0.400 p.u., 0.460 p.u. and 0.470 p.u, respectively.

As shown in Figure 3.18b, 3.18d, 3.18f, 3.18h, and 3.18j, for the grid-following control, increasing the cut-off frequency of the low-pass filter in the PLL improves the converter's capability to limit the RoCoF. This is because a higher cut-off frequency of the PLL low-pass filter allows to capture faster frequency dynamics, therefore enabling the converter to react faster to the frequency decrease after the contingency. As it is also observed in Figure 3.19b, the grid-following controller with ω_{LF} = 25 Hz is the fastest.

In Figure 3.19, it is shown that the active power injected by the grid-forming units is significantly higher than the one of the grid-following unit, especially, for the grid-forming units with higher inertia constants (i.e., H_{GFM} = 0.7958 s and H_{GFM} = 1.5915 s). In order to have a general comparison of the RoCoF performance between the grid-forming and the grid-following units, the mean values of the RoCoF for all the generators are computed and plotted in Figure 3.20. It can be seen that, overall, grid-forming control outperforms the grid-following control achieving lower RoCoF. On one hand, the grid-forming units with the lowest inertia constant (i.e., H_{GFM} = 0.3185 s) result in similar RoCoF performance as the grid-following unit. On the other hand, when higher inertia constants are used, the grid-forming units performs better than the grid-forming unit.

3.6 Conclusions

This Chapter investigates the impact of converter-based BESS on the post-contingency dynamics of a low-inertia grid that interfaces a mix of synchronous machines and power-electronics-interfaced wind turbines. To this end, three 39-bus power system configurations are proposed as an extension of the IEEE 39-bus benchmark power system. The first one corresponds to the original benchmark network. The second configuration replaces four synchronous machine-based power plants with wind power plants based on type-III wind turbines. The third configuration is identical to the second, with the exception of including a converter-interfaced BESS. Correspondingly, we built three full-replica dynamic models executed on a real-time simulator to reproduce the same contingencies and conduct post-contingency analysis with respect to the system dynamics.

The simulation results verified the substantial influence of inertia reduction on the post-contingency dynamics of the power system and quantitatively proved that the connected converter-based units, implemented with the PLL-free grid-forming controls or the grid-following control with supporting mode, can assist in limiting the frequency decreasing and in damping the grid frequency oscillations.

The performance of the grid voltages at the PCC of the converter has demonstrated the benefit of the grid-forming converters to maintain the PCC voltage during electromechanical transients. The sensitivity analysis has quantified how the inertia constant of the grid-forming controllers positively influences the post-contingency frequency containment. Furthermore, it has been shown that a higher cut-off frequency of the PLL low-pass filter allows a faster and higher active power injected by grid-following converters to respond to the frequency decreasing after the contingency.

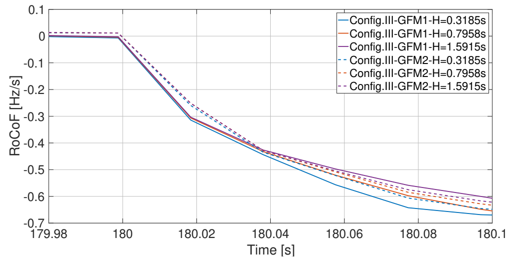

(a) RoCoF for G2

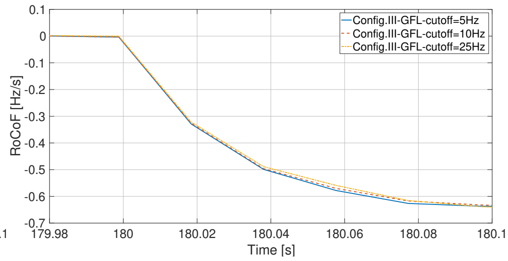

(b) RoCoF for G2

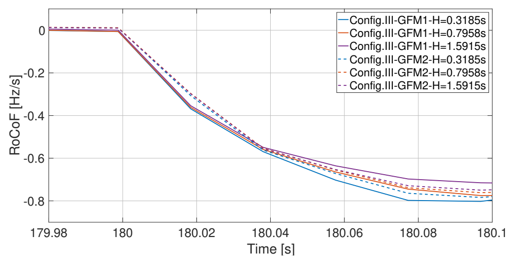

(c) RoCoF for G3

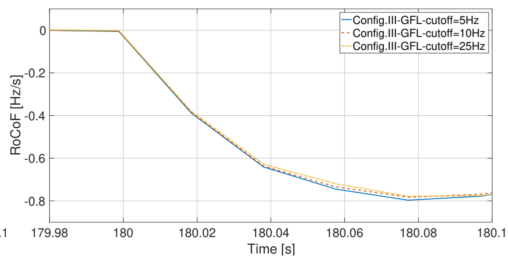

(d) RoCoF for G3

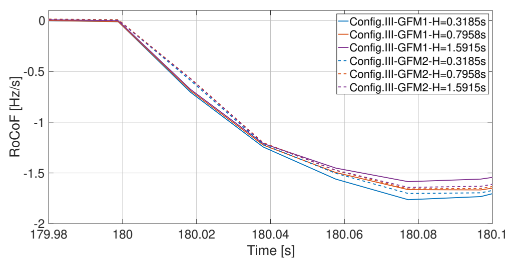

(e) RoCoF for G4

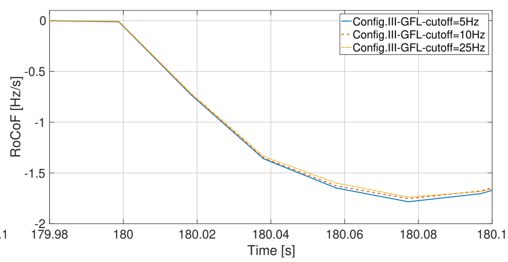

(f) RoCoF for G4

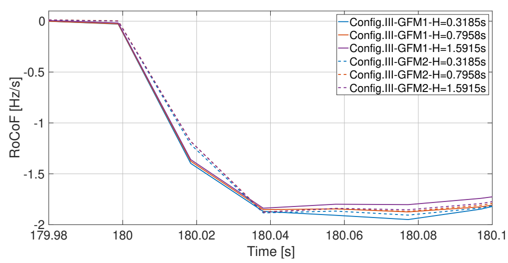

(g) RoCoF for G7

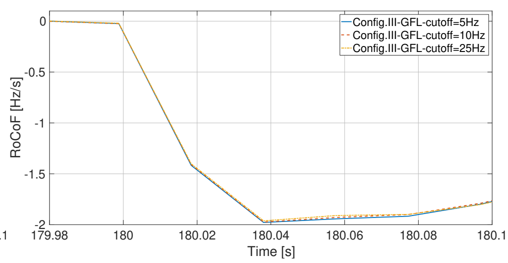

(h) RoCoF for G7

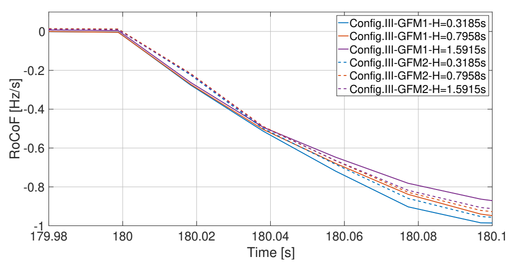

(i) RoCoF for G10

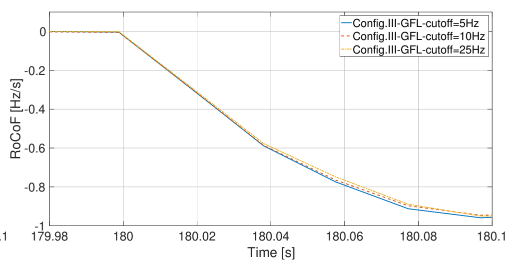

(j) RoCoF for G10

Figure 3.18 – RoCoF for Config. III with grid-forming and grid-following converters in the sensitivity analysis.

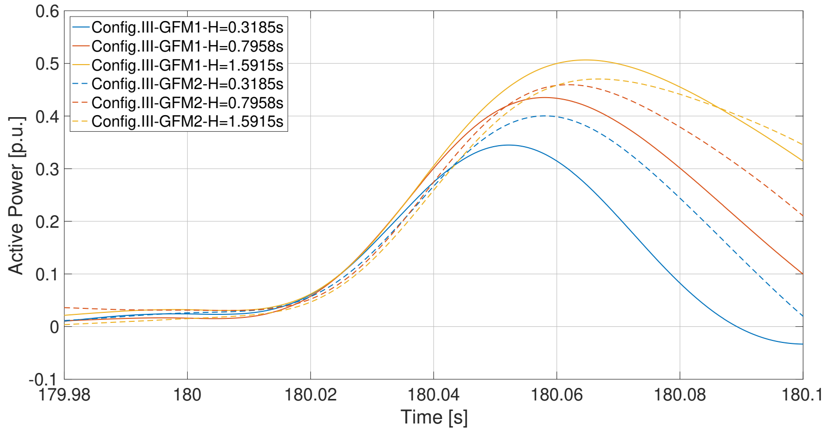

(a) Active power injected by grid-forming units

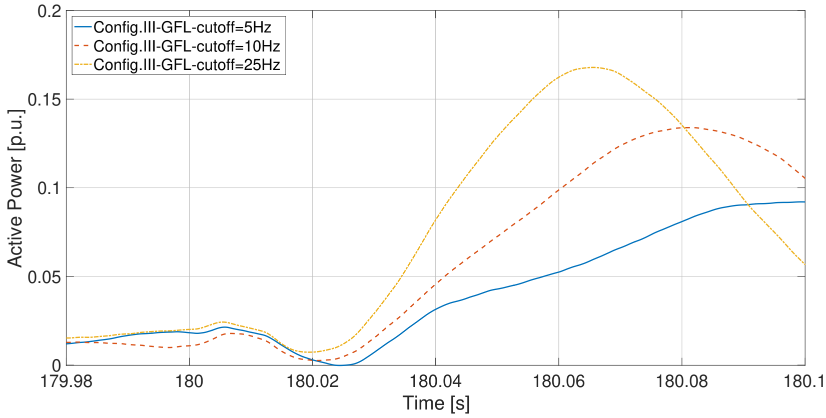

(b) Active power injected by grid-following unit

Figure 3.19 – Post-contingency active power injection by converter-interfaced BESS in the sensitivity analysis.

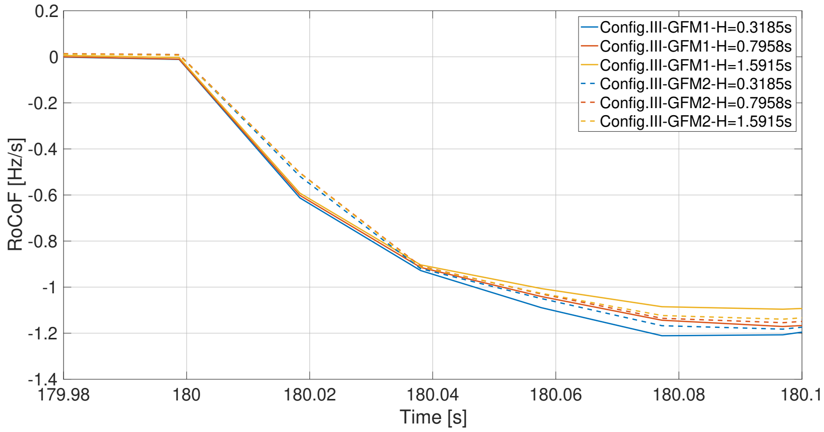

(a) Average RoCoF for Config. III with the grid-forming converters

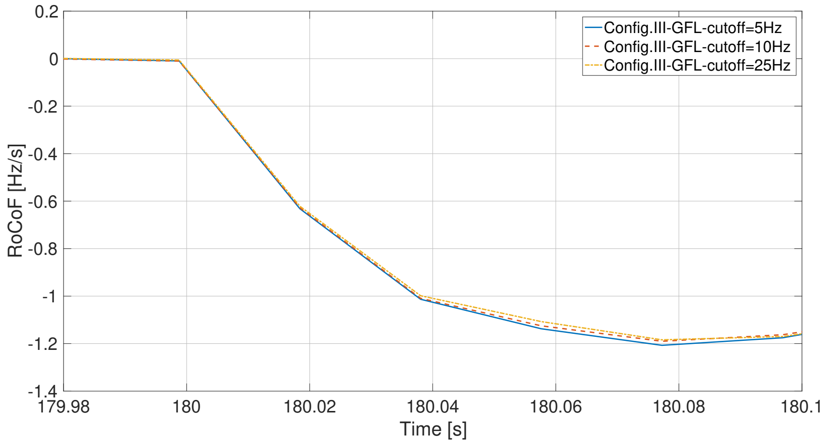

(b) Average RoCoF for Config. III with the grid-following converter

Figure 3.20 – Average RoCoF of all the synchronous generators for Config. III with grid-forming and grid-following converters in the sensitivity analysis.

4 Assessment of the Impact of Converter-interfaced BESS to Frequency Regulation in Low-inertia Power Grids

This Chapter quantitatively assesses the impact of large-scale BESSs on frequency regulation in low-inertia power grids under regular daily operation and compares the performance of grid-forming and grid-following control modes. Numerical analyses are conducted by means of the detailed dynamic models of the low-inertia IEEE 39-bus power grids where fully characterized models of stochastic generation and demand are considered. In order to reproduce a practical operative context, a comprehensive benchmark framework is proposed to enable daily long simulations where reserve levels for frequency containment and restoration are allocated considering the current practice of a TSO in Europe. Numerical analyses on various metrics applied to grid frequency show that grid-forming outperforms grid-following control mode.

The Chapter includes results of publication [107].

4.1 Introduction

The significant growth of converter-interfaced renewable generation and the displacement of conventional synchronous generators in power systems determine lower grid inertia levels and call for a review of frequency containment concept and the identification of assets capable of maintaining the system power balance [108, 109]. BESSs, characterized by large ramping rates, may play a key role in maintaining adequate frequency performance of low-inertia power grids even during daily normal operating conditions. Within this context, it is of fundamental importance to quantitatively evaluate the benefit of converter-interfaced BESSs to normal frequency regulation in low-inertia grids.

Chapter 3 has quantitatively demonstrated that, during contingency, the converter-interfaced BESS provides important support in limiting the frequency decreasing, reducing RoCoF, and damping the frequency oscillations. On the other hand, this Chapter aims to identify the impact of the converter-interfaced BESSs on frequency regulation in low-inertia power grids in consideration of standard daily operating scenarios.

The simulation framework developed in this Chapter is based on the low-inertia 39-bus power grids proposed in Chapter 3, Section 3.2. The detailed dynamic model of low-inertia 39-bus power grids is coupled with a day-ahead schedule layer to statistically evaluate the system frequency containment via 24-hour long time-domain simulations. To reproduce a realistic grid operative scenario for the numerical analyses, power reserves for frequency containment and restoration are allocated with respect to the procedure adopted nowadays by a TSO. This day-ahead scheduling stage leverages a unit commitment formulation fed by the forecast of renewable generation and demand computed with state-of-the-art methods.

This comprehensive benchmark framework provides a way to assess the frequency containment performance of power systems under daily operation. A quantitative comparison of the impact of grid-forming vs. grid-following converter-interfaced BESS on the system frequency containment of low-inertia power grids is obtained through suitably defined frequency metrics.

This Chapter is structured as follows. Section 4.2 introduces the proposed simulation framework. Section 4.3 describes operating schedules for day-long simulations. Section 4.4 presents the frequency controls implemented in the low-inertia 39-bus power grids. Section 4.5 presents test cases and metrics for system frequency containment. Section 4.6 illustrates and discusses simulation results, and Section 4.7 concludes this Chapter.

4.2 Simulation Framework

The proposed simulation framework has two layers: a scheduling stage and real-time simulations. The former allows to size power reserve requirements and reproduce realistic operative scenarios for the real-time simulations. The latter is used to evaluate the performance of the converter controllers by analysing the whole grid dynamic behavior. Figure 4.1 illustrates the overall simulation process, where L and W denote measurements of power demand and wind generation, respectively. The process starts by dividing the measurements into two subsets, one for training the forecasting and model, and one to feed the real-time simulations. Measurements and forecasts are discussed in 4.3.1.

Accordingly, the demand profile denoted by the sequence $L = \{l_1, l_2, ..., l_n\}$ is separated as $L_1 = \{\tilde{l}_1, \tilde{l}_2, ..., \tilde{l}_{n-24}\}$ and $L_2 = \{l_{n-23}, l_{n-22}, ..., l_n\}$, and the wind generation profile denoted by the sequence W=$\{w_1, w_2, .., w_m\}$ is separated as $W_1 = \{\tilde{w}_1, \tilde{w}_2, ..., \tilde{w}_{m-24}\}$ and $W_2 = \{w_{m-23}, w_{m-22}, ..., w_m\}$[1]. L_2 and W_2 are directly applied to the RTS to be reproduced in the day-long simulations. In the day-head schedule layer, L_1 and W_1 are sent to the forecasting models (described in

[1]It should be noted that $l_i = \{l_{i,1}, l_{i,2}, ..., l_{i,3600}\}$ is the 1-second resolution demand set for hour i and $\tilde{l}_i$ is the average demand of hour i. w_i and $\tilde{w}_i$ are likewise the 1-second resolution wind generation set and the average wind generation for hour i, respectively.

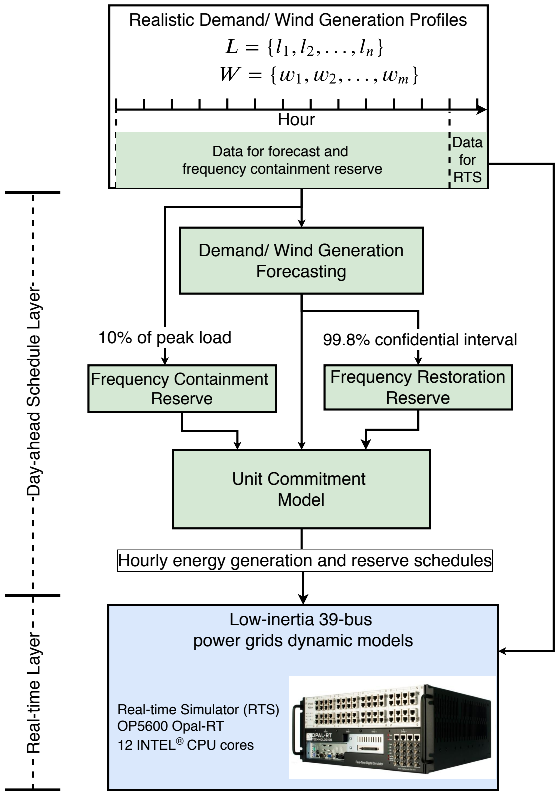

Figure 4.1 – Simulation framework.

Section. 4.3.1) to obtain the demand and wind generation forecasts, which are then used to compute the frequency restoration reserve, with the procedure described in Section 4.3.2. Additionally, L_1 is also used for computing the frequency containment reserve which is considered as 10% of peak load (described in Section 4.3.2). Then, a unit commitment model determines optimal hourly generation and reserve schedules accounting for the demand and wind generation forecasting results, the frequency containment and restoration reserves, as well as the power network and operational constraints (detailed in Section 4.3.3). Finally, a real-time simulator (RTS) executes the time-domain dynamic models of the low-inertia 39-bus power grids. The inputs of the dynamic models are (i) the demand and wind generation profiles (i.e., L_2 and W_2) with a 1-second resolution and (ii) the hourly energy generation and reserve schedules provided by the unit commitment model to be realized by synchronous generators. There are two ways to couple the inputs of the dynamic model with the real-time simulator:

- directly embed the input profiles in the MATLAB/Simulink model[2] using look-up table blocks that map input values to output values. More specifically, the look-up table blocks update the set-points of demand and wind generation every second and update

[2]Since the time-domain dynamic models of the IEEE 39-bus benchmark network and its low-inertia configurations are all built in MATLAB/Simulink, hereby we refer to it as Simulink model.

the set-points of synchronous generators every hour, according to their corresponding input profiles. In this way, the input profiles are part of the Simulink model.

- Use the block OpFromFile provided by RT-LAB[3] such that the profiles can be directly loaded into the RTS. In this case, the input datasets are not part of the Simulink model. Instead, the datasets of the input profiles and the Simulink model are loaded separately into the RTS. The block OpFromFile reads a selected dataset (loaded in RTS) before the simulation execution and outputs the values in the sequence indicated in the dataset during the simulation.

It is also worth to note that, in the low-inertia 39-bus power grid, all the devices (including type-III wind power plants, synchronous generators, converter-interfaced BESS and frequency and voltage-dependent dynamic loads) are fully modelled in time domain to make the simulations as close as possible to the realistic scenario. Moreover, the converter is modeled by switching devices (i.e., IGBT and diodes) in order to adequately capture the dynamics due to the interaction between the grid-forming/grid-following converter and the system frequency. Given the high computational complexity and the microsecond-scale time-integration step required by the high sampling frequency devices[4], a real-time simulation platform is adopted. This Chapter leverages the dynamic models of low-inertia 39-bus power grids proposed in Chapter 3 and runs real-time simulations in the same platform, i.e., executed the OPAL-RT eMEGAsim RTS.

In the following Section 4.3 and Section 4.4, the demand and wind generation forecasting, the system reserves allocation, and the frequency controls implemented in the low-inertia 39-bus power grids are described.

4.3 Operating Schedules for Day-long Simulations

4.3.1 Measurements and Forecasting

Although it is not a specific contribution of this Thesis, forecasting stochastic generation and demand is a necessary element of the process and thus briefly discussed here below.

Wind power

Wind production measurements are at a 1-second resolution and refer to two real wind farms with a nominal capacity of 17 MW and 50 MW located in the north of France. Measurements are scaled proportionally to match the capacity of the four wind farms considered in the case study (i.e., 1500 MW, 1200 MW, 750 MW and 600 MW). Forecasts are computed in terms of prediction intervals, which express the range where the realization is predicted to happen with

[3]A platform developed by OPAL-RT to interface with its RTS.

[4]In this study, the high sampling frequency devices include Pulse Width Modulation (PWM) generator of the converter and Phase Measurement Units (PMUs).

a certain confidence level, and thus are the suitable format to evaluate reserve requirements. For the reasons that will be discussed in 4.3.2, the target confidence level is 99.8%. Prediction intervals of wind generation are computed with a quantile regression forest model from the existing literature [110, 111] and trained on historical numerical weather predictions and plant production data. Figure 4.2 shows the day-ahead hourly wind forecast and the corresponding prediction intervals at 99.8% confidence level.

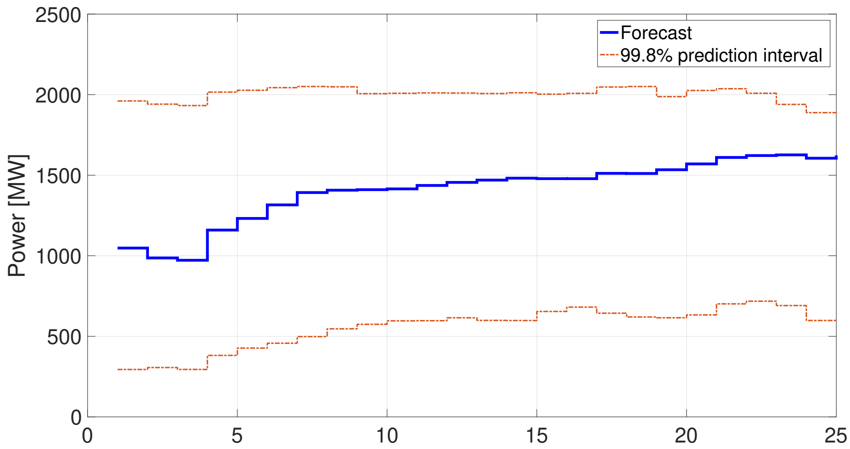

Figure 4.2 – Aggregated day-ahead wind forecast and 99.8% prediction intervals.

Power demand

The active power measurements are adapted from a monitoring system based on PMUs installed in the 125 kV sub-transmission system of Lausanne, Switzerland [112]. Reactive power is computed by assuming a constant power factor for the loads. Since the demand level of Lausanne is smaller than the demand level of the IEEE 39-bus benchmark power grid, the load profiles are scaled-up to match the rating power of the 19 loads in the 39-bus power grid. Specifically, 7 different load profiles (i.e., corresponding to measurements at different network buses of Lausanne) and their combinations are used such that the demand profiles for the 19 loads are all different. Forecasting is based on a Seasonal Auto Regression Integrated Moving Average (SARIMA) model with seasonality order of 24 hours, seasonal AR order of 5 (non-zero terms at lags 1, 2, 3 and 5), AR order of 1, MA order of 18 (non-zero terms at lags 1, 6 and 18), and a trend difference order of 1. The 99.8% prediction interval is obtained using the mean square error of the foretasted responses, by assuming the forecast errors are normally distributed. Figure 4.3 shows the day-ahead hourly demand forecast and the corresponding 99.8% prediction intervals.

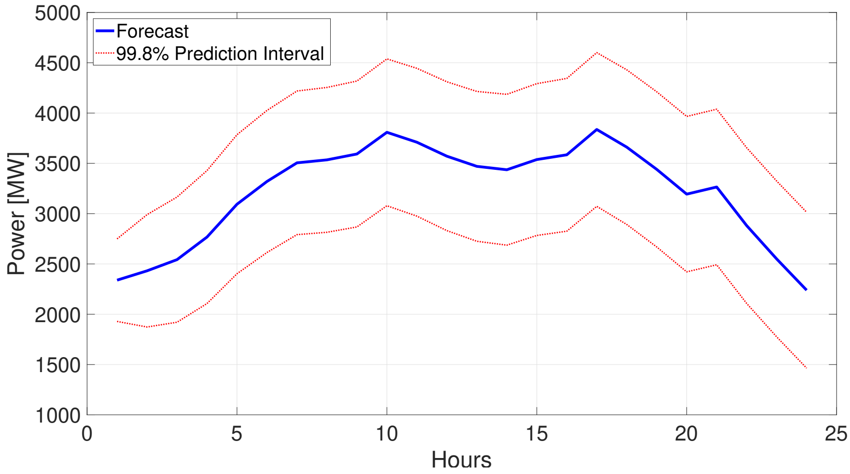

Figure 4.3 – Aggregated day-ahead demand forecast and 99.8% prediction intervals.

4.3.2 System Reserves

Power reserves for frequency containment and restoration are calculated referring to the norms of the Swiss national TSO, Swissgrid. Both are allocated as symmetric products and calculated as described in the following of this sub-section [113, 114].

Frequency containment reserve

Typically, national TSOs within a large interconnected system procure reserves for frequency containment proportionally to the size of their systems. Swissgrid, as the Swiss TSO within the electricity grid of continental Europe (UCTE), procures reserve as the pro rata of its maximum load compared to the total UCTE one [115]. Since our low-inertia 39-bus power system is assumed to be non-interconnected, the frequency containment reserve is set as 10% of the peak load, ±500 MW, using the deterministic notion proposed in [116].

Frequency restoration reserve

ENTSO-E operation handbook recommends attaining zero frequency error with a probability of 99.8% [117]. According to this principle, and since grid imbalances are caused by stochastic generation and demand, the power reserve for frequency restoration is dimensioned by considering 99.8% prediction intervals of the wind generation and power demand. Figure 4.4 shows, in addition to the 99.8% prediction intervals of wind and demand already discussed, the allocated power reserve for frequency restoration. The total positive, R_h^+ (negative, R_h^-), reserve at hour h is the sum of the upper (lower) quantile of the wind and demand prediction intervals. However, since the power reserve is symmetric, the applied total secondary frequency reserve at each hour is $R_h = \pm\max\{|R_h^+|, |R_h^-|\}$.

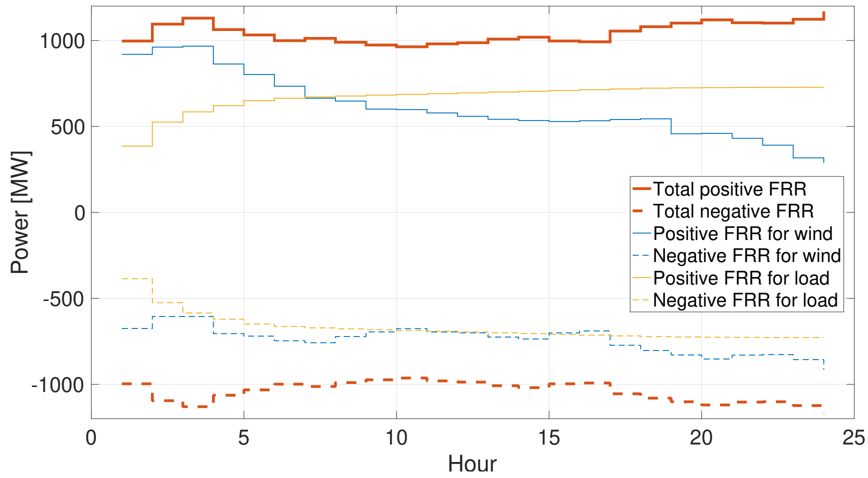

Figure 4.4 – Frequency restoration reserve considering 99.8% prediction intervals for wind generation and power demand.

4.3.3 Unit Commitment for Generation and Reserve Scheduling

A security constrained unit commitment (SCUC) model is considered for scheduling generation, frequency containment and restoration reserves based on a DC power flow to model the transmission grid's capability. The SCUC model is used as a replacement for the day-ahead market set-up to schedule the active power profiles. The BESSs are treated here as an additional frequency regulation service provider. For the sake of a fair comparison in the results section, they are not included in the SCUC (where only synchronous generators are included) because this would determine different operating conditions for the generators, making it difficult to compare the system performance in the cases with and without the BESS. In this way, the exclusion of the BESS from the SCUC produces the same boundary conditions on the system, allowing to quantify the impact of the BESS on the system dynamics.

The objective of the SCUC is to minimize the economic cost of energy generation and reserve procurement considering the power network constraints, operational (security) constraints, load and renewable energy generation forecast, and reserve requirements. The SCUC model (4.1) is a mixed integer linear programming problem and expressed in (4.1).Its formulation reads as:

$$\underset{\Omega}{\text{Minimize}} \quad Cost^{uc} = E_{cost} + Up_{cost} + Dw_{cost} + Rev_{cost}$$

subject to

$$E_{cost} = \sum_{n,t} \beta_n p_{g_{n,t}} \tag{4.1a}$$

$$Up_{cost} = \sum_{n,t} C_{n,t}^{up} u_{n,t}^{up} \tag{4.1b}$$

$$Dw_{cost} = \sum_{n,t} C_{n,t}^{down} u_{n,t}^{dw} \tag{4.1c}$$

$$Rev_{cost} = \sum_{n,t} C_{n,t}^{reserve} p_{g_{n,t}}^{r} \tag{4.1d}$$

$$p_{g_{n,t}} - p_{d_{n,t}} = \sum_{l} A(n,l) p_{l,t} + G_n \tag{4.1e}$$

$$p_{l,t} = \frac{\theta_{s_{l,t}} - \theta_{r_{l,t}}}{X_l} \tag{4.1f}$$

$$u_{n,t}^{on} Ramp_{n,t}^{dw} \leq p_{g_{n,t}} - p_{g_{n,t-1}} \leq u_{n,t}^{on} Ramp_{n,t}^{up} \tag{4.1g}$$

$$u_{n,t}^{on} - u_{n,t-1}^{on} = u_{n,t}^{up} - u_{n,t}^{dw} \tag{4.1h}$$

$$u_{n,t}^{up} + u_{n,t}^{dw} \leq 1 \tag{4.1i}$$

$$Rev_t \leq \sum_{n} p_{g_{n,t}}^{r} \tag{4.1j}$$

$$u_{n,t}^{on} p_{g_n}^{min} \leq p_{g_{n,t}} \leq u_{n,t}^{on} p_{g_n}^{max} \tag{4.1k}$$

$$p_{g_n}^{min} \leq p_{g_{n,t}} + p_{g_{n,t}}^{r} \leq p_{g_n}^{max} \tag{4.1l}$$

$$p_l^{min} \leq p_{l,t} \leq p_l^{max} \tag{4.1m}$$

$$\theta_n^{min} \leq \theta_n - \theta_{n'} \leq \theta_n^{max}, \forall n \in N_{PV}, n^{'} \in N_{slack} \tag{4.1n}$$

$$\theta_l^{min} \leq \theta_{s_{l,t}} - \theta_{r_{l,t}} \leq \theta_l^{max} \tag{4.1o}$$

$$\left\{u_{n,t}^{on}, u_{n,t}^{up}, u_{n,t}^{dw}\right\} \in \{0,1\} \tag{4.1p}$$

The objective cost function $Cost^{uc}$ includes the energy generation cost (linear) E_{cost}, generator start-up cost (linear) Up_{cost}, generator shut-down cost (linear) Dw_{cost} and reserve cost Rev_{cost}. $\Omega = \{p_{g_{n,t}}, u_{n,t}^{on}, u_{n,t}^{up}, u_{n,t}^{dw}\}$ is the set of decision variables. β_n is the cost parameter of energy generation. $C_{n,t}^{up}$, $C_{n,t}^{down}$, $C_{n,t}^{reserve}$ are the cost parameters of generator start-up, shut-down and reserve. $p_{g_{n,t}}$ is the energy generation of the generator at bus n and time step t. $p_{d_{n,t}}$ is the active power load forecast. $p_{l,t}$ is the active power flow of transmission line l. $A(n,l)$ is the network matrix with $A(n,l) = 1$ if n is the sending end of transmission line l and $A(n,l) = -1$ if n is the receiving end of transmission line l. G_n is the shunt conductance at bus n. As we are using the DC power flow, the voltage amplitudes are assumed equal to $1\,p.u.$ for all the buses. Constraint (4.1e) refers to the active power balance equation. Constraint (4.1f) is the DC power flow equation. $p_{l,t}$ is the power flow through the transmission line l at time step t. $\theta_{s_{l,t}}, \theta_{r_{l,t}}$ are the voltage phase angles at the sending end and receiving end of transmission line l. $u_{n,t}^{on}$ is the unit commitment variable. $u_{n,t}^{up}$ is the unit start-up variable. $u_{n,t}^{dw}$ is the unit shut-down variable. Constraint (4.1g) respects generators ramp-rate bound. $Ramp_{n,t}^{up}$, $Ramp_{n,t}^{dw}$ are the upper and lower bounds of generators' ramp rates. Constraint (4.1h) is the relationship among the generator start-up, shut-down and in-operation variables. Constraint (4.1i) is the bound of start-up and shut-down variables. Constraint (4.1j) is the requirement of total reserve which is equal to the sum of frequency containment and restoration reserves computed in Section 4.3.2. Constraint (4.1k) is the bound for active power generation. Constraint (4.1l) is the bound of reserve (plus energy generation). Constraint (4.1m) is the bound of power flow of the transmission line. Constraint (4.1n) is the phase angle stability bound for all (non-slack bus) generators compared with the slack bus generator. N_{slack} is the set of slack bus generator. N_{PV} is the set of non-slack bus generator. Constraint (4.1o) is the phase angle bound for all transmission line for security consideration. For the unit commitment variables, $\{u_{n,t}^{on}, u_{n,t}^{up}, u_{n,t}^{dw}\} = 1$ means the generator is in-operation, start-up action and shut-down action, respectively. Otherwise, $\{u_{n,t}^{on}, u_{n,t}^{up}, u_{n,t}^{dw}\} = 0$ means the generator is off-operation, no start-up action or shut-down action.

4.4 Frequency Controls Implemented in the Low-inertia 39-bus Power Grids

The dynamic models of the low-inertia 39-bus power grids (i.e., Config, II and Config. III) proposed in Chapter 3 are used for running day-long simulations to assess the system frequency containment performance. The details of the time-domain dynamic model are described in Appendix A. This section highlights the frequency controls, comprising of BESS converter controls and frequency controls on synchronous generation, that are implemented in the low-inertia power grids for the 24-hour operating simulations conducted in this Chapter.

4.4.1 Power Converter Controls

In order to investigate the impact of converter controls on the BESS's performance of improving system frequency containment, the PLL-free grid-forming control with coupled functionalities and the grid-following control operating in grid-supporting mode (introduced in Chapter 3, Section 3.3) are implemented as representatives of *grid-forming* and *grid-following* controls, respectively. For both the grid-forming and grid-following controls, the parameters that allow the best converter contribution to the system frequency containment have been adopted. To this end, according to the sensitivity analysis conducted in Chapter 3, Section 3.5, the inertia constant H_{GFM} =1.5915 s is applied for the PLL-free grid-forming control and the 25 Hz cut-off frequency is applied to the PLL low-pass filter of the grid-following control.

4.4.2 Frequency Controls on Synchronous Generators

The synchronous generators provide both frequency containment and frequency restoration, as shown is Figure 4.5. The parameter R_p is the static droop coefficient for frequency con-

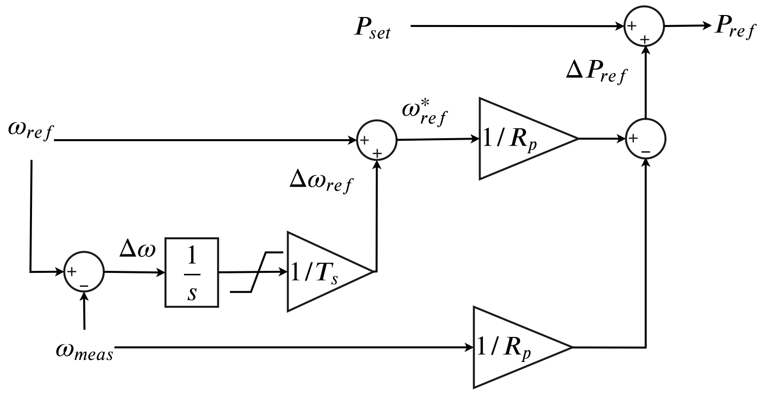

Figure 4.5 – Diagram of the synchronous generator frequency containment and restoration regulators.

Table 4.1 – Cases studied through day-long simulations.

Case	**BESS converter control**	f-p **Gain**
Case 1	No BESS	-
Case 2	Grid-forming	225 MW/Hz
Case 3	Grid-forming	450 MW/Hz
Case 4	Grid-following with supporting mode	225 MW/Hz
Case 5	Grid-following with supporting mode	450 MW/Hz

tainment, T_s is the integration time constant for the frequency restoration regulation, w_{ref} is reference frequency (i.e., nominal frequency), w_{meas} is measured actual frequency, P_{set} is the power set-point scheduled for the generator, and P_{ref} is the power reference for the turbine-governor system. The adopted hydro governor is a typical control design employed in hydro plants [118], detailed in the Appendix A.1.2. As in Chapter 3, the droop coefficient of the frequency containment regulator for each generator is 5%. Regarding the frequency restoration regulation, the adopted integration time constant is $T_s = 120\ s$.

4.5 Test Cases and Metrics for Frequency Containment

4.5.1 Test Cases

For the purpose of comparison, five cases over 24-hour long simulations are investigated, where the same generation and reserve schedules obtained from the SCUC are reproduced. Figure 4.6a and Figure 4.6b show the generation and reserve schedules determined for the day of operations.

Table 4.1 lists the five cases tested over the 24-hour long simulations. *Case 1* is the base configuration with no BESS. *Case 2* and *Case 3* feature a BESS connected to the low-inertia

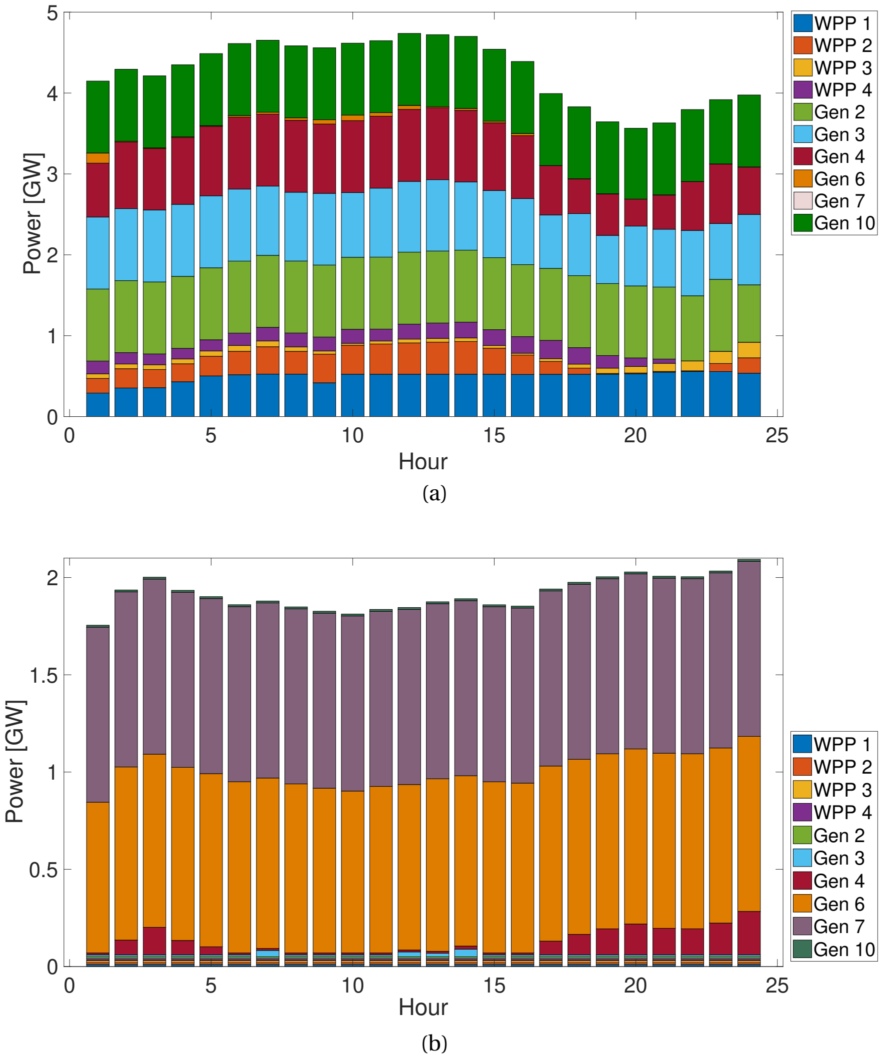

Figure 4.6 – Generation and reserve schedules. Generation schedule (a); Frequency containment and restoration reserve schedule (b).

power grid via a PLL-free grid-forming converter with the $p-f$ droop coefficients of 2% and 1%, corresponding to the $f-p$ control gains of 225 MW/Hz and 450 MW/Hz, respectively. *Case 4* and *Case 5* are the two cases where the BESS is connected to the low-inertia power grid through a grid-following converter with $f-p$ control gains of 225 MW/Hz and 450 MW/Hz, respectively. For the sake of brevity, in the following of this section, the $f-p$ control gain is also used for both grid-forming and grid-following converter.

4.5.2 Metrics

In order to quantitatively evaluate the frequency containment, the following metrics are used.

- Frequency Probability Density Function (PDF), identified using the 24-hour frequency measurements from the 19 simulated PMUs (with a reporting rate of 50 frames per second) located at 19 load buses [119].

- Integral Frequency Deviation (IFD):

$$\text{IFD} = \sum_{i}^{L} \sum_{k=1}^{N} |f_{k,i} - f_0| \tag{4.2}$$

  where L is the total number of loads buses (where PMUs are installed) and N is the total sampling number of frequency measurements for each load.

- Relative Rate-of-Change-of-Frequency (rRoCoF):

$$\text{rRoCoF} = \frac{\Delta f_{pcc}/\Delta t}{\Delta P_{BESS}} \tag{4.3}$$

  where Δf_{pcc} is the difference between one grid frequency sample and the next (once-differentiated value) at the bus where the BESS is connected to, ΔP_{BESS} is the once-differentiated BESS active power, and Δt is the sampling interval.

The frequency PDF and IFD measure grid frequency deviations from the nominal value and are used to assess frequency containment performance. The rRoCoF measures the RoCoF regulation at PCC weighted by the delivered active power of the BESS, thereby this index is independent from the size of the BESS.

4.6 Results

This section presents and discusses the simulation results for the 5 cases listed in Table 4.1. Figure 4.7a shows the system frequency for the 5 cases. The zoomed region shows that the grid frequency dynamics at the beginning of the 15-th hour exhibits a considerable frequency deviation. The cases with a higher $f-p$ control gain attain more frequency containment because of the larger regulating power provided, as visible in the zoomed region of Figure 4.7b. While Figure 4.7 provides a general view of the system frequency responses, the defined metrics allow a better scrutiny of the control performance and will be described next.

4.6.1 Integrated Frequency Deviation

The IFD reported in Table 4.2 shows that the case without BESS (i.e., *Case 1*) scores the highest IFD. In *Case 2* and *Case 3*, IFD decreases by 11.0% and 20.3%, respectively, compared to *Case 1*. In *Case 4* and *Case 5*, IFD decreases by 10.0% and 18.7%, respectively. This is in accordance with the expectation that the higher $f-p$ control gain (i.e., 450 MW/Hz) provides more frequency containment, therefore reducing deviations of the grid frequency.

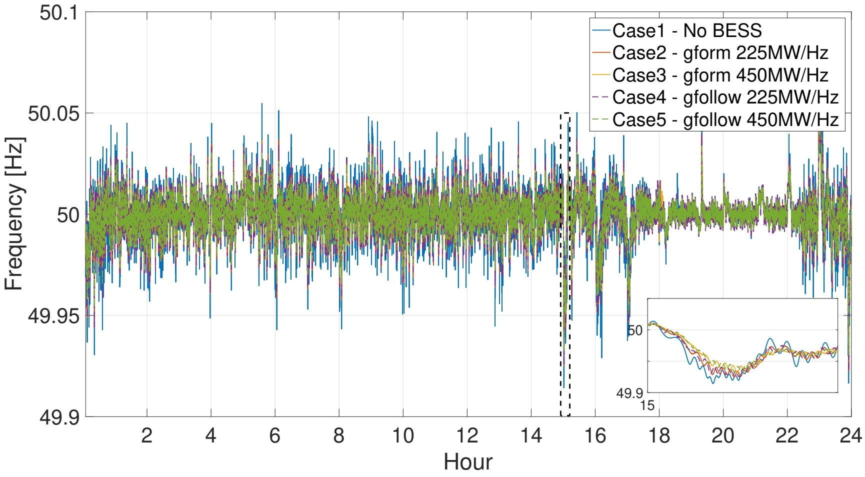

(a)

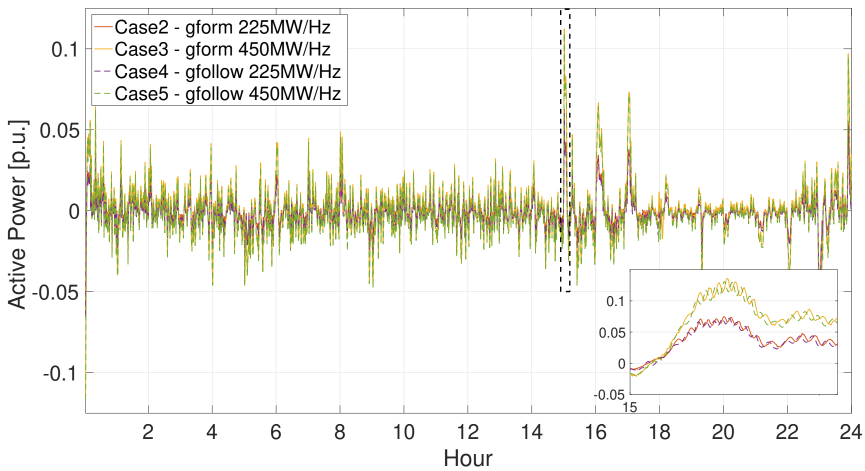

(b)

Figure 4.7 – System frequency and BESS active power. System frequency (represented by the rotor speed of Generator 2) (a); BESS active power (b).

Table 4.2 – Integrated Frequency Deviation and apparent power for the 5 cases.

Case	**IFD [Hz]**	$\sum S_{BESS}$ **[MVA·h]**
Case 1	7.547×10^5	–
Case 2	6.718×10^5	435.5
Case 3	6.015×10^5	442.8
Case 4	6.798×10^5	558.3
Case 5	6.138×10^5	564.3

4.6.2 Probability Density Function of Grid Frequency

Figure 4.8 shows the PDF estimated from the frequency measurements on the 19 loads. The PDF results are consistent with the value of IFD, demonstrating that the higher control gain

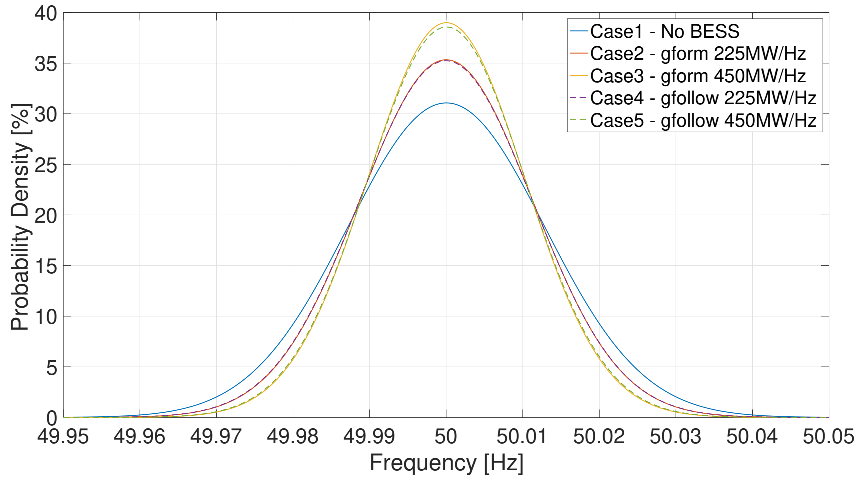

Figure 4.8 – Probability density function for frequency measurements of 19 loads. Standard deviation for each case: σ^{f}_{case1}=0.0128, σ^{f}_{case2}=0.0113, σ^{f}_{case3}=0.0102, σ^{f}_{case4}=0.0113, and σ^{f}_{case5}=0.0103.

results in smaller standard deviation and higher probability at 50 Hz. By comparing *Case 2* and *Case 4*, the two cases with the lowest $f-p$ control control gain, it is observed that the grid-forming and grid-following converters achieve an equivalent increment of performance for frequency containment. After examining the values of IFD and PDF standard deviation for *Case 3* and *Case 5*, it can be observed that, for a higher $f-p$ control gain, the grid-forming converter performs better than the grid-following converter, achieving a 2% reduction of IFD and 1% reduction of PDF standard deviation.

4.6.3 Relative Rate of Change of Frequency

Figure 4.9 illustrates the Cumulative Density Functions (CDFs) of rRoCoF for the larger and smaller $f-p$ gains for both grid-forming and grid-following converter. For the smaller gain in Figure 4.9a, the grid-forming converter performs better than the grid-following converter as it achieves lower RoCoF per Watt of regulating power. The standard deviation of rRoCoF for *Case 2* and *4* are σ^{rRoCoF}_{case2}= 0.0016 and σ^{rRoCoF}_{case4}= 0.0065, respectively. Figure 4.9b shows that also for the larger gain, the grid-forming converter performs better than the grid-following as it achieves smaller frequency rates. In this case, the corresponding standard deviations of rRoCoF are σ^{rRoCoF}_{case3}= 0.0013 and σ^{rRoCoF}_{case5}= 0.0064 for *Case 3* and *5*, respectively.

Figure 4.10 shows the evolution in time of the BESS state of charge (SOC). It is interesting to observe its decreasing trend, that, since the average grid frequency along the day is 50 Hz due to the frequency restoration action, is to ascribe to power losses on the AC- and DC-side filters. Thanks to the high fidelity of the dynamic models, we are capable to numerically quantify the impact of converter controls on the SOC evolution. Since the energy losses are proportional to the apparent power $S_{BESS} = \sqrt{P^2_{BESS} + Q^2_{BESS}}$, Table 4.2 reports the integral of the BESS

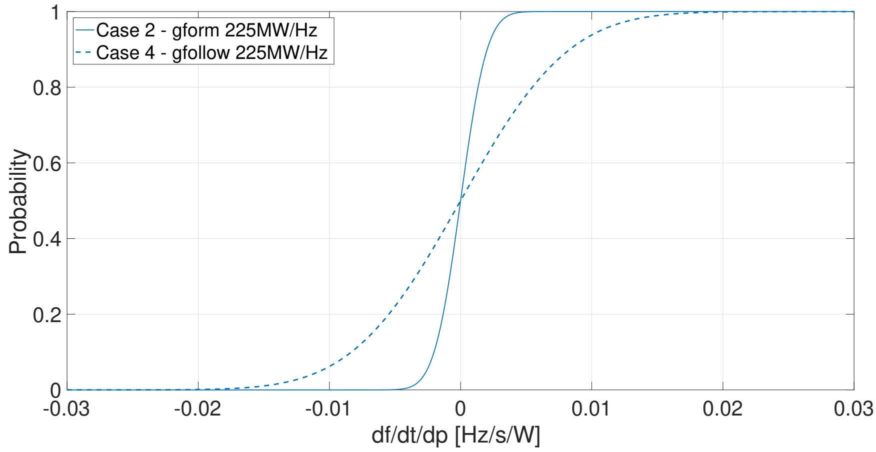

(a)

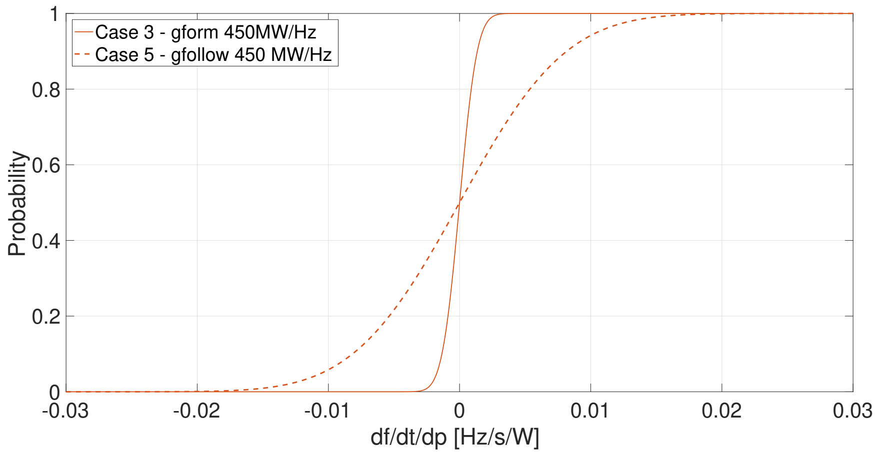

(b)

Figure 4.9 – Cumulative density function (CDF) of rRoCoF. *Case2* and *Case4* (a); *Case3* and *Case5* (b).

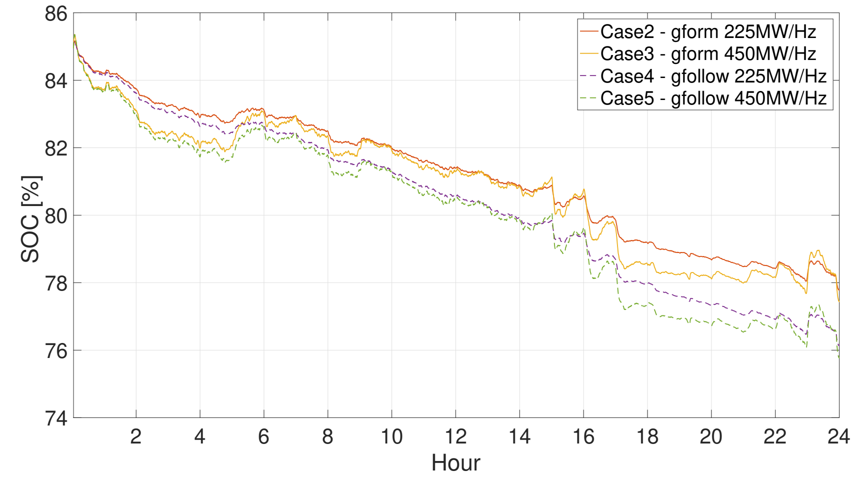

Figure 4.10 – Evolution in time of the battery state of charge.

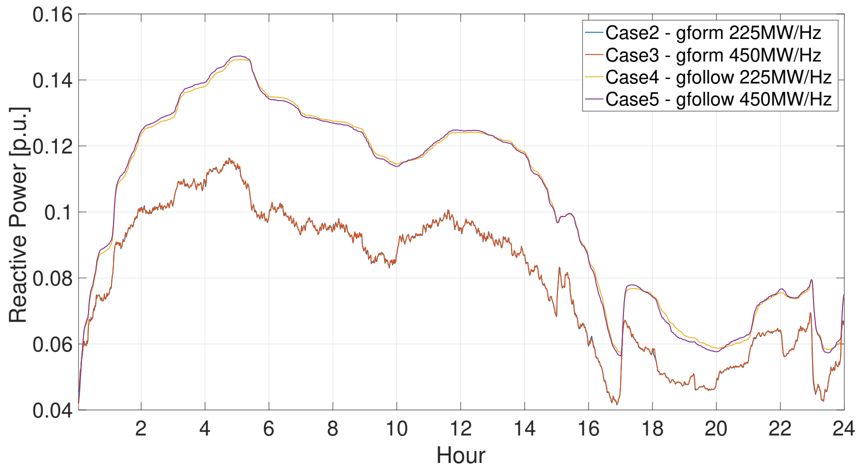

Figure 4.11 – BESS reactive power.

apparent power over the 24 hours of the simulation.

On one hand, the PDF of the grid frequency (therefore the active power of BESS) is more dependent on the droop setting. By comparing Case 3 vs Case 2 or Case 5 vs Case 4, it can be observed that the cases with the high control gain of 450MW/Hz correspond to higher apparent power due to converter's higher active power output than in the cases with the low control gain of 225MW/Hz. Therefore, for the same control law, a larger SOC decrease is exhibited in the case with higher control gain.

On the other hand, the grid-following unit exhibits a higher apparent power throughput than in the case of grid-forming unit due to the converter's higher reactive power output (see in Figure 4.11). The grid-following converter provides higher reactive power because of its voltage-reactive power (v-q) regulator, which supports the grid voltage by injecting reactive power as the grid-voltage varies. Conversely, the grid-forming unit adjusts the converter's voltage magnitude to limit the reactive power deviation from its reference value, therefore reducing the impact of grid voltage variation on the reactive power exchange.

4.7 Conclusions

In this chapter, the full-replica dynamic model of the low-inertia 39-bus power grid has been used to assess the performance of grid-forming and grid-following converter-interfaced BESS in enhancing frequency containment regulation. In order to reproduce a real operational scenario, frequency containment and restoration reserves are allocated with the same margins and procedures adopted by TSOs nowadays. To this end, a SCUC problem embedding prediction intervals from real forecasters of wind generation and electric demand is formulated. Based on the SCUC schedule, the 24-hour long dynamic simulations are executed with the real stochastic wind generation and demand profiles (both come from high-resolution measurements). In the simulations, the performance of 5 cases are compared: no BESS, BESS characterized by grid-forming converter small (225 MW/Hz) and large (445 MW/Hz) $f-p$ gains, and BESS with grid-following converter with same gains.

By means of suitably-defined frequency metrics, the results quantitatively verified that the grid-forming control outperforms the grid-following one achieving better frequency containment and lower relative RoCoF. Simulations also quantitatively demonstrate that large-scale BESSs are capable of significantly improving the system frequency containment, and the level of improvement is proportionally related to the level of $f-p$ gain.

5 OPF-driven Under Frequency Load Shedding in Low-inertia Power Grids Hosting Large-scale BESS

Large frequency excursions are more likely to happen in low-inertia grids due to reduced levels of stored kinetic energy. This calls for faster and adaptive under frequency load shedding (UFLS) protection schemes to secure the system in case of contingencies. The distributed and synchronized sensing technology provided by phasor measurement units (PMUs) enables the development of adaptive UFLS schemes. By considering Optimal Power Flow (OPF) equations, it is possible to formulate an optimization problem to restore the nominal frequency, maintaining nodal voltages and branch currents within the safety limits. In this respect, this chapter describes the formulation and application of an OPF-driven UFLS scheme to low-inertia power grids hosting large-scale battery energy storage systems (BESSs). Thanks to the accurate prediction of the system dynamics subsequent to a large contingency, the proposed OPF-UFLS is capable of minimizing the amount of load to be shed while ensuring a safe trajectory of the system frequency and preventing nodal voltages and branch currents from violating their feasible limits. The performance of the method is assessed by using numerical simulations of the fully-modeled IEEE 39-bus low-inertia power grids, where the obtained results are compared with those of the UFLS strategy recommended by the European Network of Transmission System Operators (ENTSO-E). Furthermore, the potential benefit of large-scale BESSs on the power grid response when coupled with the proposed OPF-driven UFLS method is investigated and quantified in the low-inertia 39-bus power grid.

This Chapter includes results of publications [120, 121].

5.1 Introduction

Traditionally, under frequency load shedding (UFLS) plans rely on local control strategies that implement a pre-defined decision function (e.g., frequency thresholds vs the amount of shed loads) [68]. However, in view of events characterized by anomalous power systems dynamics associated to the increasing numbers of inverter-based resources and the consequent reduction of online synchronous generation, nowadays power systems may require adaptive UFLS protection schemes [36]. Events described in [122, 65, 66] indicate that faster UFLS schemes are necessary since large frequency excursions are more likely to occur due to the decreasing kinetic energy storage in modern power grids. Furthermore, these events clearly document the presence of line tripping associated to the violation of line ampacity limits subsequent to contingencies and the load shedding actions.

In this context, the distributed and synchronised sensing technology of synchrophasors provided by phasor measurement units (PMUs) enables the development of adaptive UFLS schemes. Indeed, PMU-based distributed measurement infrastructures may compose the backbone of more sophisticated and adaptive UFLS schemes [72, 121]. In [121], the proposed approach anticipates the evolution of the frequency trajectory by means of a dynamic system model. Moreover, the proposed method is augmented by the coupling with the Optimal Power Flow (OPF) problem allowing to constrain asymptotic values of nodal voltages and branch currents.

In this Chapter, the OPF-driven UFLS method proposed in [121] is further extended and benchmarked on two configurations of the IEEE 39-bus low-inertia power grids: without (Config. II) and with (Config. III) a large-scale battery energy storage system (BESS). Indeed, the existence of large-scale BESSs in transmission systems is no longer a future scenario [18, 123] and their impact on the load shedding actions determined by UFLS strategies is still to be quantified via accurate models.

The objectives of this Chapter are listed below.

1. Propose the use of an accurate power system dynamic model that enables the OPF-driven UFLS scheme to better predict the post-contingency frequency.

2. Apply the OPF-driven UFLS scheme to low-inertia power grids with high shares of renewable energy resources (i.e., wind generation).

3. Quantify the potential benefit of large-scale BESSs on the power grid response when coupled with UFLS schemes.

4. Compare the performance of the proposed UFLS scheme with the one recommended by the European Network of Transmission System Operators (ENTSO-E).

The Chapter is structured as follows. Section 5.2 describes the OPF-driven UFLS method considering the presence of BESSs. Section 5.3.2 introduces the test-bed and study cases, then Section 5.4 illustrates and discusses the simulation results. Finally, Section 5.5 concludes this Chapter providing a summary of the findings along with recommendation on the use of UFLS schemes.

5.2 OPF-driven UFLS Method

The proposed OPF-driven UFLS method is intended to enhance the performance of the emergency operational practices in Transmission System Operator (TSO) control rooms, which, as known, are continuously running transient stability assessments. Within this context, it is reasonable to assume that the network model, comprising network topology and electrical parameters of the network components, is assessed/available in real-time in the TSO control room. On one hand, the information of network topology can be constructed by collecting the breaker/switch statues that are streamed by PMUs [124]. On the other hand, the parameters of the network components are usually known by the TSO. Based on the network model and the PMU-fed synchrophasors, the system state can be estimated in real-time with delays in the order of 100 ms [125]. In this respect, the results of the state estimation process are used by the OPF-driven UFLS method that runs in parallel with conventional contingency analysis to pre-define optimal load shedding strategy for each possible contingencies. By leveraging this real-time situational awareness system, the proposed OPF-driven UFLS method, as a centralized approach, can be easily coupled with other emergency control and management actions. It is worth to point out that the proposed method could also rely on conventional measurements provided by remote terminal units (RTU) in substations, as long as a reliable and accurate estimation of the system state is available in real-time.

Working Hypotheses: in view of the above, the proposed OPF-driven UFLS method relies on the following working hypotheses.

1. The nodal admittance matrix $\overline{Y}$, network topology and associated parameters are known in real-time.

2. The system state is tracked in real-time by means of PMUs/RTUs feeding a suitable state estimation process, guaranteeing the full observability of the system state [126].

3. Scenarios of generators' tripping are assumed to be continuously evaluated in the TSO control room.

4. The controlled variables are the system average frequency f, the magnitudes of the nodal voltage phasors $|\overline{V}_i|$ and branch current phasors $|\overline{I}_{ij}|$ (subscripts i and j are respectively the i-th and j-th node of the power grid that has N nodes and M branches). The control variables are the loads to be shed in terms of active power variation $\Delta P_{l,LS}$ in each load bus l.

5. The renewable generations (i.e., wind and photovoltaic power plants) are assumed to not contribute to the frequency regulation.

Problem Formulation: the amount of loads to be shed is determined by the following optimization problem whose constraints are discussed in detail in the following sub-sections.

$$\min_{\Delta P_{l,LS}} \sum_{l=1}^{L} \Delta P_{l,LS} \tag{5.1}$$

subject to:

$$\begin{cases} f_{min}^{t\in[t_1,t_2]} \leq f(t) \leq f_{max}^{t\in[t_1,t_2]} & \forall t \in [t_1, t_2] \\ f_{min}^{t\to\infty} \leq f(t) \leq f_{max}^{t\to\infty} & t \to \infty \end{cases} \tag{5.2}$$

$$V_{i,min} \leq V_i \leq V_{i,max} \quad \forall i = 1, ..., N \tag{5.3}$$

$$I_{ij} \leq I_{ij,max} \quad \forall ij = 1, ..., M \tag{5.4}$$

$$\begin{aligned} &\tfrac{d\Delta f(t)}{dt} = \tfrac{f_n}{2H}\Big(\Delta P_{PFR}(t) - P_{LoG} + \\ &\sum \Delta P_{l,LS} - (D_s + D_{BESS})\Delta f(t)\Big) \end{aligned} \tag{5.5}$$

$$\begin{aligned} &k_1 \tfrac{d^2\Delta P_{PFR}(t)}{dt^2} + k_2 \tfrac{d\Delta P_{PFR}(t)}{dt} + k_3 \Delta P_{PFR}(t) \\ &= -\tfrac{1}{R_{eq}}\Big(k_4 \tfrac{d^2\Delta f(t)}{dt^2} + k_5 \tfrac{\Delta f(t)}{dt} - \Delta f(t)\Big) \end{aligned} \tag{5.6}$$

$$\Delta P_g = \begin{cases} -\tfrac{1}{R_g}\Delta f & \text{if } -\tfrac{1}{R_g}\Delta f \leq \Delta P_{g,max} \\ \Delta P_{g,max} & \text{if } -\tfrac{1}{R_g}\Delta f > \Delta P_{g,max} \end{cases} \tag{5.7}$$

$$\Delta Q_g = \begin{cases} \beta \Delta P_g & \text{if } V_g > \tfrac{Q_g - \beta P_g}{Q_{P=0}} \\ \tfrac{Q_{g,n}}{P_{g,n}} \Delta P_g & \text{if } V_g \leq \tfrac{Q_g - \beta P_g}{Q_{P=0}} \end{cases} \tag{5.8}$$

$$\Delta P_l = \Delta P_{l,LS} + \frac{P_{l,n} k_{pv}}{V_n} \Delta V_l + P_{l,n} k_{pf} \Delta f \tag{5.9}$$

$$0 \leq \Delta P_{l,far,LS} \leq 0.5\ |P_{l,far,n}| \tag{5.10}$$

$$0 \leq \Delta P_{l,adj,LS} \leq |P_{l,adj,n}| \tag{5.11}$$

$$\Delta Q_l = \Delta Q_{l,LS} + \frac{Q_{l,n} k_{qv}}{V_n} \Delta V_l + Q_{l,n} k_{qf} \Delta f \tag{5.12}$$

$$\Delta Q_{l,LS} = \Delta P_{l,LS} \frac{Q_{l,n}}{P_{l,n}} \tag{5.13}$$

$$|\Delta \overline{V}_i| \cong \frac{\partial |\overline{V}_i|}{\partial P_k} \Delta P_k + \frac{\partial |\overline{V}_i|}{\partial Q_k} \Delta Q_k \tag{5.14}$$

$$|\Delta \overline{I}_{ij}| \cong \frac{\partial |\overline{I}_{ij}|}{\partial P_k} \Delta P_k + \frac{\partial |\overline{I}_{ij}|}{\partial Q_k} \Delta Q_k \tag{5.15}$$

The meaning of the symbols is listed here below.

List of Symbols

f system frequency

$\overline{V}_i, \underline{V}_i, V_i$ voltage at bus i: complex phasor, conjugate phasor and phasor module

$\overline{I}_{ij}, \underline{I}_{ij}, I_{ij}$ line current from bus i to j: complex phasor, conjugate phasor and phasor module

P_g, Q_g active and reactive power of generator g

P_l, Q_l active and reactive power of load l

P_{PFR} primary frequency regulator power

P_{LoG} loss of generation power

H system equivalent inertia

D system damping coefficient

D_{BESS} additional damping coefficient introduced by the BESS

R_g governor droop coefficient of generator g

k_1, k_2, k_3, k_4, k_5 system frquency regulation coeffcients

S_g base power of generator g

S_b base power of the entire system

β excitation system characteristic's slope

k_{pv}, k_{pf} active power coefficients in load model: voltage exponent and frequency sensitivity

k_{qv}, k_{qf} reactive power coefficients in load model: voltage exponent and frequency sensitivity

t_1 time instant when the contingency occurs

t_2 time instant when the post-contingency dynamic is exhausted

n subscript associated to nominal value

LS subscript associated to load shedding action

min, max subscripts associated to minimum and maximum safety values

N, L, G total number of buses, loads and generators

i, j, k bus indexes defined in the set $[1, \dots N]$

l load index defined in the set $[1, \dots L]$

g generator index defined in the set $[1, \dots G]$

5.2.1 Grid Constraints

The grid constraints enforce frequency, nodal voltage and branch currents limits, as shown in the equations below:

$$\begin{cases} f_{min}^{t\in[t_1,t_2]} \leq f(t) \leq f_{max}^{t\in[t_1,t_2]} & \forall t \in [t_1, t_2] \\ f_{min}^{t\to\infty} \leq f(t) \leq f_{max}^{t\to\infty} & t \to \infty \end{cases} \tag{5.2}$$

$$V_{i,min} \leq V_i \leq V_{i,max} \quad \forall i = 1,...N \tag{5.3}$$

$$I_{ij} \leq I_{m,max} \quad \forall ij = 1,...M \tag{5.4}$$

During the early post-contingency transients, i.e., from t_1 to t_2, the frequency is constrained within 49 and 51 Hz, which is corresponding to the maximum instantaneous frequency deviation range indicated in [127]. As for the asymptotic value of the post-contingency steady-state frequency, the indicated range is [49.8, 50.2] according to the technical study on UFLS plan for Continental Europe in presence of renewable energy resources [128]. The safety constraints of the nodal voltage are set to ±5% of the rated voltage [104], and the limits on the branch currents are set as the maximum capacity of each transmission line.

It is worth to note that only frequency dynamics are tracked in time-domain. For the other system variables, i.e., nodal voltages, branch currents, active and reactive power, their post-contingency asymptotic values are constrained. With respect to the grid constraints on frequency, the OPF-driven UFLS control aims at predicting the frequency trajectory over a pre-defined time horizon, preventing it to drop below 49 Hz during the transient, and ensuring the post-contingency value to be within 50 Hz ± 0.2 Hz. Regarding voltage magnitude limits and current ampacities, the OPF-driven UFLS predicts the post-contingency values of the voltages and currents, determining the optimal amounts and locations of loads to be shed to keep the system from violating the corresponding operating limits.

5.2.2 System Frequency Response

A third-order equivalent frequency dynamic response model is proposed to predict the frequency trajectory subsequent to the power imbalance and load shedding. The system frequency response is modeled through an equivalent swing equation, accounting for the loss of generation, the load shedding, and the frequency regulation provided by the synchronous generators and the BESS.

Equivalent swing equation

As it is assumed that all generators swing synchronously at a common frequency f, the system frequency response is represented through an equivalent single-machine swing equa-

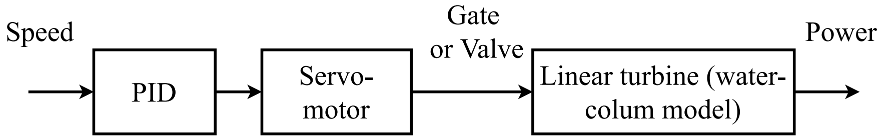

Figure 5.1 – Block diagram of hydro turbine-governing system.

tion (where we make reference to quantities in per-unit) [129]:

$$\frac{d\Delta f(t)}{dt} = \frac{f_n}{2H}\left(\Delta P_{PFR}(t) - P_{LoG} + \sum \Delta P_{l,LS} - (D_s + D_{BESS})\Delta f(t)\right) \tag{5.5}$$

where Δf is the frequency deviation from the nominal frequency f_n, H is the equivalent inertia constant of the grid, P_{LoG} is the loss of generation, $\Delta P_{PFR}(t)$ is the power variation as a result of synchronous generators primary frequency regulation, $\sum \Delta P_{l,LS}$ is the total load shedding, D_s is the system damping coefficient, and D_{BESS} is the damping coefficient due to battery frequency regulation. In order to account for the influence of load shedding on system damping effect, D_s is calibrated by the function:

$$D_s = D_{s,0} + \alpha \frac{\sum \Delta P_{l,LS}}{P_{LoG}} \tag{5.16}$$

where $D_{s,0}$ is the system damping coefficient when no UFLS plan is employed, α is hereby defined as damping-shedding coefficient. It is worth to note that the calibration of the system damping coefficient is to account for the influence of voltage[1] on the nodal power flow during the transient subsequent to the load shedding.

Primary frequency regulation by synchronous generators

The low-inertia power grid envisaged in this work is dominated by hydro and wind power plants. In this study, the hydro generators are committed to delivering the primary frequency regulation, whereas the wind generators are considered not providing frequency regulation services. As shown in Figure 5.1, the hydroelectric unit can be represented by a third-order transfer function, which considers the governor and the hydraulic turbine [118].

It is generally acknowledged that the servomotor time constant is significantly smaller than the water time constant of the hydraulic turbine and the PID controller time constant [92, 95]. Therefore, to reduce the computational complexity, the primary frequency regulation of hydro units is modelled by an equivalent second-order transfer function represented by the following

[1]The voltages affect the nodal power flow on two aspects: first, the load power is not only frequency-dependent but also voltage-dependent (see Section 5.2.4); second, the losses on transmission lines are also influenced by nodal voltages.

differential equation:

$$k_1 \frac{d^2 \Delta P_{PFR}(t)}{dt^2} + k_2 \frac{d\Delta P_{PFR}(t)}{dt} + k_3 \Delta P_{PFR}(t) = -\frac{1}{R_{eq}}\left(k_4 \frac{d^2 \Delta f(t)}{dt^2} + k_5 \frac{\Delta f(t)}{dt} - \Delta f(t)\right) \quad (5.6)$$

where, k_1, k_2, k_3, k_4 and k_5 are system frequency regulation coefficients (to be identified [130]), and R_{eq} is equivalent governor droop derived from individual generator's droops R_g:

$$\frac{1}{R_{eq}} = \sum_{g=1}^{G} \frac{S_g}{S_b R_g} \quad (5.17)$$

where S_g is the base power of generator g and S_b is system power base.

Frequency regulation by grid-forming converter-based BESS

We consider the presence of large-scale BESS interfaced with the low-inertia power grid through a grid-forming converter. The implemented converter control is the PLL-free grid-forming control with coupled functionalities, described in Chapter 3, Section 3.3.1. It creates a direct link between the voltage angle and the output active power of the converter, enabling the converter to synchronize with the grid and deliver in primary frequency regulation:

$$\Delta P_{BESS} = k_{BESS} \Delta f \quad (5.18)$$

where ΔP_{BESS} is the active power variation of BESS and k_{BESS} is the power-frequency control gain set in the BESS grid-forming controller of its power electronic interface.

Accordingly, the primary frequency regulation provided by the BESS is equivalent to an additional damping coefficient in (5.5), given by the following equation:

$$D_{BESS} = k_{BESS} / S_b \quad (5.19)$$

5.2.3 Generators

As regards the generators, their active power is determined based on the generator's droop characteristic:

$$\Delta P_g = \begin{cases} -\frac{1}{R_g}\Delta f & \text{if } -\frac{1}{R_g}\Delta f \leq \Delta P_{g,max} \\ \Delta P_{g,max} & \text{if } -\frac{1}{R_g}\Delta f > \Delta P_{g,max} \end{cases} \quad (5.7)$$

In particular, as long as the computed active power deviation ΔP_g is lower than the maximum attainable power output, the droop characteristic is considered. Otherwise, the power is set to the generator's maximum set-point. The reactive power, instead, is computed as a function of

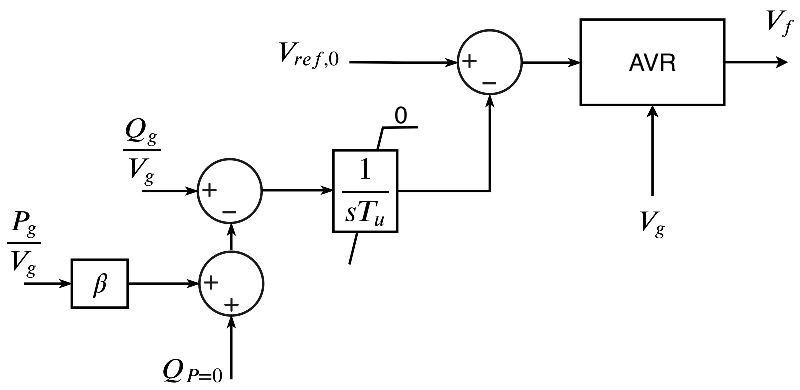

Figure 5.2 – Diagram of the excitation system accounting for active and reactive power: $V_{ref,0}$ is the generator nominal voltage, T_u the under-excitation time constant, V_f the excitation voltage.

the active power, scaled to a voltage-dependent factor:

$$\Delta Q_g = \begin{cases} \beta \Delta P_g & \text{if } V_g > \frac{Q_g - \beta P_g}{Q_{P=0}} \\ \frac{Q_{g,n}}{P_{g,n}} \Delta P_g & \text{if } V_g \leq \frac{Q_g - \beta P_g}{Q_{P=0}} \end{cases} \tag{5.8}$$

where $Q_{P=0}$ is the reactive power absorbed by the generator in case of null supplied active power and β is the inverse of the under-excitation characteristic's slope. In particular, the synchronous generators embed the excitation system presented in Figure 5.2. Based on such scheme, and as presented in (5.8), the reactive power deviation ΔQ_g depends on the voltage at the generator's output V_g. Specifically, in case V_g exceeds a specific threshold, ΔQ_g is proportional to ΔP_g with the coefficient of β. For V_g below the threshold, ΔQ_g is proportional to ΔP_g with the coefficient of $\frac{P_{g,n}}{Q_{g,n}}$, where $P_{g,n}$ and $Q_{g,n}$ are the generator's pre-contingency active power and reactive power, respectively.

5.2.4 Loads

The load model relies on the Electric Power Research Institute (EPRI) LOADSYN model [100], that is adaptable to different systems and conditions [131]. In particular, the loads are modeled as follows:

$$P_l = (P_{l,n} + \Delta P_{l,LS}) \left(\frac{V_l}{V_n} \right)^{k_{pv}} \left(1 + k_{pf}(f_l - f_n) \right) \tag{5.20}$$

$$Q_l = (Q_{l,n} + \Delta Q_{l,LS}) \left(\frac{V_l}{V_n} \right)^{k_{qv}} \left(1 + k_{qf}(f_l - f_n) \right) \tag{5.21}$$

where $P_{l,n}$ and $Q_{l,n}$ represent the power consumed at the rated voltage and system frequency and $\Delta P_{l,LS}$ and $\Delta Q_{l,LS}$ are the amount of shed power at load l. The values of the load voltage- and frequency- dependent coefficients (i.e., $k_{pv}, k_{pf}, k_{qv}, k_{qf}$), that represent a comprehensive set of empirically determined parameters for various load classes [100], are provided in Appendix A.2.

In order to have a convex formulation, (5.20) and (5.21) are linearized around the pre-contingency active and reactive power set-points:

$$\Delta P_l = \Delta P_{l,LS} + \frac{P_{l,n} k_{pv}}{V_n} \Delta V_l + P_{l,n} k_{pf} \Delta f \tag{5.9}$$

$$\Delta Q_l = \Delta Q_{l,LS} + \frac{Q_{l,n} k_{qv}}{V_n} \Delta V_l + Q_{l,n} k_{qf} \Delta f \tag{5.12}$$

To estimate the shed reactive power, we assume that the power factor of the loads remains constant, i.e., the ratio between reactive and active power is assumed to remain constant:

$$\Delta Q_{l,LS} = \Delta P_{l,LS} \frac{Q_{l,n}}{P_{l,n}} \tag{5.22}$$

Constraint (5.10) is introduced to adhere to conventional UFLS methods (e.g., [128]) where the amount of load shedding is limited to 50 % of the rated load power. However, this constraint is applied to the load nodes that are not adjacent to the one where the contingency is taking place. The nodes that are adjacent to the one experiencing the contingency, are allowed to shed the total amount of their load. This relaxed constraint, i.e. (5.11), increases the solution space of the OPF that usually experiences binding constraints corresponding to those of nodes and lines surrounding the location where the contingency happens.

5.2.5 Nodal Voltages and Branch Currents

The proposed OPF-driven UFLS method determines the nodal voltages $\overline{V}_i$ and branch currents $\overline{I}_{ij}$ as a linearized function of the nodal power injections, leveraging on the direct computation of state-dependent sensitivity coefficients proposed in [132].

As proposed in [132], in order to derive the voltage sensitivity coefficients, the partial derivatives of voltage $\overline{V}_i$ with respect to the active and reactive power P_k and Q_k of a bus $k \in [1,...,N]$ (i.e., $\frac{\partial \underline{V}_i}{\partial P_k}, \frac{\partial \overline{V}_j}{\partial P_k}, \frac{\partial \underline{V}_i}{\partial Q_k}$ and $\frac{\partial \overline{V}_j}{\partial Q_k}$) need to be computed via the following system of equations:

$$\mathbb{1}_{\{i=k\}} = \frac{\partial \underline{V}_i}{\partial P_k} \sum_{j=1}^{N} \overline{Y}_{ij} \overline{V}_j + \underline{V}_i \sum_{j=1}^{N} \overline{Y}_{ij} \frac{\partial \overline{V}_j}{\partial P_k} \tag{5.23}$$

$$-\mathbb{1}_{\{i=k\}} = \frac{\partial \underline{V}_i}{\partial Q_k} \sum_{j=1}^{N} \overline{Y}_{ij} \overline{V}_j + \underline{V}_i \sum_{j=1}^{N} \overline{Y}_{ij} \frac{\partial \overline{V}_j}{\partial Q_k} \tag{5.24}$$

where $\overline{Y}_{ij}$ is the generic element of system nodal admittance matrix $\overline{Y}$ between node i and node j, $\overline{V_i}$ and $\underline{V_i}$ are complex phasor and conjugate phasor of the voltage at bus i, respectively. As it is assumed that the system operator knows in real-time the model and states of the system, in the power flow equations (5.23) and (5.24), the nodal admittance matrix and the voltage phasors are known. Therefore, the only unknowns are these sensitivity coefficients, namely, the partial derivatives of the voltage phasors with respect to each bus's active and reactive power injections. In [132], it has been proved that the solution of the sensitivity coefficients is unique, if and only if the load flow solution is unique for the current system state. In this context, the sensitivity coefficients are also working for meshed transmission systems, provided that the load flow has a unique solution in the current operating point.

It is worth pointing out that, although the systems of (5.23) and (5.24) are not linear over complex numbers, they are linear with respect to $\frac{\partial \underline{V}_i}{\partial P_k}, \frac{\partial \overline{V}_j}{\partial P_k}$ and $\frac{\partial \underline{V}_i}{\partial Q_k}, \frac{\partial \overline{V}_j}{\partial Q_k}$, respectively. Therefore, they are linear over real numbers with respect to rectangular coordinates.

Once $\frac{\partial \underline{V}_i}{\partial P_k}, \frac{\partial \overline{V}_j}{\partial P_k}$ and $\frac{\partial \underline{V}_i}{\partial Q_k}, \frac{\partial \overline{V}_j}{\partial Q_k}$ are obtained, the partial derivatives of the magnitude of the voltage at bus i with respect to active and reactive power at bus k are defined as:

$$\frac{\partial |\overline{V}_i|}{\partial P_k} = \frac{1}{|\overline{V}_i|} \mathrm{Re}\left\{ \underline{V}_i \frac{\partial \overline{V}_i}{\partial P_k} \right\} \tag{5.25}$$

$$\frac{\partial |\overline{V}_i|}{\partial Q_k} = \frac{1}{|\overline{V}_i|} \mathrm{Re}\left\{ \underline{V}_i \frac{\partial \overline{V}_i}{\partial Q_k} \right\} \tag{5.26}$$

Based on these sensitivity coefficients, it is possible to approximate voltage variations as linearized functions of active and reactive power at bus k :

$$|\Delta \overline{V}_i| \cong \frac{\partial |\overline{V}_i|}{\partial P_k} \Delta P_k + \frac{\partial |\overline{V}_i|}{\partial Q_k} \Delta Q_k \tag{5.14}$$

As the sensitivity coefficients linking the power injections to the voltage variations are known, it is straightforward to express the branch current sensitivities with respect to the same power injections. The current flow $\overline{I}_{ij}$ between node i and j can be expressed as the function of the voltages of the relevant i, j voltage:

$$\overline{I}_{ij} = \overline{Y}_{ij} \left(\overline{V}_i - \overline{V}_j \right) \tag{5.27}$$

Then the partial derivatives of the current with respect to the active and reactive power injections in the network can be expressed as:

$$\frac{\partial \overline{I}_{ij}}{\partial P_k} = \overline{Y}_{ij} \left(\frac{\partial \overline{V}_i}{\partial P_k} - \frac{\partial \overline{V}_j}{\partial P_k} \right) \tag{5.28}$$

$$\frac{\partial \overline{I}_{ij}}{\partial Q_k} = \overline{Y}_{ij} \left(\frac{\partial \overline{V}_i}{\partial Q_k} - \frac{\partial \overline{V}_j}{\partial Q_k} \right) \tag{5.29}$$

where the partial derivative of voltages with respect to the active and reactive power have been obtained via (5.23) and (5.24).

The variation of the currents magnitude could be estimated in a similar way as (5.14). However, due to the approximation introduced by the above linearizations, there might be cases where $\Delta I_{ij} < -|\bar{I}_{ij,0}|$ (with $\bar{I}_{ij,0}$ being the pre-contingency current in line ij) yielding a negative magnitude. For this reason, the magnitude of the current is computed based on its real and imaginary components:

$$\Delta\bar{I}_{ij} \cong \frac{\partial\bar{I}_{ij}}{\partial P_k}\Delta P_k + \frac{\partial\bar{I}_{ij}}{\partial Q_k}\Delta Q_k \tag{5.15}$$

$$|\bar{I}_{ij}| = \sqrt{\mathrm{Re}\left\{\bar{I}_{ij,0} + \Delta\bar{I}_{ij}\right\}^2 + \mathrm{Im}\left\{\bar{I}_{ij,0} + \Delta\bar{I}_{ij}\right\}^2} \tag{5.30}$$

When coupled with (5.4), constraint (5.30) becomes a nonlinear but convex equality constraint. To achieve a linear formulation, the ampacity circle constraint given by (5.4) and (5.30) has been piece-wise linearized, obtaining a set of linear constraints.

5.2.6 Iterative Solution

Applying (5.16) in (5.5) causes the constraints constructed based on (5.5) to be nonlinear. In this respect, the formulated problem is solved in an iterative fashion as illustrated in Figure 5.3. In each iteration, the system damping coefficient is set as constant, such that the optimization problem to be solved is linear. The initial damping coefficient is set as $D_{s,0}$, i.e., the damping coefficient when no load shedding is employed. Then, the updated damping coefficient is computed according to (5.16), using the obtained load shedding results. The iteration process stops as the difference between the two consecutive damping coefficients is equal or smaller than the error tolerance ϵ[2].

5.2.7 Computational complexity

Theoretically, the formulated problem could be solved at every time step to have very accurate predictions of all the controlled (i.e., system frequency, voltage, and current phasors) with respect to the control (i.e., power injections) variables for the entire time-horizon. The computational complexity associated with solving problem (5.2) - (5.15) at every time step is pretty high, even though all the constraints have been properly linearized. In particular, the piecewise linearization of the load models in (5.9) and (5.12) involves three decision variables (amount of load shedding power, frequency, and voltage magnitude). This leads to many constraints, resulting in an intractable complex optimization problem. Also, as expressed in (5.23) and (5.24), the computation of the sensitivity coefficients requires solving a linear system of equations where the matrix to be inverted changes over time based on the decision variables of the previous time-step.

In order to reduce the computational complexity of the proposed problem, only the trajectory

[2]The tolerance ϵ is smaller than 0.1% of the magnitude of the damping coefficient.

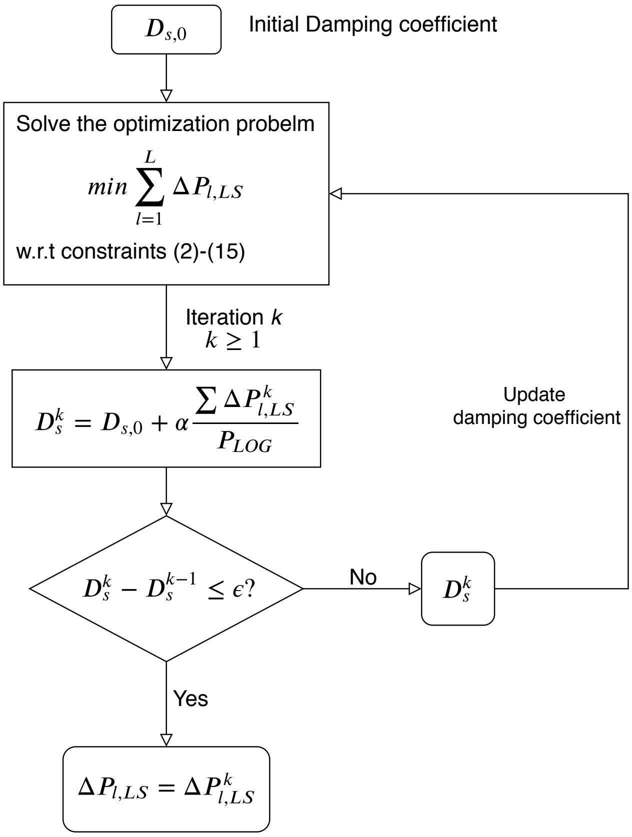

Figure 5.3 – Iterative method to solve the optimization problem formulated for the OPF-driven UFLS strategy.

of the frequency is predicted and constrained over the entire time-horizon, via (5.5) and (5.6). Regarding the other variables, i.e., the nodal voltages, the branch currents, and the active and reactive power profiles (for both generation and load buses), only their asymptotic values are computed:

$$\Delta V_i(t), \Delta I_{ij}(t), \Delta P_i(t), \Delta Q_i(t) \qquad \text{only for } t \to \infty \tag{5.31}$$

$$f(t) \qquad \forall t \tag{5.32}$$

Nevertheless, it should be noticed that the proposed method is scalable, since each synchronous generator can be regarded as the dynamic equivalent model of a synchronous area that could be characterized by a specific system frequency response model.

5.3 Test-bed and Study Cases

5.3.1 Low-inertia 39-bus Power Grids

The OPF-driven UFLS method is tested on the low-inertia IEEE 39-bus power grids proposed in Chpater 3, Section 3.2. Its performance is assessed through simulations of the full-replica dynamic models executed on a Opal-RT eMEGAsim real-time simulator. It is worth noting that the adoption of a RTS is only to decrease the computation time needed to determine the system response. The optimization problem is implemented via the Yalmip-MATLAB interface and executed on a MacBook Pro (3.3 GHz Core i7 processor, 16 GB RAM) with the Gurobi solver.

Figure 5.4 recalls the topologies of the low-inertia IEEE 39-bus power systems, without (Config. II) and with (Config. III) converter-based BESS, respectively. Details on the modeling of synchronous generators, wind power plants, voltage and frequency-dependent loads, and the converter-based BESS can be found in Appendix A. The model hosts in every node a simulated PMU embedding the e-IpDFT (enhanced Interpolate Discrete Fourier Transform) synchrophasor compliant with P-class of the IEEE std. c27.118 [119]. The simulated PMUs send nodal voltages and branch currents synchorophasors, as well as frequency measurements, to the UFLS controller that acts on the load to be shed based on the corresponding UFLS strategy.

5.3.2 Cases Studies

The results are compared with those obtained in case of utilizing the local UFLS control scheme (denoted as Standard UFLS) recommended by the ENTSO-E [128]. For Continental Europe in presence of renewable energy resources, [128] has conducted simulations to establish recommendations on the minimum mandatory number of load shedding steps and the amplitude range of each step. Figure 5.5 shows the Standard UFLS adopting these recommended frequency thresholds and the corresponding load shedding amount. Also, ENTSO-E recommends the total tripping time of load shedding relay (considering measuring

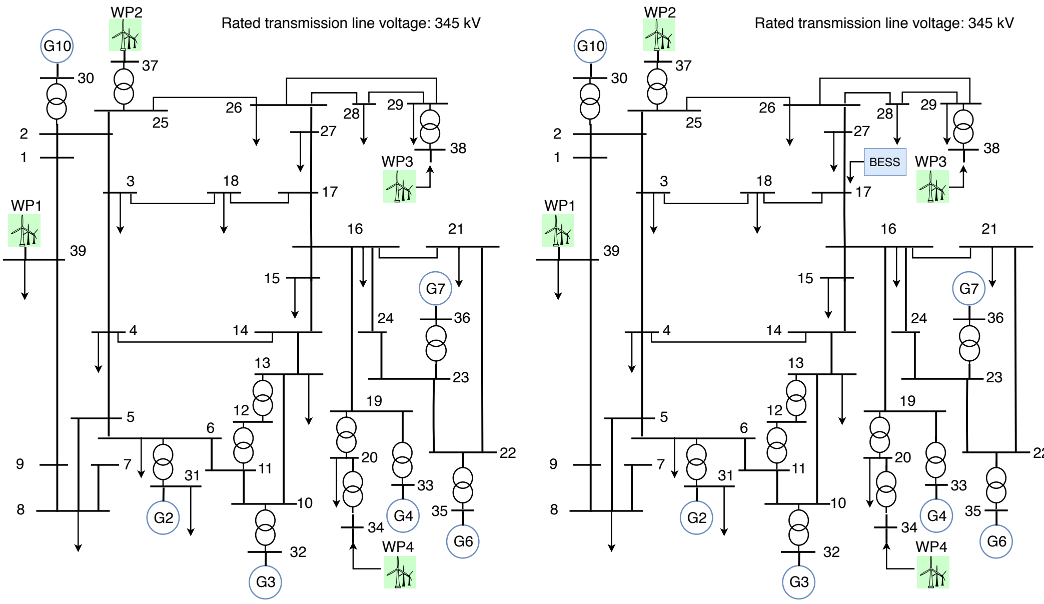

(a) Config. II (b) Config. III

Figure 5.4 – Topologies of the low-inertia 39-bus power systems.

Table 5.1 – Study cases.

	Configuration	
	Without BESS	**With BESS**
No UFLS	Config. II - case 1	Config. III - case 1
Standard UFLS	Config. II - case 2	Config. III - case 2
OPF-driven UFLS	Config. II - case 3	Config. III - case 3

time, trip action of auxiliary circuits and circuit breaker opening time) to be less than or equal to 150 ms [128]. Therefore, the considered Standard UFLS scheme and the OPF-driven UFLS scheme are both implemented with a 150 ms activation delay. It is worth noting that for the Standard UFLS, the delay time is counted after triggering one of the frequency thresholds, whereas for the OPF-driven UFLS, the delay time is counted after the control center receiving the signal indicating the occurrence of the contingency.

As illustrated in TABLE 5.1, with respect to each of the two low-inertia configurations of the IEEE 39-bus network, the results of 3 cases are assessed: No UFLS, Standard UFLS and OPF-drive UFLS. For the considered cases, dedicated simulations are conducted for the contingency of tripping generator 4, yielding 485 MW loss of generation. This contingency is selected as it would violate multiple line ampacity and node voltage limits without implementing any UFLS scheme (results for the cases that no UFLS are provided in Section 5.4). The pre-contingency nodal power injections of load and generation buses are shown in Table. 5.2.

Table 5.2 – Load and generation buses: pre-contingency nodal power injection.

Load #	1	2	3	4	5	6	7	8	9	10	11	12	13	14	15	16	17	18	19
Bus #	3	4	7	8	12	15	16	18	20	21	23	24	25	26	27	28	29	31	39
P [MW]	328	502	233	522	13	327	340	162	315	283	282	315	239	147	285	210	290	5	1067
Q [MVar]	2	85	84	76	88	79	34	31	50	60	90	-98	52	19	38	30	29	2	230

Generation Unit #	1	2	3	4	5	6	7	8	9	10
Bus #	39	31	32	33	34	35	36	37	38	30
Type	WPP [a]	SG [b]	SG	SG	WPP	SG	SG	WPP	WPP	SG
P [MW]	1148	230	536	485	520	588	535	989	746	240
Q [MVar]	139	229	156	175	55	136	35	46	15	156

[a] Wind Power Plant
[b] Synchronous Generator

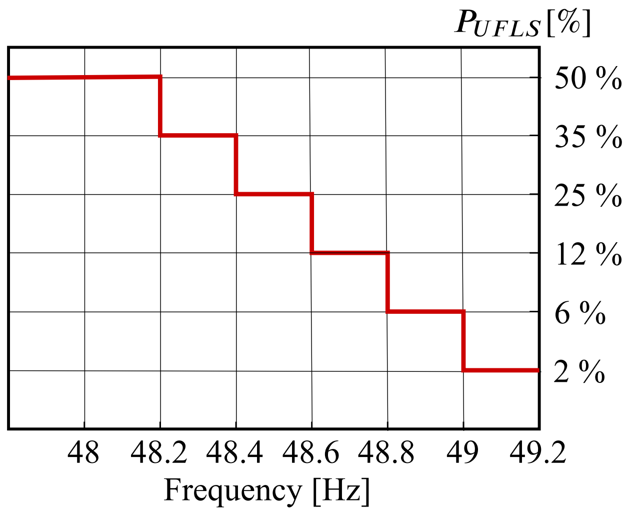

Figure 5.5 – Percentage of load to be shed as a function of the frequency as suggested by ENTSO-E. Adapted from [128].

5.4 Performance Assessment in Low-inertia 39-bus Power Grids

This Section presents the numerical assessment of the performance of the UFLS schemes implemented in the low-inertia 39-bus power grid without (Config. II) and with (Config. III) BESS. First, the analysis of dedicated contingency tests carried out with respect to the 3 cases, namely: (i) No UFLS, (ii) Standard UFLS and (iii) OPF-driven UFLS(see Section 5.4.1 and Section 5.4.2). Then, Section 5.4.3 presents the assessment of the expected energy not served in the low-inertia 39-bus power grids implementing the OPF-driven UFLS and the Standard UFLS, respectively. At last, Section 5.4.4 discusses the effect of the calibration of system damping coefficient on the load shedding action and the frequency tracking performed by the OPF-driven UFLS strategy.

5.4.1 Results for the Low-inerta 39-bus Power Grid without BESSs

In Config. II, the UFLS control strategies are implemented in the low-inertia 39-bus power grid where the BESS is not installed. The OPF-driven UFLS scheme determines to shed a total of 407.7 MW, in which load 15 sheds 95.8 MW, load 20 sheds 303.8 MW, and load 39 sheds 8.3 MW. The Standard UFLS method determines that each of the 19 loads should shed 6%, thereby with the total amount of 345 MW.

Figure 5.6 shows the frequency trajectory of the 3 cases where no UFLS, the Standard UFLS and the OPF-driven UFLS are implemented, respectively. The frequency nadir for case 1, 2 and 3 are 48.49 Hz, 48.84 Hz and 49.83 Hz, respectively. Compared with the Standard UFLS, the proposed UFLS scheme achieves a higher frequency nadir (i.e., +1.34 Hz) without experiencing frequency overshooting as happens in the case of Standard UFLS.

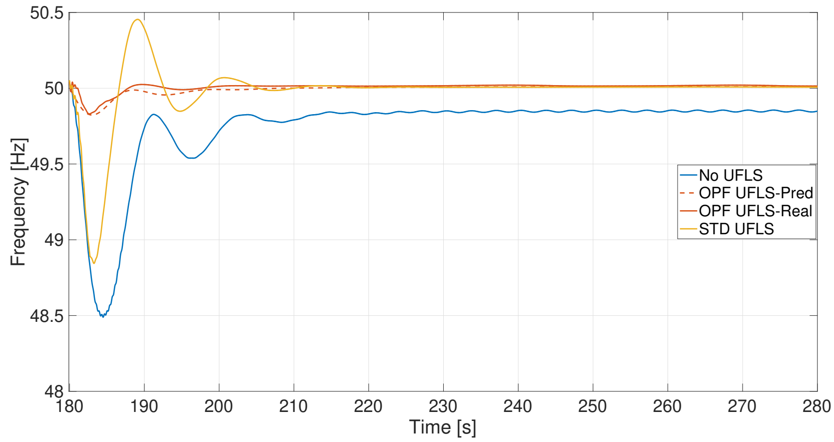

Figure 5.6 – Frequency trajectory for the 3 cases in Config. II: No UFLS (blue), Standard UFLS (yellow), OPF-driven UFLS prediction (dash red) and realization (solid red).

In Figure 5.6 - Figure 5.8, the curves referred as *Real* are obtained by simulating the detailed system response via the full dynamic model of Config. II and the curves referred as *Pred* are the predicted values using the OPF model. As shown in Figure 5.6, a good frequency tracking is achieved, being the mean prediction errors during the transient (180 $s \leq t \leq 220$ s) and the post-contingency steady state ($t \to \infty$) are 0.0224 Hz and 0.0081 Hz, respectively. Also, as shown in Figure 5.7 and Figure 5.8, all the post-contingency voltage and current states are predicted with a high fidelity by the OPF-driven UFLS.

Figure 5.8 shows the voltage limits and the post-contingency nodal voltage magnitudes and Figure 5.9 exhibits the ampacity and the post-contingency current magnitudes for lines 13-14, 22-23 and 25-26. Without UFLS, current ampacities for lines 13-14, 22-23 and 25-26, and the voltage limit for node 20, are all largely violated. Thanks to the high prediction fidelity on system states (i.e., system frequency, branch currents and nodal voltages), the proposed UFLS scheme is capable to prevent nodal voltages and branch current limits violation. On the contrary, the Standard UFLS results into a system state where the current ampacity for line 13-14 and voltage limits at node 20 are violated.

It is worth noting that the margin of improvement of the Standard UFLS by changing its load shedding parameters (i.e., the maximum frequency threshold, number of load shedding steps, percent of load shed per threshold in Figure 5.5) is minimal. Firstly, the issue of frequency overshooting observed for the Standard UFLS is caused by the fact that the load shedding action has to wait until frequency decrease below 49.2 Hz, which is the maximum frequency threshold allowed by ENTSOE [69]. The adopted Standard UFLS already uses 49.2 Hz to react as fast as possible. Secondly, the problem of voltage and current limit violations for the Standard UFLS is due to the fact that it is myopic to the system states (e.g., branch currents and nodal voltages). Therefore, tuning the load shedding steps or the percentage of load to be shed for each threshold can hardly solve the voltage and current limit violation problem.

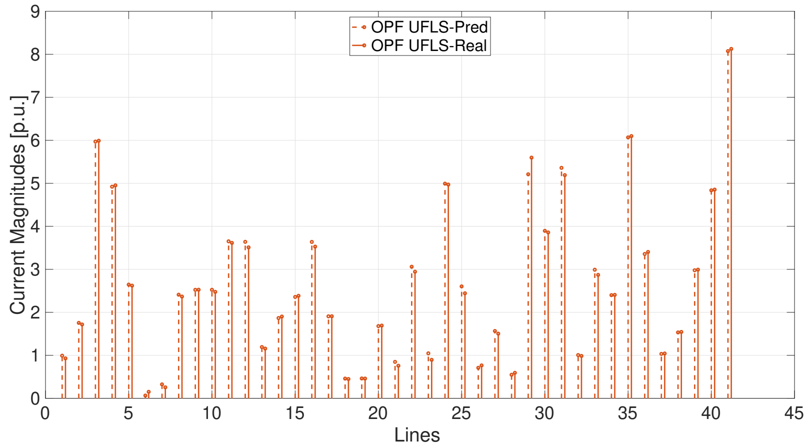

Figure 5.7 – Currents flow in all the lines for Config. II with OPF-driven UFLS: prediction (dash red) and realization (solid red).

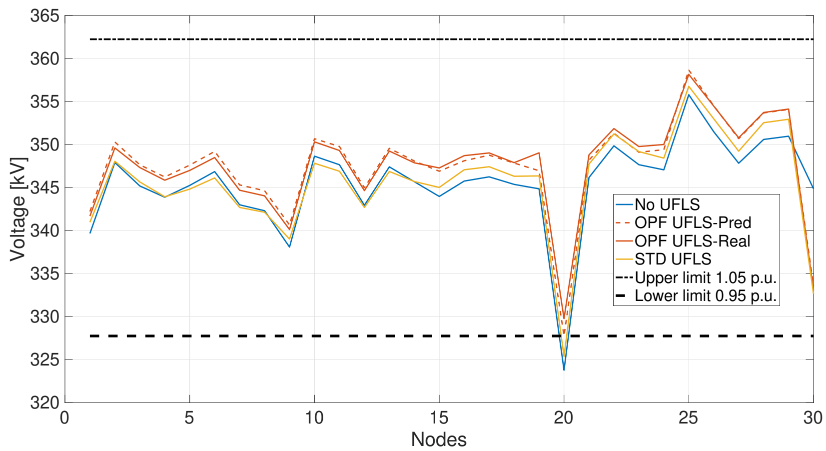

Figure 5.8 – Nodal voltages for the 3 cases in Config. II: No UFLS (blue), Standard UFLS (yellow), OPF-driven UFLS prediction (dash read) and realization (solid red). The dash and solid black lines are the upper and lower limits of the nodal voltage, respectively.

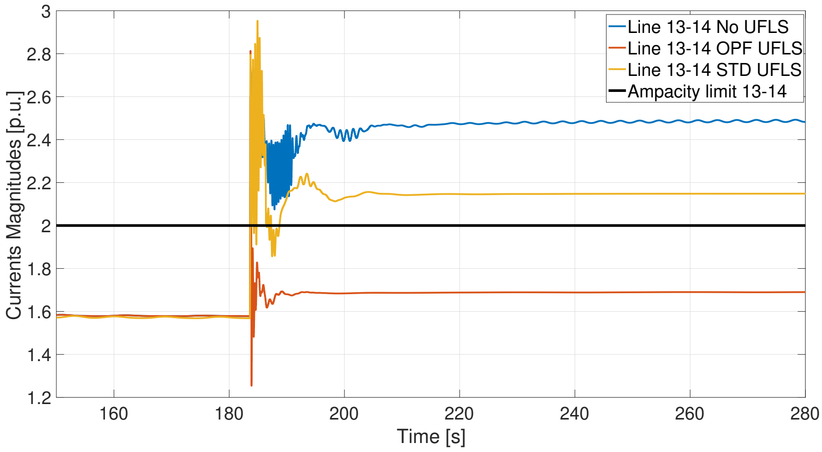

(a) Line 13-14.

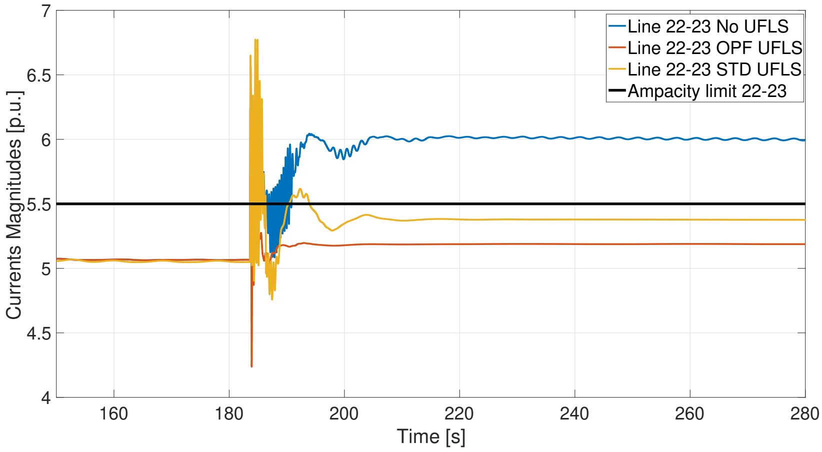

(b) Line 22-23..

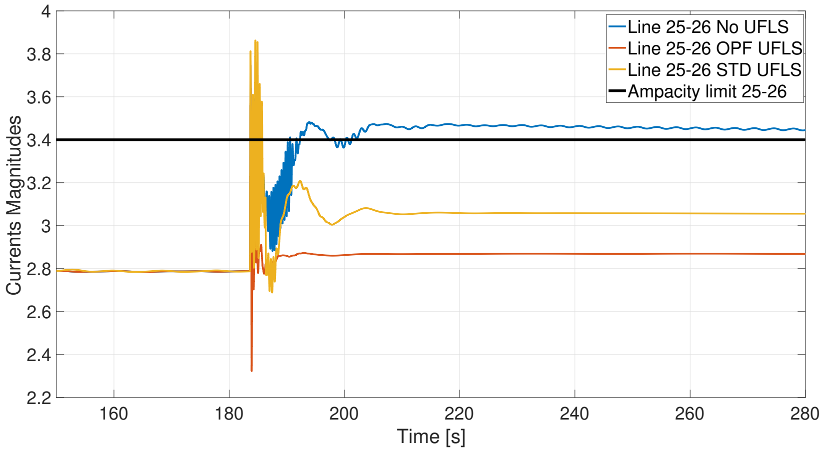

(c) Line 25-26.

Figure 5.9 – Current ampacity and line current for the 3 cases in Config. II: No UFLS (blue), Standard UFLS (yellow), OPF-driven UFLS prediction (dash red) and realization (solid red). The black lines are the ampacity of line 13-14, line 22-23 and line 25-26, respectively.

5.4.2 Results for the Low-inerta 39-bus Power Grid in the Presence of BESSs

In Config. III, a converter-based BESS is connected to the low-inertia 39-bus power grid, providing primary frequency regulation to the grid. For the studies carried out in this Chapter, the BESS converter adopts the PLL-free grid-forming control with coupled functionalities whose parameters are presented in Appendix A.5.3. As described in Section 5.2.2, in the system frequency response model, the primary frequency regulation provided by the BESS is modeled as an additional damping coefficient D_{BESS} in (5.5). 5

For this configuration, the OPF-driven UFLS scheme sheds in total 316.2 MW, where load 20 sheds 285.2 MW and load 39 sheds 31 MW. The Standard UFLS method sheds 6% at each load and the total amount is 345 MW. Figure 5.10 shows the frequency trajectory of the 3 cases where no UFLS, the Standard UFLS and the OPF-driven UFLS are implemented, respectively. The frequency nadir for case 1, 2 and 3 respectively are 48.76 Hz, 48.95 Hz and 49.61 Hz. Compare with the Standard UFLS, the proposed UFLS scheme achieves a way higher frequency nadir (i.e., +0.66 Hz) without experiencing frequency overshooting as happened in the case of the Standard UFLS.

Similarly to the previous simulation, Figure 5.10 - Figure 5.12, the curves referred as *Real* are obtained by simulating the detailed system response via the full dynamic model of Config. III, and the curves referred as *Pred* are the predicted values using the OPF model. As shown in Figure 5.10, a good frequency tracking is achieved, being the mean prediction errors during the transient (t from 180 s to 220 s) and the post-contingency steady state ($t \to \infty$) are 0.0128 Hz and 0.0011 Hz, respectively. Figure 5.11 and Figure 5.12 exhibit that all the post-contingency voltage and current states are predicted with a high fidelity by the OPF-driven UFLS.

In Config. III, the OPF-driven UFLS determines less amount of load shedding than in Config. II while still manages to obtain a high frequency nadir as well as keep the voltages and currents within safety ranges in the post-contingency steady state. For the Standard UFLS, as it is not capable to appreciate the presence of the BESS, the same issues have been observed as in Config. II. With the same amount of load shedding, there are still violations on the current ampacity for the line 13-14 and for the voltage magnitude at node 20. Regarding the No UFLS case, current ampacities for lines 13-14, 22-23 and 25-26, and the voltage limits for node 20, are still all largely violated.

5.4.3 Expected Energy Not Served

The metric Expected Energy Not Served (*EENS*), defined as the expected amount of energy not being served to the demand during the UFLS action, is computed to compare the performance of the implemented UFLS methods. More specifically, it is assessed for a time period of 100

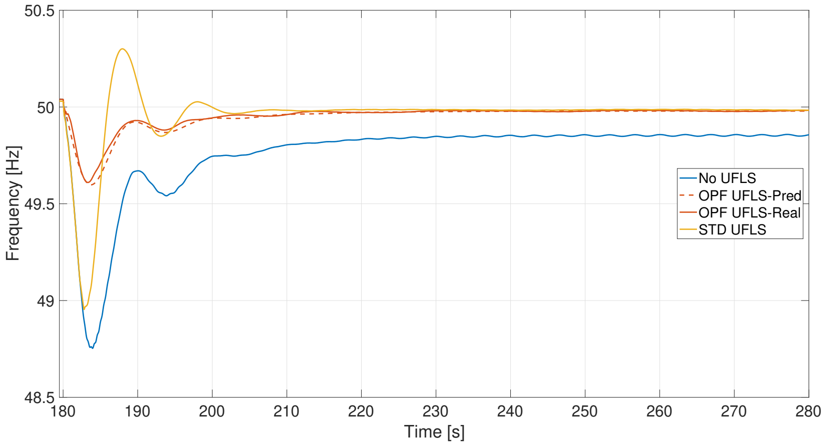

Figure 5.10 – Frequency trajectory for the 3 cases in Config. III: No UFLS (blue), Standard UFLS (yellow), OPF-driven UFLS prediction (dash read) and realization (solid red).

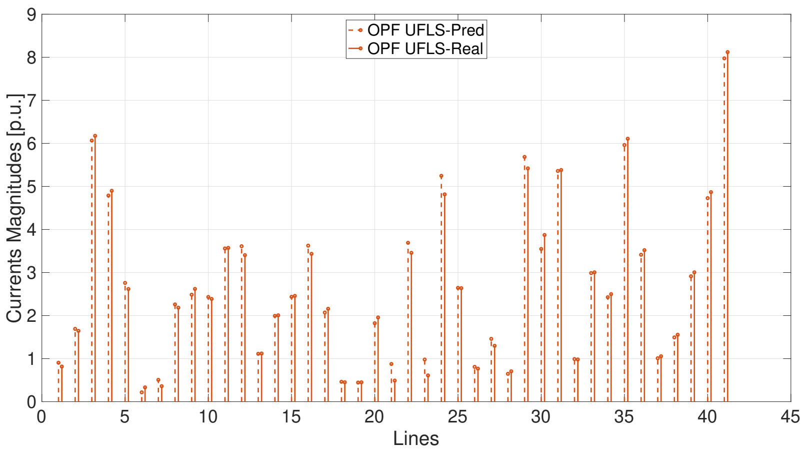

Figure 5.11 – Currents flow in all the lines for Config. III with OPF-driven UFLS: prediction (dash red) and realization (solid red).

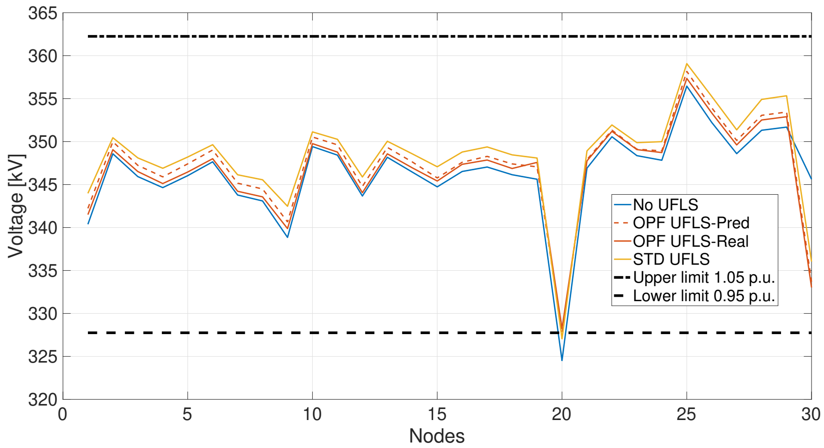

Figure 5.12 – Nodal voltages for the 3 cases in Config. III: No UFLS (blue), Standard UFLS (yellow), OPF-driven UFLS prediction (dash red) and realization (solid red). The dash and solid black lines are the upper and lower limits of the nodal voltage, respectively.

seconds[3] after the contingency, expressed as

$$EENS = \sum_{t=t_0}^{t_s} \sum_{l=1}^{L} \Delta P_{l,LS} \Delta t \tag{5.33}$$

where t_0 is the time when the contingency happened, t_s is equal to $t_0 + 100\ s$, and L is the total number of load buses.

Table. 5.3 summarizes the *EENS*, the voltage magnitude limits and line ampacity violated in all the studied cases. It should be noted that the values provided in Table 5.3 have not considered the *EENS* caused by the line tripping due to the ampacity and voltage limits violations. Thanks to properly considering the presence of the BESS providing primary frequency regulation to the grid, the OPF-driven UFLS scheme not only respects all the physical limits but also reduces the *EENS* in Config. III to be 77% of the one in Config.II. In contrast, the Standard UFLS fails to take advantage from the BESS, being myopic to the frequency regulation service provided by the BESS. It is observed that the Standard UFLS determines the same amount of load shedding for Config. II and Config. III, leading to the same amount of *EENS* and voltage and current limits violations.

5.4.4 Calibration of the System Damping Coefficient

As the the system frequency response is modeled on the basis of the swing equation (5.5), it is worth investigating the effect of the damping coefficient calibration (5.16) on the performance of the frequency tracking. To this end, the OPF-driven UFLS scheme without damping coeffi-

[3]Since the low-inertia 39-bus power grids have entered into post-contingency steady states in 100 seconds after the contingency and the cascading events (e.g. line tripping due to ampcity or voltage limits violations) are not considered in this work, it is not necessary to compute *EENS* in a longer time range.

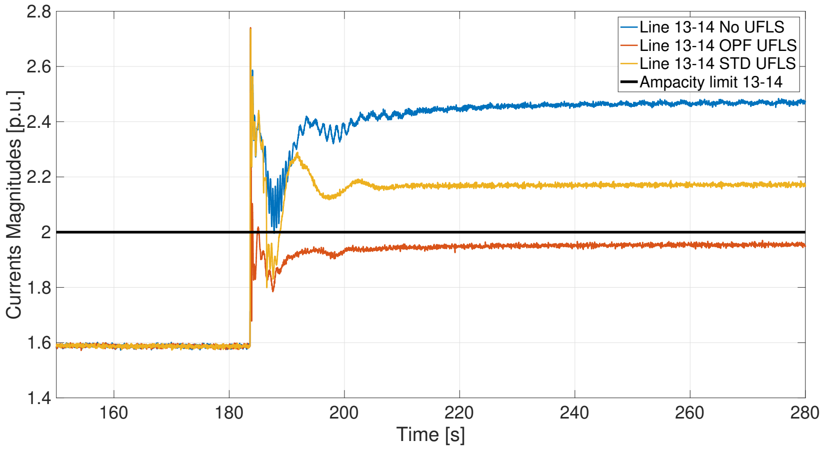

(a) Line 13-14.

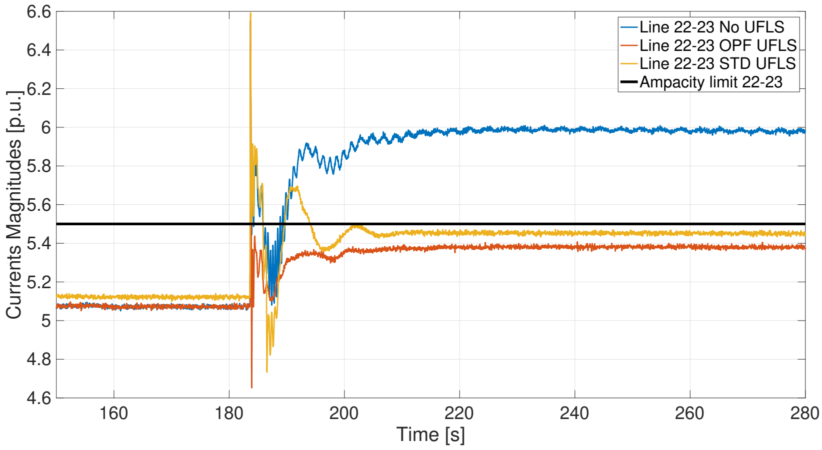

(b) Line 22-23..

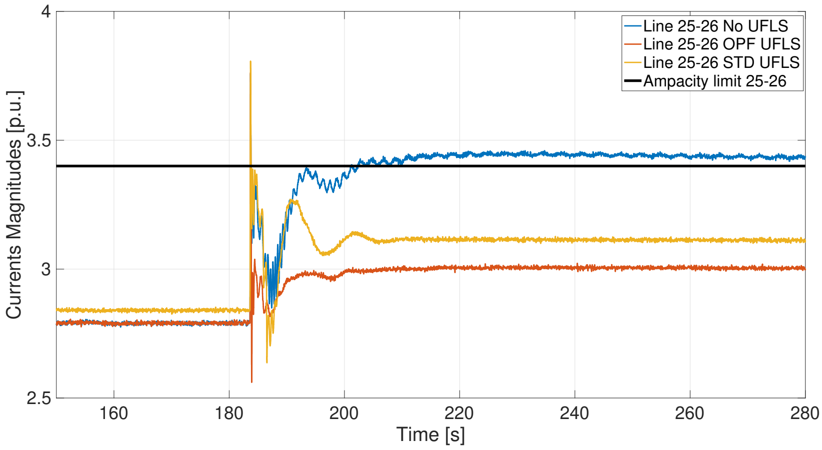

(c) Line 25-26.

Figure 5.13 – Current ampacity and line current for the 3 cases in Config. III: No UFLS (blue), Standard UFLS (yellow), OPF-driven UFLS prediction (dash red) and realization (solid red). The black lines are the ampacity of line 13-14, line 22-23 and line 25-26, respectively.

Table 5.3 – EENS, voltage magnitude limits and line ampacity violations.

		Voltage and current limits violated	EENS [MWh]
Config. II	**No UFLS**	Nodes 20 Line 13-14 Line 22-23 Line 25-26	-*
	Standard UFLS	Nodes 20 Line 13-14	10.54*
	OPF-driven UFLS	No violation	12.54
Config. III	**No UFLS**	Nodes 20 Line 13-14 Line 22-23 Line 25-26	-*
	Standard UFLS	Nodes 20 Line 13-14	10.54*
	OPF-driven UFLS	No violation	9.66

* This value does not consider the *EENS* caused by the line tripping due to the ampacity and voltage limits violations.

cient calibration is tested in Config. II and Config. III for the same contingency (i.e., tripping of G4) considered in Section 5.4.1 and Section 5.4.2. For the sake of brevity, the OPF-driven UFLS scheme with damping coefficient calibration are denoted as OPF-UFLS-1 and the OPF-driven UFLS scheme without damping coefficient calibration are denoted as OPF-UFLS-2.

The details of load shedding determined by the OPF-UFLS-1 and OPF-UFLS-2 are compared in Table 5.4. It illustrates that the OPF-UFLS-2 determines very similar amount of load shedding as the OPF-UFLS-1 for both Config. II and Config. III. This is because the solution space of the optimization problem is binded by the post-contingency line ampacity and voltage limits, rather than by the frequency limits. Fig. 5.14a and Fig. 5.14b exhibit the frequency predicted

Table 5.4 – Load shedding plans determined by OPF-UFLS schemes.

	OPF-UFLS-1		**OPF-UFLS-2**	
Config. II	Total	407.1 MW	Total	407.9 MW
	load 15	95.2 MW	load 15	95.8 MW
	load 20	308.8 MW	load 20	308.8 MW
	load 39	8.1 MW	load 39	8.3 MW
Config. III	Total	316.2 MW	Total	316.5 MW
	load 20	285.2 MW	load 20	285.2 MW
	load 39	31.0 MW	load 39	31.3 MW

Table 5.5 – Mean errors of frequency trajectory prediction during transient.

	OPF-UFLS-1	**OPF-UFLS-2**
Config. II	0.0224 Hz	0.0272 Hz
Config. III	0.0128 Hz	0.0144 Hz

by OPF-UFLS-1 and OPF-UFLS-2 and the real system frequency for Config. II and Config. III, respectively. On one hand, for both Config. II and Config. III, the difference between the post-contingency frequency predicted by OPF-UFLS-1 and the one by OPF-UFLS-2 is negligible. As a result, the solution space of the optimization problem for OPF-UFLS-1 is very close to the one for OPF-UFLS-2. On the other hand, the transient frequency trajectories predicted by the two OPF-driven UFLS schemes exhibit discernible differences. The mean value of the frequency prediction errors during transient (t from 180 s to 220 s) for OPF-UFLS-1 and OPF-UFLS-2 are summarized in Table 5.5. It illustrates that, with the damping coefficient calibration, OPF-UFLS-1 achieves better frequency prediction during the transient.

It is also worth to note that the OPF-UFLS-2 is always more conservative than the OPF-UFLS-1, as the calibration increases the system damping coefficient. As shown in Figure 5.14a and Figure 5.14b , the frequency nadir predicted by OPF-UFLS-2 are lower than the OPF-UFLS-1 in both config. II and Config. III. In this respect, when the damping-shedding coefficient α in (5.16) is not available, implementing OPF-UFLS-2 can still ensure the system respect to the frequency limits with an equivalently good load shedding allocation.

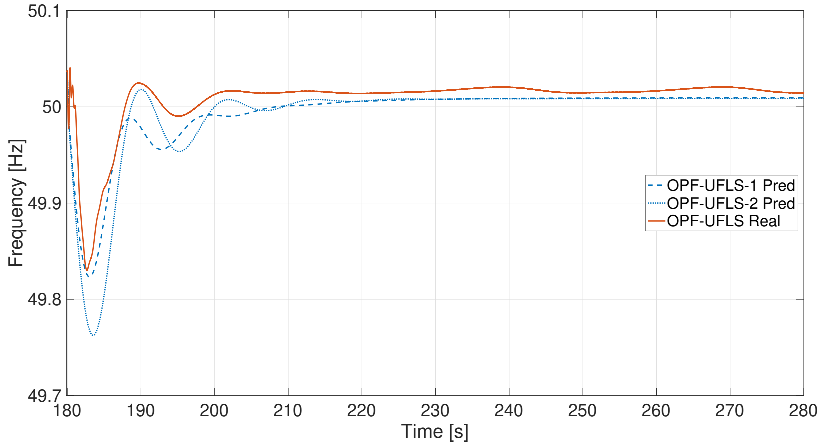

(a) Config. II.

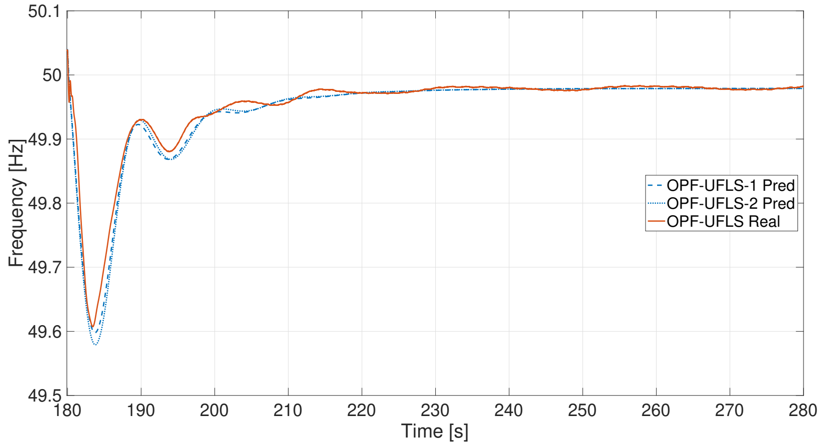

(b) Config. III.

Figure 5.14 – Frequency trajectory for OPF-driven UFLS schemes.

5.5 Conclusions

This Chapter has assessed the performance of a centralized OPF-driven UFLS scheme when used in low-inertia power systems hosting large-scale battery energy storage systems. The numerical evaluation has demonstrated the high prediction fidelity of the OPF-driven UFLS method. The Chapter has also discussed the effect of damping coefficient calibration on the frequency tracking, showing that the calibration mainly affects the transient frequency prediction and barely impacts the post-contingency frequency prediction.

Compared with the traditional ENTSO-E recommended UFLS scheme, the OPF-driven UFLS method exhibits the following advantages.

- The adopted frequency response model enables the OPF-driven UFLS approach to correctly predict system frequency, ensuring a better frequency containment.
- By leveraging the system real-time situational awareness enabled by PMUs/RTUs, the post-contingency voltages and currents states are correctly predicted, allowing the OPF-driven UFLS to successfully prevent the system from further lines tripping caused by nodal voltages and branch current limits violations.
- The benefit associated to the presence of a large-scale BESS are better leveraged by the OPF-driven UFLS, for which the presence of the BESS produces less *EENS* while still keeping the system in feasible operational states. On the contrary, the Standard UFLS does not take advantage of the presence of large-scale BESSs since it is myopic regarding its presence.

6 Impact of Synchrophasor Estimation Algorithms on RoCoF-based Under Frequency Load Shedding

In view of the need for faster and adaptive under frequency load shedding (UFLS) protection schemes to secure the system in case of contingency, UFLS schemes based on Rate-of-Change-of-Frequency (RoCoF) provide a more responsive and effective solution than traditional approaches solely based on frequency. In this respect, Phasor Measurement Units (PMUs) may play an important role in the development of enhanced UFLS control schemes that leverage both frequency and RoCoF measurements. In this context, the Chapter proposes an effective local UFLS and Load-Restoration (LR) scheme that relies on RoCoF and frequency measurements provided by PMUs and then investigates the impact of synchrophasor estimation algorithms on the load shedding action of the proposed relay scheme. Two consolidated window-based synchrophasor estimation algorithms, as representative approaches based on static and dynamic signal models, are compared with a focus on the appropriateness of using PMU-based RoCoF measurements. In particular, this Chapter examines the impact of the class of performance (i.e., the window length) and the signal model (i.e., static or dynamic) on the action of RoCoF-based UFLS scheme outcomes. The performance of the proposed relay scheme is assessed through numerical simulations of a time-domain dynamic model of the IEEE 39-bus power system, hosting a substantial amount of wind generation.

This Chapter includes results of publication [133].

6.1 Introduction

Subsequent to a large power system's contingency, UFLS schemes determine the amount of shed loads relying on under-frequency relays that operate on frequency estimates. When applying the under-frequency relays, the system frequency must already decrease to a sufficiently low value before the relays operate [68]. This can delay load shedding and, consequently, cause issues for the system restoration, especially for power systems with a large share of non-synchronous resources since they are more likely to experience fast dynamics. An example is the severe blackout event in South Australia power system on 28 September 2016, when a wind storm hit the region while half of the power consumption was fed by wind generation [21]. Following the loss of power in-feed from the wind farm and import from Victoria (via Heywood interconnector), the South Australia system frequency fell so fast that the UFLS schemes were unable to arrest the fall, resulting in a blackout [21, 64].

In this context, UFLS schemes relying on RoCoF estimates may potentially lead to a faster system restoration as RoCoF can be seen as a predictive quantity whose output accounts for the variation of frequency polarity and velocity. Applying thresholds on estimated RoCoF values makes it possible to promptly detect critical conditions, even before the frequency has fallen below abnormal operation levels.

Most existing schemes that adopt RoCoF thresholds to trigger the load shedding action, only analyze and acknowledge the necessity of using RoCoF as an index for UFLS schemes, without providing a strategy to actually measure it [80, 81, 82]. Indeed, frequency and RoCoF are computed using simplified system frequency response models or by assuming the information of the studied power grid is fully available, rather than using actual measuring devices (e.g., PMUs). In this regard, PMUs characterized by high reporting rate and remarkable measurement accuracy [73, 83] might represent a promising solution. As a matter of fact, PMUs are able to provide frequency and RoCoF estimates with a reporting rate in the order of tens of frames per second [134, 135] and with accuracy levels of 10^{-4} Hz ad 10^{-2} Hz/s [136].

Within this context, this Chapter investigates the impact of synchrophasor estimation algorithms in RoCoF-based UFLS schemes. First, an analysis of the anticipatory property of RoCoF with respect to frequency in detecting large electro-mechanical transients is presented. Then, an effective local UFLS and Load-Restoration (LR) scheme is proposed. The proposed scheme relies on RoCoF and frequency measurements provided by PMUs. Furthermore, the strategy to tune the parameters of the proposed UFLS and LR scheme is provided. In order to assess the impact of the parameters tuning, two sets of RoCoF thresholds are selected. The impact of the synchrophasor estimation algorithms on the proposed RoCoF-based UFLS is analyzed by comparing two consolidated window-based synchrophasor estimators that are based on a static [137] and dynamic signal models [138], respectively. The performance of the proposed relaying scheme is assessed by means of numerical simulations carried out on the full-replica time-domain dynamic model of the IEEE 39-bus power system, hosting a substantial amount of wind generation.

The Chapter is structured as follows: Section 6.2 introduces the context of PMU-based RoCoF measurements. Section 6.3 provides details of the proposed UFLS and LR scheme. Section 6.4 describes the power grid model used in the simulation. Section 6.5 presents the ULFS performance assessment, including simulation scenarios, and results. Section 6.6 concludes the Chapter with a dedicated discussion.

6.2 PMU-based RoCoF Measurements

In general, the traditional control scheme of RoCoF-based relaying relies on four main steps [139]. First, a nodal voltage waveform is processed in order to extract the fundamental frequency. Then, the RoCoF is computed as the first-order time-derivative of frequency. Next, a low-pass filtering stage removes fast/noisy RoCoF dynamics, thus providing a smoother trend, yet introducing an inevitable time delay. Finally, the obtained measurements are compared with the specific thresholds, whose excess activates the control action.

Although the recent literature provides several solutions, it is not possible to identify a common guideline. The frequency estimation stage usually considers a relatively long window length, in the order of tens of periods, to improve the frequency resolution and estimation accuracy [69, 139]. The low-pass filtering stage is typically implemented as a moving average, whose window length has to be suitably scaled based on the expected variation range and bandwidth of RoCoF estimates. As a consequence of the adoption of long window lengths and averaging filters, time delays are introduced into the control scheme. Such time delays may significantly deteriorate the responsiveness of the load shedding action and are not compatible with the anomalous dynamics of modern power systems, e.g., [21].

Furthermore, during large electromechanical transients, power exchanges are taking place in a broad spectrum, well beyond the single fundamental component. Therefore, the definition of frequency and RoCoF associated to the fundamental component represents an open issue from the metrological point of view [140, 141, 79, 142, 143, 144, 145].

In a PMU-based scenario, instead, the IEEE Std C37.118.1 introduces stringent limits on the measurements reporting latency which make it challenging to perform the RoCoF estimation over window lengths of three/ five nominal cycles, i.e. 60 and 100 ms at 50 Hz, for P- and M-class[1], respectively [134]. With respect to the estimation accuracy, the above IEEE Standard requires RFE (Rate-of-Change-of-Frequency Error) to not exceed 0.01 Hz/s in steady-state conditions, and 6 Hz/s in the presence of harmonic distortion [135]. However, RoCoF measurements applied into real-world scenarios require a metering infrastructure more resilient against interfering components and characterized by faster dynamics. Indeed, in the South Australian blackout, the measured value of RoCoF has the same order of magnitude as the accuracy of RoCoF estimates imposed by the IEEE Std C37.118.1. Besides, the reporting latency should not exceed few tens of ms, since the frequency drop is extremely fast. In other words, PMUs should be able to provide fast and accurate RoCoF estimates independently from the variation speed of the fundamental frequency [146].

It is also worth to point out that PMUs are specifically designed to provide frequently updated measurements with a reporting rate in the order of tens of frames per second. Typically, they consider short window lengths without applying any moving average compensation. As a consequence, PMU estimates account for the quasi-instantaneous voltage and current

[1] M-class is intended for measurement applications requiring accurate synchrophasor estimates, whereas P-class is intended for mission-critical applications requiring fast responsiveness.

variations, but their accuracy tends to deteriorate in the presence of fast dynamic [142].

In this Chapter, two PMU-based RoCoF estimation techniques are considered, based on two consolidated state-of-the-art algorithms, i.e., the Enhanced Interpolated DFT (e-IpDFT) [137] and the Compressive Sensing-based Taylor-Fourier Model (cs-TFM) [138]. The two algorithms are selected for two reasons: (i) their implementation details have been fully presented in the current literatures, thus ensuring the reproducibility of obtained results; (ii) adopt different processing approaches, as they rely on different signal models, i.e., static for the e-IpDFT and dynamic for the cs-TFM. A static signal model computes RoCoF as the incremental ratio between two consecutive frequency estimates. It is thus reasonable to expect that the RoCoF estimates are partially delayed and can be smoothed depending on the adopted reporting rate. In contrast, a dynamic signal model is able to directly compute the instantaneous RoCoF as the second-order time-derivative of phase, since it is explicitly embedded in the signal model.

6.3 RoCoF-based Under Frequency Load Shedding

6.3.1 Anticipative Effects of RoCoF

This Section presents an analysis on the anticipating property of RoCoF measurements in detecting electro-mechanical transients in respect to frequency estimates. The study is meant to give a qualitative insight, since a quantitative and thorough study is grid-dependant and may only be provided via complex numerical simulations (see Section 6.4 and 6.5). For the sake of brevity, the rotating machines, loads and network elements are represented using simplified models.

It is assumed a prower grid in steady-state conditions, where N synchronous machines have the same electrical angular speed Ω_s. During electro-mechanical transients, the rotating machine's electro-mechanical power balance is expressed by the following well-know system of equations (e.g., [129]):

$$\begin{cases} \frac{d\Omega_i}{dt} = \frac{1}{M_i} \cdot (P_{mi} - P_{ei}) \\ \frac{d\delta_i}{dt} = \Omega_i - \Omega_s \end{cases} \tag{6.1}$$

where the index i denotes the considered synchronous machine, whereas Ω_i and δ_i are its angular speed and angular position with respect to a reference machine rotating at Ω_s. The terms P_{mi} and P_{ei} represent the mechanical driving power and the generated active electrical power, respectively, whereas M_i denotes the machine's inertia coefficient. As is well known, this set of differential equations shows how the time-derivative of the angular speed $d\Omega/dt$, i.e. the RoCoF, is proportional to the power imbalance in the grid.

Furthermore, as discussed in [147], in a power grid composed of N generation buses and M load buses, a change ΔP_j of active power at the jth load bus causes a change ΔP_{ei} of active power at the ith generation unit, given by:

$$\Delta P_{ei} = \frac{C_{ji}\Delta P_j}{\sum_{i\in N} C_{ji}} \tag{6.2}$$

$$C_{ji} = \frac{|\mathbf{K}_{ij}\mathbf{V}_G|\cos\theta_{ji}}{|\tilde{E}_j^{eq}|} \tag{6.3}$$

where $\mathbf{K}$ is an $N \times M$ matrix obtained from system admittance matrix, V_G is the generator bus voltage vector, $\tilde{E}_j^{eq} = \mathbf{K}_{ji}\mathbf{V}_G(j)$, and θ_{ij} is the angle between $\tilde{E}_j^{eq}$ and $\mathbf{K}_{ji}\mathbf{V}_G(i)$, and $\tilde{E}_j^{eq}$ denotes the Thevenin equivalent voltage at bus j.

The combination of (6.1), (6.2), and (6.3) shows why the RoCoF is an instantaneous indicator of the load-generation imbalance, providing an insight on why a RoCoF estimator might be used for a prompt and anticipative load shedding relaying scheme. When acquiring RoCoF measurements from PMUs that, by definition, are characterized by low reporting latency, it is possible to infer any large power imbalance much faster than when using simple frequency measurements.

6.3.2 RoCoF-based UFLS Scheme

The proposed RoCoF-based UFLS scheme is inspired from [83] and comprises two parts: the RoCoF-based Load Shedding (R-LS) and the frequency-based Load Restoration (f-LR). This dual mechanism has been designed and optimized in order to ensure a fast reaction to power shortage as well as a secure network-restoration process. In particular, the f-LR thresholds have been derived from the guidelines in [63].

The reason why RoCoF measurements are not used in LR process, is that during the network-restoration, the RoCoF values experienced by each bus strongly depend on the adopted restoration actions. On the one hand, it is quite difficult to infer all the possible attainable RoCoF values, on the other hand, a long-lasting positive RoCoF value, does not necessarily indicate that the grid has reached a stable status that could handle the connection of further loads. The recovery of system frequency towards nominal values, instead, is an unequivocal indicator of secure system state.

As shown in Table 6.1, the control action is scaled to the threshold level, i.e. larger RoCoF and frequency values correspond to larger amounts of loads to be shed or restored, respectively. For this analysis, two sets of RoCoF thresholds are considered in order to compare the performance of considered LS scheme as function of different load shedding shares. For the sake of brevity, the two RoCoF thresholds settings are denoted as R-LS-1 and R-LS-2. As for the restoration process, a single f-LR is implemented, referring to the guideline in [63].

For the purpose of a smooth and stable system restoration, time-delays should be applied between two consecutive control actions. As regards f-LR, a time delay of 5000 ms is considered, in order to avoid the load shedding repetitions or the occurrence of system instabilities [63].

Table 6.1 – RoCoF and frequency thresholds for LS and LR.

Load Share [%]		100	95	90	85	75	60	50
R-LS-1	R [Hz/s]		0.3	0.4	0.6	0.7	1	1.2
	p_{act} [%]		88	84	72	68	64	64
R-LS-2	R [Hz/s]		0.2	0.3	0.5	0.7	1	2
	p_{act} [%]		84	60	60	60	52	52
f-LR	f [Hz]	49.75	49.6	49.5	49.4	49.2	49	

However, to design a RoCoF-LS relay that uses RoCoF measurements from PMUs, it is necessary to consider the inaccuracies on the RoCoF estimation associated to the synchrophasor's estimation algorithm embedded in a given PMU. Indeed, after the contingency, it is reasonable to expect that the voltage signal is affected by amplitude and phase modulations. The combined effect of amplitude and phase modulations is evident in both voltage waveform and corresponding RoCoF estimation (e.g., Figure 6.3). In the IEEE Std C37.118.1, for the phase and amplitude modulation tests, the given formulas to compute frequency and RoCoF show that the magnitude of frequency deviation increases linearly with the frequency, whereas the RoCoF is increased with the square of the frequency. For this reason, the requirement on REF under amplitude and phase modulation tests has been relaxed to 3 Hz/s for P-class and 30 Hz/s for M-class [134]. In this regard, RoCoF estimates have to be suitably filtered to mitigate the instantaneous transients and the long term-damped oscillations of system frequency after a contingency event in order to avoid false triggering of UFLS. To this end, the RoCoF estimates $\hat{R}$ are evaluated over an observation window interval of 500 ms, as recommended in [148]. Given a PMU reporting rate of 50 frames per second, this corresponds to a set of 25 consecutive RoCoF estimates.

In Table 6.1, the adopted RoCoF-LS relay embeds RoCoF thresholds R and activation thresholds p_{act}. As shown in Algorithm 1, the load shedding activation criterion is a combination of the RoCoF and activation thresholds. For each RoCoF threshold $R(i)$, the probability of the RoCoF estimates $\hat{R}$ exceeding $R(i)$ in the 500 ms observation window is computed. The calculated probability is denoted as p. If p is larger than the activation level p_{act}, the corresponding load share is activated. In the condition of multiple thresholds that are simultaneously activated, only the most severe control action is implemented, i.e. the largest share of loads is shed. As regard the f-LR case, the loads start to restore when the frequency value exceeds 49 Hz. The amount of load restoration escalates as the increase of the frequency.

It should be noted that in Table 6.1 the load share is defined as a percentage of the installed load. It is also worth pointing out that the adopted RoCoF and activation thresholds, i.e., R and p_{act}, are grid-dependent and can be obtained through dedicated sensitivity studies. In this respect, a strategy to tune these parameters, as well as a quantitative analysis on the interference of voltage modulation, are proposed in Section 6.4 referring to the targeted

Algorithm 1 LS and LR Load Share Selection

input: estimated $\hat{f}$ and $\hat{R}$, thresholds R-LS and f-LR
output: LS or LR Load Share
Load-Shedding Share Selection
for i = 1 : length(R-LS)
  if $\hat{R} > R$(i) $\wedge$ $p > p_{act}(i)$
    LS Share = R-LS(i)
    reset probability $p = 0$
    set time delay < 500 ms
  end if
end for
Load-Restoration Share Selection
for i = 1 : length(f-LR)
  if $\hat{f} > f$(i)
    LR Share = f-LR(i)
    time delay = 5000 ms
  end if
end for

electrical grid, i.e., the IEEE 39-bus power grid.

6.3.3 UFLS Scheme Implementation

The adopted RoCoF-based UFLS scheme is local, namely the relays located in different nodes do not exchange information and the load shedding is performed only based on the locally measured RoCoF and frequency values.

Within the simulated three-phase power system, each load bus is equipped with a PMU that measures the bus voltage amplitude, frequency and RoCoF associated to phase A. In order to reproduce a plausible measurement noise, the voltage waveform acquired by the PMU is corrupted by an additive white Gaussian noise, resulting a Signal-to-Noise Ratio (SNR) of 80 dB. The diagram of Figure 6.1 shows how the UFLS scheme is coupled with the adopted dynamic load model. Once completed the estimation process, the PMU streams the measured RoCoF and frequency to the UFLS relay, which determines the LS or LR load share based on the thresholds in Table 6.1.

6.4 Simulation Model

The impact of the considered synchrophasor estimation algorithms on the performance of the proposed RoCoF-based UFLS plan is demonstrated in an adapted IEEE 39-bus power grid (see in Figure 6.2). In order to take into account the increasing deployment of renewable generation in modern power grids, the IEEE 39-bus benchmark network is modified by adding 4 wind power plants. It is worth noting that the dynamic models used in this Chapter are the

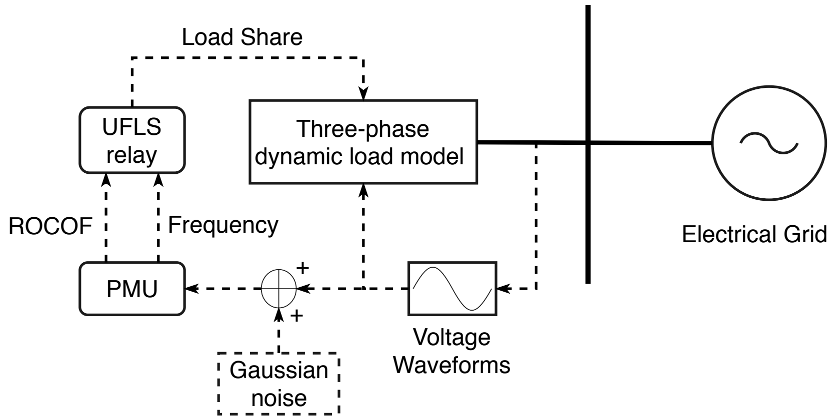

Figure 6.1 – Diagram of the UFLS scheme coupling with the dynamic load model.

Table 6.2 – List of generation units.

Generation Unit	Plant Type	Installed Capacity [MVA]	FR /Location
G1	Thermal Plant	3000	PFR, SFR
G2–G4, G6–G10	Hydro Plant	1000	PFR
G5	Hydro Plant	520	PFR
Wind Plant 1	Type-III DFIG	300	bus 2
Wind Plant 2		150	bus 21
Wind Plant 3		400	bus 8
Wind Plant 4		500	bus 11

models adopted in the whole manuscript. The data and modeling details of each device are available in the Appendix A.

The description presented below is meant to introduce the implemented frequency regulations (Section 6.4.1), present the source of adopted wind profiles (Section 6.4.2), and highlight the importance of using the dynamic load model (Section 6.4.3).

6.4.1 Synchronous Generators

The conventional generation asset is identical to the one of Config. I introduced in Chapter 3, Section 3.2. It consists of both hydro- and thermal-power plants. The synchronous generator model and data are provided in Appendix A.1. Each generator's governor includes a Primary Frequency Regulator (PFR) with a droop coefficient of 5%. The thermal-power plant (i.e., G1), that accounts for the highest installed capacity, is also implemented with a Secondary Frequency Regulator (SFR), whose integration time constant is set equal to 120 s. The diagram of synchronous generator PFR and SFR is presented in Chapter 4, Figure 4.5. As a summary, Table 6.2 reports the plant type, nominal capacity and frequency regulation for each generator.

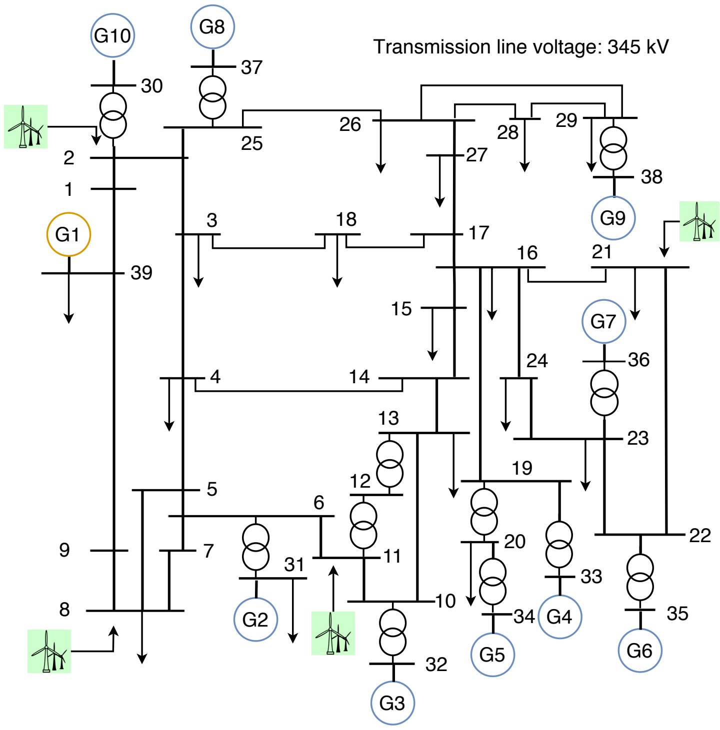

Figure 6.2 – Diagram of the modified IEEE 39-bus power system.

6.4.2 Wind Generation

Table 6.2 also shows the plant type, nominal capacity and location of the 4 wind power plants. The generator is modeled as type-III Doubly-Fed Induction Generator (DFIG) that consists of an asynchronous machine and a back-to-back converter. Modeling details of the wind power plants are presented in Appendix A.4. For this analysis, the wind profiles are generated at 1 second resolution by re-sampling the measurements at 1 minute resolution from ERCOT [149]. The re-sampling approach is based on iterated smoothing and differentiating operations that use the statistical characteristics of the aggregated wind generation profiles presented in [150].

6.4.3 Dynamic Load Model

Static load models, including constant impedance, constant current model, and constant power models, are well known in the literature and can be easily implemented [151]. Nevertheless, such static models do not provide an accurate approximation of the load frequency and voltage responses. In order to reproduce a plausible dynamic load behavior, the EPRI LOADSYN model has been adopted [100]. The design and implementation of the EPRI LOADSYN model are provided in Appendix A.2.

6.4.4 Phasor Measurement Units

This study compares the two different RoCoF estimation techniques based on two consolidated state-of-the-art algorithms, namely e-IpDFT [137] and cs-TFM [138]. The details regarding their implementation within the adopted real-time simulator are provided in [119] and [152], respectively.

The e-IpDFT PMU adopts an enhanced version of the IpDFT to estimate the synchrophasor associated to the fundamental component of the power signal under analysis. Such technique, described in Algorithm 2, is specifically designed to mitigate the effects of long-range spectral leakage produced by the negative image of the fundamental component.

Algorithm 2 e-IpDFT

1: $x[n] := \{x(t_n) \quad | \quad t_n = nT_s,\, n = [0, \dots N-1] \in \mathbb{N}\}$
2: $X(k) = \mathtt{DFT}(x[n] \cdot w[n])$
3: $\{\widehat{f}, \widehat{A}, \widehat{\varphi}_0\} = \mathtt{IpDFT}(X(k))$
4: $\widehat{X}^{-}(k) = \mathtt{wf}(-\widehat{f}, \widehat{A}, -\widehat{\varphi}_0)$
5: $\widehat{X}^{+}(k) = X(k) - \widehat{X}^{-}(k)$
6: $\{\widehat{f}, \widehat{A}, \widehat{\varphi}_0\} = \mathtt{IpDFT}(\widehat{X}^{+}(k))$
7: $\hat{R} = \mathrm{diff}(\hat{f}) / T_r$

First, the PMU acquires a discrete time-series of samples $x[n]$, where $x(t)$ is the time-variant power system signal under analysis, N is the number of samples contained in the considered observation interval and $F_s = T_s^{-1}$ is the sampling rate (line 1). The signal is windowed with the Hanning function $w[n]$ to reduce the long-range spectral leakage effects, then the weighted signal DFT $X(k)$ is computed (line 2).

The IpDFT technique applied to the highest DFT bins, provides a preliminary estimate of the fundamental parameters (line 3). With respect to the location of the highest amplitude bin k_m, the fractional correction term δ is given by:

$$\delta = \varepsilon \cdot \frac{2 \cdot |X(k_m + \varepsilon)| - |X(k_m)|}{|X(k_m + \varepsilon)| + |X(k_m)|} \tag{6.4}$$

and is used to refine the fundamental parameter estimates as:

$$\begin{aligned} \hat{A} = |X(k_m)| \left| \frac{\pi\delta}{\sin(\pi\delta)} \right| \left|\delta^2 - 1\right| \qquad & \hat{\varphi}_0 = \angle X(k_m) - \pi\delta \\ \hat{f} = (k_m + \delta) F_s / N \qquad & \hat{R} = \mathrm{diff}(\hat{f}) / T_r \end{aligned} \tag{6.5}$$

These values enable us to reconstruct the component's negative image $\widehat{X}^{-}(k)$ (line 4), and subtract it from the original DFT bins, that now account only for the fundamental component's positive image $\widehat{X}^{+}(k)$ (line 5). In this reduced-leakage scenario, the IpDFT is applied again for a further enhanced estimation of the fundamental parameters $\{\hat{f}, \hat{A}, \hat{\varphi}_0\}$ (line 6). Finally, the fundamental RoCoF $\hat{R}$ is computed as the finite difference between two consecutive frequency estimations, divided by the reporting period T_r (line 7).

The cs-TFM PMU adopts a formulation of the Taylor-Fourier Transform (TFT), that has been suitably modified and generalized in order to deal also with multi-tone power signals. Thanks to a Taylor series expansion truncated to the second derivative order, it is possible to include the fundamental frequency and RoCoF within the estimator state variables as the first and second time-derivative of the phase angle, respectively.

The cs-TFM method recovers the spectral support $\mathscr{S}$ through an Orthogonal Matching Pursuit (OMP) algorithm, i.e. a *greedy* selection routine that exploits the assumption that the signal spectrum is sparse and consists only of a limited number of narrow-band components. The support recovery stage might suffer from the poor frequency resolution provided by DFT when short observation intervals are taken into account. In order to partially overcome this limitation, the cs-TFM method applies a CS-based super-resolution technique to reduce the bin spacing by one order of magnitude (line 1 of Algorithm 3).

As shown in Algorithms 3, the first step consists in enhancing the frequency resolution by projecting X over the vector space spanned by matrix D_f. In more detail, the matrix columns are designed to account for leakage effects over a super-resolved grid, whose bin spacing is set to 1.515 Hz (line 1). The fundamental frequency $\hat{f}_0$ is associated to the maximum bin of the super-resolved spectrum (line 2). Then, the first four harmonic terms are included into the spectral support $\mathscr{S}$ (line 3). Given the recovered support $\mathscr{S}$, the corresponding TFM matrix M is constructed (line 4) and the corresponding fundamental synchrophasor coefficients p are computed as follows (line 5):

$$p = \{p^0, p^1, p^2\} = (M^\dagger M)^{-1} M^\dagger \cdot x \tag{6.6}$$

where the superscript denotes the derivative order, $M^\dagger$ is the conjugate transpose of M and the subscript {-1} denotes the inverse operator. Based on this, the fundamental synchrophasor, frequency and RoCoF are extracted (line 6):

$$\begin{aligned} \hat{A} &= |p^0|, & \hat{A}^1 &= 2\Re(p^1 \cdot e^{-j\hat{\varphi}}) \\ \hat{\varphi} &= \angle p^0, & \varphi^1 &= \frac{\Im(p^1 \cdot e^{-j\hat{\varphi}})}{\hat{A}} \\ \hat{f} &= \hat{f}_0 + \frac{\hat{\varphi}^1}{2\pi}, & \hat{R} &= \frac{\Im(p^2 \cdot e^{-j\hat{\varphi}}) - \hat{A}^1 \cdot \hat{\varphi}^1}{2\pi \cdot \hat{A}} \end{aligned} \tag{6.7}$$

where $\hat{R}$ denotes the estimated RoCoF, and f_0 is the fundamental frequency within the recovered spectral support.

For each algorithm, two window length are considered, as representative of P- and M-class PMUs. Specifically, three- and five-cycle windows are selected, corresponding to 60 ms and 100 ms at the rated power system frequency of 50 Hz, respectively.

Algorithm 3 cs-TFM

1: $Y = D_f^{\dagger} \cdot X$
2: $\hat{f}_0 = \max(Y)$
3: $\mathscr{S} = \{\hat{f}_0 \cdot [1,2,3,4]\}$
4: $M = TFM(\mathscr{S})$
5: $p = (M^{\dagger} M)^{-1} M^{\dagger} \cdot x$
6: $\hat{f}_0, p \rightarrow \{\hat{A}, \hat{f}, \hat{\varphi}, \hat{R}\}$

6.4.5 Tunning of UFLS Scheme Parameters

This Section first discusses how post-contingency voltage modulations interferes with the RoCoF estimation, then presents a sensitivity study that enables the tuning of the UFLS scheme parameters.

As an example to demonstrate how post-contingency voltage modulation interferes with the RoCoF estimation, Figure 6.3 presents a voltage waveform and its corresponding RoCoF measurements in the IEEE 39-bus power grid experiencing a large contingency. Specifically, at $t = 180$ s a total amount of 1.5 GW generation power is tripped. The waveforms refer to bus 26, but similar considerations hold for the rest of the buses. The RoCoF estimates are provided by 4 PMUs: for both e-IpDFT and cs-TFM, we implement two different configurations, as representative of P- and M-class of IEEE Std c37.118.1 [134].

By means of the curve fitting tool provided by MATLAB, the voltage waveform is fit with a model consisting a sum of sines (one representing the fundamental tone, two for the amplitude modulation, two for the phase modulation). Thereby the modulations of the waveform are characterized in terms of depth and frequency: 12.90% and 5.27 Hz for the amplitude modulation, and 153 mrad and 4.23 Hz for the phase modulation. In the first modulation period T_{VM}, the voltage modulation significantly affects the RoCoF estimation, and the 4 PMUs provide unreliable results (refer to Figure 6.3b). Conversely, the RoCoF measurements become way more consistent when the voltage modulation is damped, as illustrated in the zoomed window in Figure 6.3b. Therefore, it is recommended to wait for a proper time interval before relying on a RoCoF estimate. In this context, the adopted 500 ms observation interval, as described in Section 6.3.2, is necessary.

A similar sensitivity study allows for the tuning of the RoCoF thresholds R and the activation thresholds p_{act}, as a function of the severity of the power outage. Specifically, dedicated simulations for the tripping of 1.0 GW, 1.25 GW, 1.5 GW, 1.75 GW are conducted in order to analyze the frequency dynamics after these critical events are analyzed. Figure 6.4 shows the simulation results, as reported by a P-class e-IpDFT PMU at bus 26 (similar results hold for all buses and for all PMUs). As illustrated in Figure 6.4b, the most severe contingency corresponds to the fastest frequency decrease, i.e., largest RoCoF. Briefly, the larger the measured RoCoF, the larger the detected contingency and, therefore, the larger the amount of loads to be shed. This is consistent with the RoCoF thresholds R in Table 6.1. In a similar way, also the activation

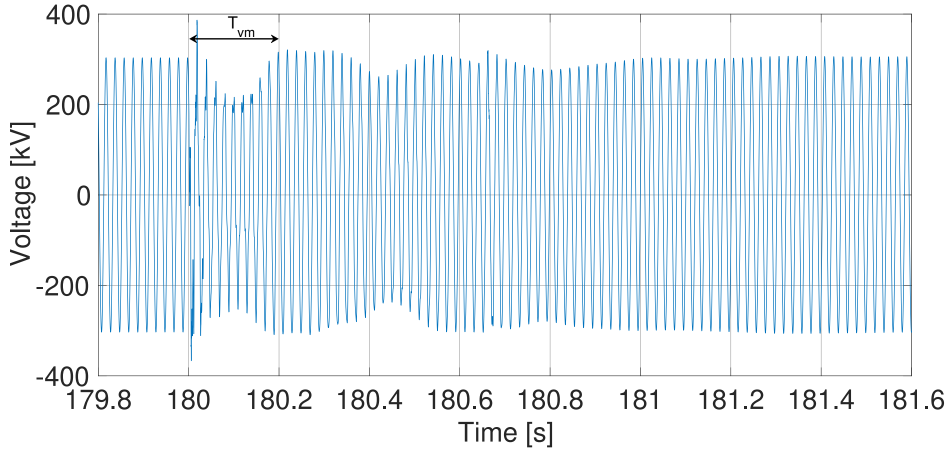

(a)

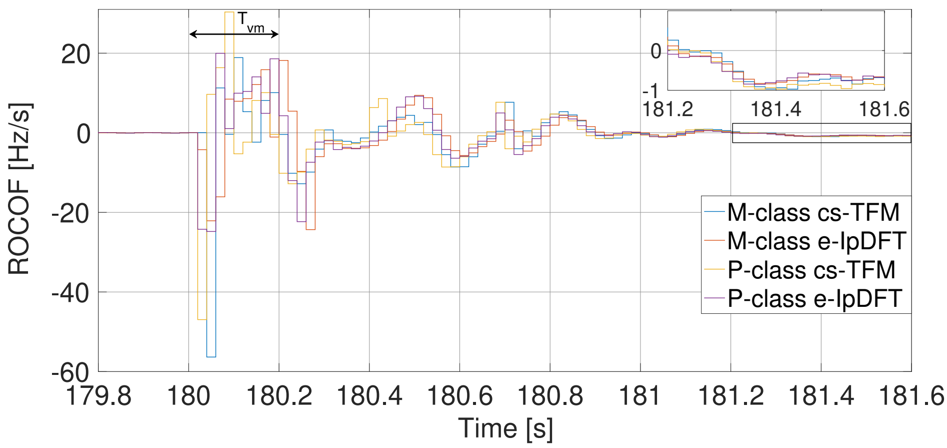

(b)

Figure 6.3 – Example of voltage modulation interfering with RoCoF estimation. Voltage waveform (a); RoCoF measurements (b).

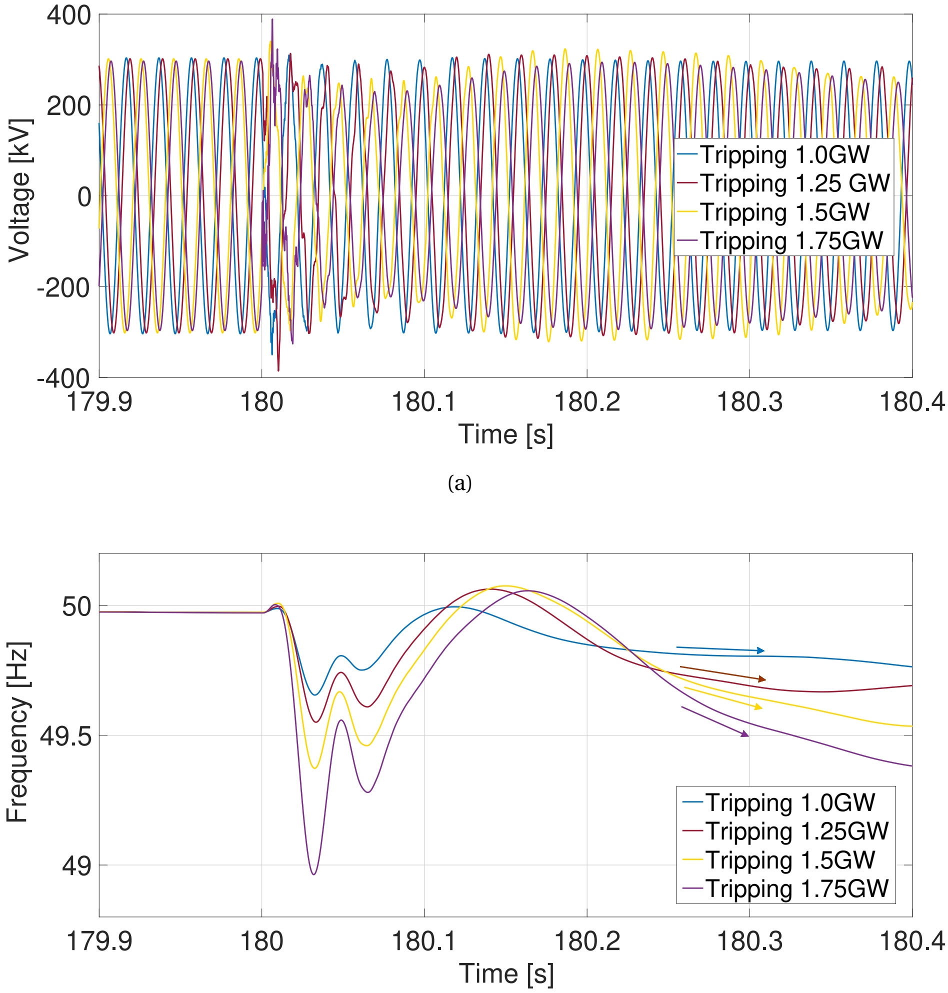

(a)

(b)

Figure 6.4 – Sensitivity study results. Voltage waveform on bus 26 (a); Frequency measurements on bus 26 by P-class e-IpDFT PMU (b).

thresholds p_{act} are tuned with respect to the contingency severity. As reported in Table 6.1, the larger the detected contingency, the faster the UFLS should act, therefore, the lower the activation threshold.

6.5 Validation Results

This section numerically assesses the performance of the proposed UFLS strategy with a focus on the impact of the synchrophasor estimation algorithm and of the UFLS parameters. As described in Section 6.4, the UFLS strategy is embedded within the modified IEEE 39-bus power system, where a large contingency event is simulated. In the considered contingency event, G4, G6 and G7 (1.5 GW total generation) are tripped at $t = 180$ s. For each synchrophasor estimation algorithm, two different configurations are implemented, as representative of M- and P-class of IEEE Std c37.118.1 [134].

In order to study whether different thresholds can affect the performance of the overall control scheme, the tests are repeated with both R-LS-1 and R-LS-2. The simulation results for R-LS-1 an R-LS-2 are respectively shown in Figure 6.5 and Figure 6.6, in terms of measured RoCoF and active power profiles. For the sake of clarity, the following figures consider a single representative load for each class, i.e., load 16 for M-class and load 4 for P-class.

Regarding the RoCoF measurements from the 4 PMUs, for the PMU M-class configuration, Figure 6.5a and Figure 6.6a show the RoCoF measurements provided by cs-TFM and e-IpDFT for R-LS-1 and R-LS-2, respectively, and for the PMU P-class configuration, Figure 6.5c and Figure 6.6c show the RoCoF measurements provided by cs-TFM and e-IpDFT for R-LS-1 and R-LS-2, respectively. As shown in the figures, right after the contingency, the cs-TFM estimates of RoCoF anticipate the e-IpDFT ones by one reporting period (i.e. 20 ms). This anticipatory effect is explained by the fact that cs-TFM adopts a dynamic signal model that allows for a direct estimation of the phase second-order time-derivative (i.e., the RoCoF), whereas e-IpDFT adopts a static signal model that calculates RoCoF as the incremental ratio between two consecutive frequency estimates. This is particularly noticeable within the first 300 ms after the contingency. As RoCoF-LS starts to be triggered, this effect is less visible.

The corresponding active powers are displayed in Figure 6.5b, Figure 6.6b, Figure 6.5d and Figure 6.6d, and illustrate the control actions of R-LS and f-LR control scheme. Given R-LS-1 thresholds for M-class configuration, the zoomed window in Figure 6.5b shows that the e-IpDFT sheds a larger share of loads (+25%) 1.3 s earlier than the cs-TFM. Given R-LS-2 thresholds for M-class configuration, the zoomed window in Figure 6.6b shows that the same amount of loads is shed by both cs-TFM and e-IpDFT, yet the e-IpDFT sheds earlier and the cs-TFM determines a faster system restoration. It is also observed that, using both R-LS-1 and R-LS-2, e-IpDFT sheds earlier whereas cs-TFM restores before. While the cs-TFM estimates of RoCoF anticipate the e-IpDFT ones by one reporting period, the e-IpDFT estimates are characterized by higher RoCoF values than those of cs-TFM. Therefore, in accordance with the threshold in Table I, it is reasonable to expect that the e-IpDFT estimates activate a larger

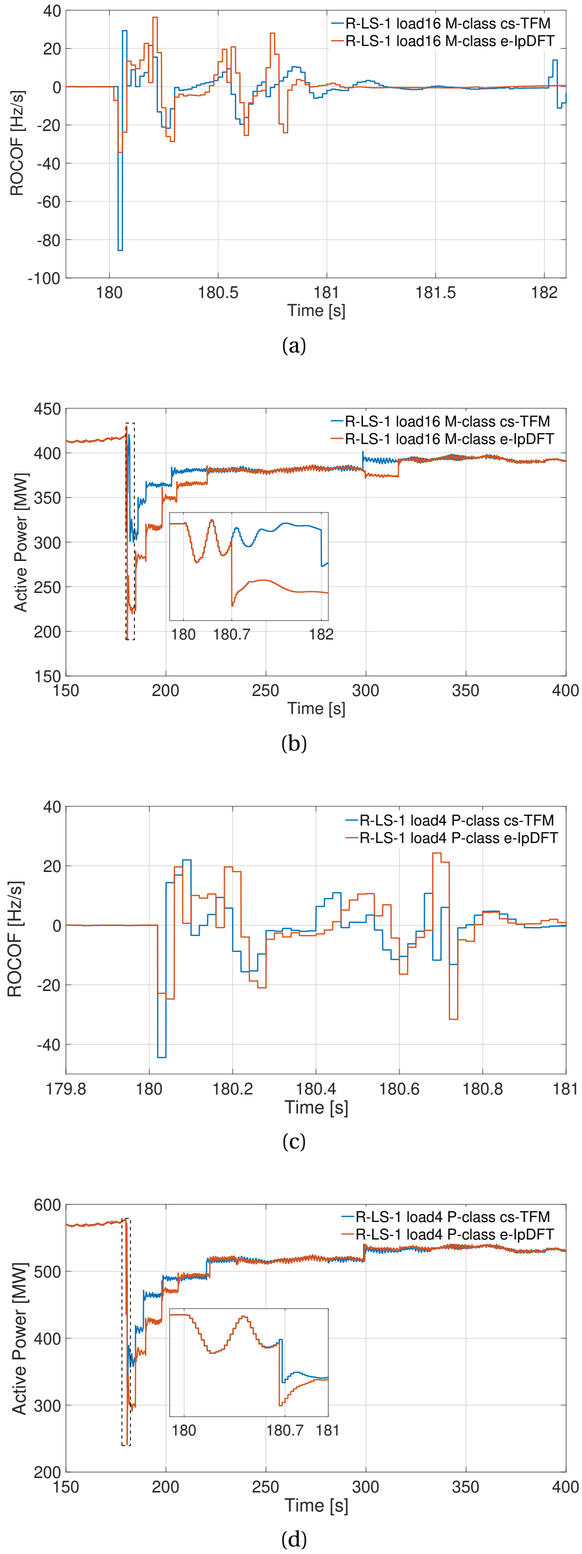

Figure 6.5 – PMU-based RoCoF measurements and corresponding active power profiles for *R*-LS-1 thresholds: (a) and (b) refer to load 16 and PMU M-class configuration, whereas (c) and (d) refer to load 4 and PMU P-class configuration.

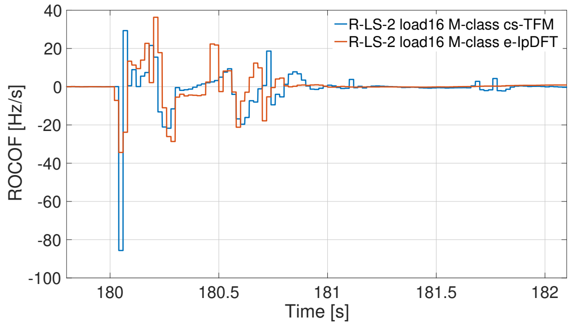

(a)

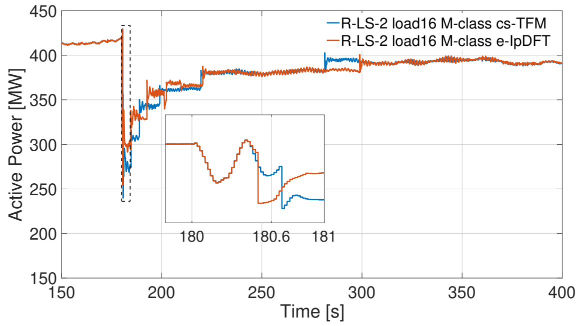

(b)

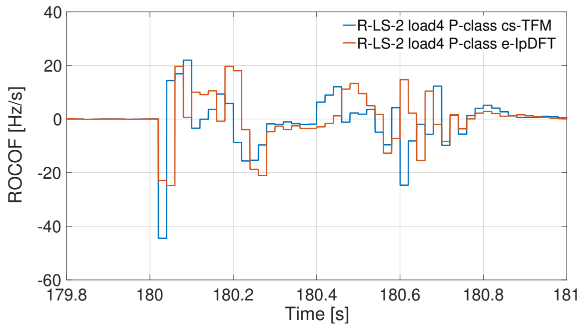

(c)

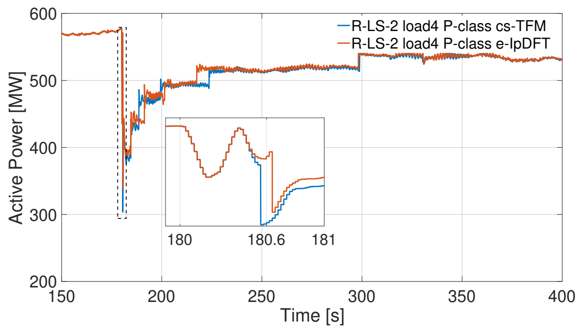

(d)

Figure 6.6 – PMU-based RoCoF measurements and corresponding active power profiles for R-LS-2 thresholds: (a) and (b) refer to load 16 and PMU M-class configuration, whereas (c) and (d) refer to load 4 and PMU P-class configuration.

amount of loads to be shed (refer to Figure 6.5a and Figure 6.6a). Concerning the load shedding results for R-LS-2, the difference between e-IpDFT and cs-TFM is less significant since the more conservative thresholds set in R-LS-2 make it more likely to trigger large amount of load shedding and lead to faster load shedding actions for both estimators.

Given the R-LS-1 and R-LS-2 thresholds for the PMU P-class configuration, Figure 6.5d shows that the e-IpDFT sheds a larger share of loads (+10%) than the cs-TFM and Figure 6.6d shows that the same amount of loads is shed by both cs-TFM and e-IpDFT. As shown in the zoomed windows, for both of the e-IpDFT and cs-TFM estimators, the load shedding is triggered earlier in P-class than in M-class configuration. This is due to the fact that, given the shorter observation interval of P-class PMUs, both estimators provide less accurate RoCoF measurements.

By extending the analysis to the entire grid, the performance evaluation of the considered RoCoF estimators can be characterized in terms of Expected Energy Not Served (*EENS*) and Integrated Frequency Variation (*IFV*). It is worth to note that the metric *EENS* has been defined in Chapter 5, Section 5.4. The same formula is adopted to compute the *EENS*. Since the load restoration is included for the studies conducted in this Chapter, the *EENS* is computed for the time interval between the start of load shedding and the end of load restoration. Here below the expression of *EENS* is recalled.

$$EENS = \sum_{t=t_0}^{t_{LR}} \sum_{l=1}^{L} \Delta P_{l,LS} \Delta t \tag{6.8}$$

where t_0 is the time when the load shedding started, t_{LR} is the time when the load restoration ended, and L is the total number of load buses. Regarding the metric IFV, it refers to the total integrated frequency deviation (absolute value) of all the load buses during the UFLS and LR actions, expressed as

$$IFV = \sum_{i}^{L} \sum_{t=t_0}^{t_{LR}} |f_{t,i} - f_0| \tag{6.9}$$

where $f_{t,i}$ is the frequency measured on load bus i at time t, and f_0 is the system nominal frequency.

Table 6.3 reports the *EENS* and *IFV* values in the simulated contingency scenarios. The comparison between the two threshold settings shows that R-LS-2 corresponds to higher *EENS* values than R-LS-1. As discussed in 6.3, the R-LS-2 thresholds are associated with lower RoCoF values and activation probability. Coherently, implementing R-LS-2 produces much higher *EENS* values. As regards IFV, although a higher LS share results in a reduction of the frequency decrease, it does not guarantee a lower *IFV*. This is because that an excessive amount of load shedding may cause a subsequent rapid frequency increase, not properly compensated by LR actions. An example of such phenomenon is shown in Figure 6.7, where

Table 6.3 – UFLS scheme performance in the simulated contingency scenarios.

Threshold	Estimator	Class	EENS [MWh]	IFV
R-LS-1	cs-TFM	M	14.05	1336.2
	e-IpDFT	M	16.70	1358.4
	cs-TFM	P	14.51	1329.3
	e-IpDFT	P	16.83	1373.1
R-LS-2	cs-TFM	M	14.21	1334.4
	e-IpDFT	M	24.17	1568.8
	cs-TFM	P	19.23	1383.2
	e-IpDFT	P	24.20	1458.9

the evolution of frequency measurements provided by the four PMU configurations in R-LS-1 and R-LS-2 are compared. The frequency overshoots are clearly visible in the zoomed window in Figure 6.7b.

6.6 Discussions and Conclusions

This Chapter investigated the impact of synchrophasor estimation algorithms in RoCoF-based UFLS schemes. To this end, a simple yet effective local UFLS and Load-Restoration scheme has been developed. The proposed dual scheme relies on PMU-based estimates of fundamental frequency and RoCoF. Specifically, two sets of RoCoF thresholds have been considered to promptly trigger the load shedding and suitably select the amount of shed loads. Frequency measurements, instead, are used in the load restoration process. In contrast to traditional approaches based on frequency thresholds, the proposed scheme employs RoCoF measurements to activate the load shedding action, as its derivative formulation allows for a prompter and more effective response to the fast dynamics experienced in modern power systems with a high share of non-synchronous renewable resources. In this respect, two PMU-based estimation RoCoF techniques are considered: the e-IpDFT and the cs-TFM, that rely on a static and a dynamic signal model, respectively. For each algorithm, two configurations, as representative of PMU P- and M-class as specialized by the IEEE Std C37.118.1, are considered.

The performance of the proposed relaying scheme is assessed by means of a real-time simulator, reproducing a full-replica of the time-domain dynamic model of the IEEE 39-bus power system with a substantial amount of wind generation. In the dedicated simulations, the contingency event of tripping 1.5 GW generation power is reproduced to evaluate the UFLS and LR performance for each combination of RoCoF thresholds and algorithm configurations. The *EENS* and the *IFV* are applied as performance metrics.

The comparison between the two synchrophasor estimation algorithms shows that the e-IpDFT always leads to higher *EENS* than the cs-TFM, for both P- and M-class configurations. As for the comparison between the PMU P- and M-class configurations, it is observed that the

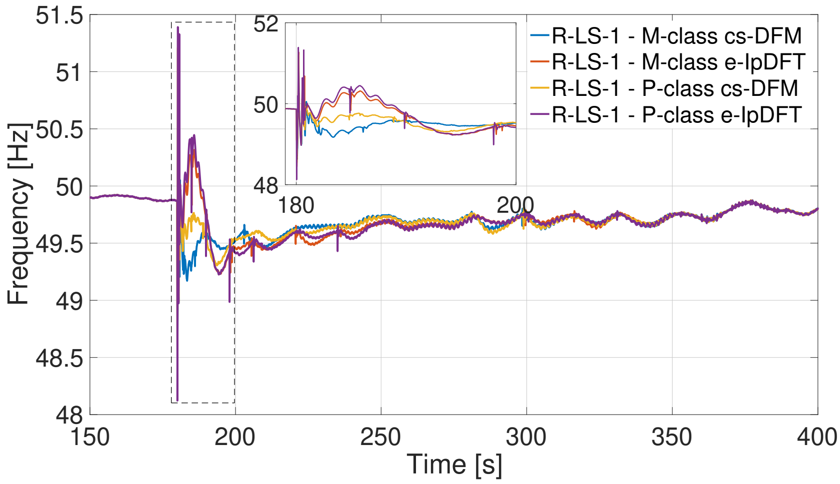

(a)

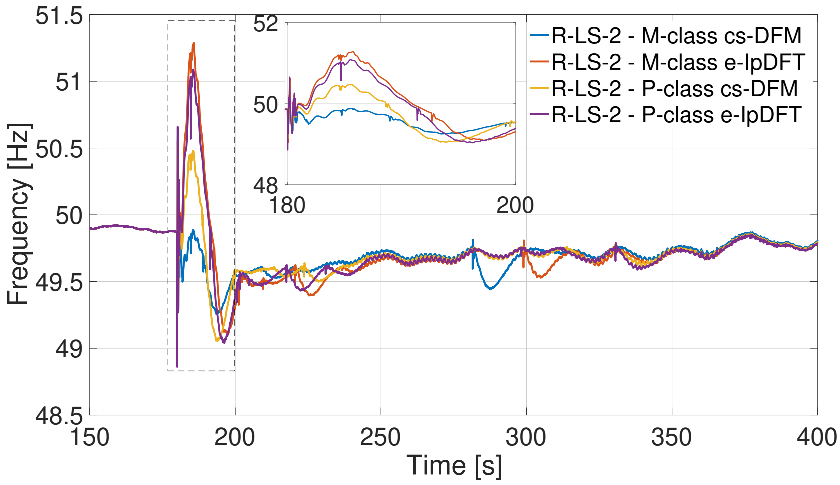

(b)

Figure 6.7 – Frequency: M-class cs-TFM (blue), M-class e-IpDFT (orange), P-class cs-TFM (yellow), P-class e-IpDFT (violet). Frequency for thresholds *R*-LS-1 (a); Frequency for thresholds *R*-LS-2 (b).

P-class one produces higher RoCoF estimations leading to higher *EENS* and IFV. In addition, the comparison between the two different sets of RoCoF thresholds exhibits the importance of a proper threshold setting, as high shares of shed loads might lead to an uncontrolled frequency increase and thus trigger too fast and excessive LR actions.

In conclusion, the obtained results confirmed the potential benefit of PMU-based RoCoF measurements for UFLS applications and demonstrated that the performance of the control scheme depends on the adopted synchrophasor estimation technique and configuration. From the proposed analysis, it is possible to deduce some practical recommendations. As PMU-based RoCoF measurements are algorithm-dependent, it is necessary to identify such estimation differences, which can have a significant impact on RoCoF-based applications under non-stationary operation conditions.

7 Conclusions

The Thesis has evaluated the dynamics of low-inertia power grids hosting large-scale BESSs, quantitatively assessed the benefit of converter-interfaced BESS with respect to the system frequency containment and validated and analyzed two proposed UFLS control strategies.

Specifically, the manuscript has analyzed the impact of converter-based BESS on the post-contingency dynamics of low-inertia grids that interfaces a mix of synchronous generation and CIG. The numerical results quantitatively proved that BESSs controlled as grid-forming or grid-following units can both assist in limiting the frequency decreasing and damping the grid frequency oscillations subsequent to contingencies, but also demonstrated the superiority of the grid forming converters to maintain the PCC voltage during electromechanical transients. In addition, a dedicated sensitivity analysis has quantified how the inertia constant of the grid-forming controllers positively influences the post-contingency frequency containment showing that the grid-forming controllers with high inertia constants can provide important containment to post-contingency RoCoF during electromechanical transients.

Then, the manuscript has assessed the performance of large-scale BESSs in enhancing the frequency containment in low-inertia power grids. Realistic and detailed one-day-long dynamic simulations have been carried out considering real stochastic wind generation and demand profiles, both inferred from high-resolution measurements. The proposed simulation framework and the performance metrics provided a benchmark setup to quantitatively compare the benefit of large-scale BESSs controlled as grid-forming vs. grid-following units in improving the system frequency containment considering a real operative scenario with realistic reserve margins. The numerical results quantitatively verified that the grid-forming outperforms grid-following control, achieving better system frequency containment and lower relative RoCoF. TSOs can potentially use the proposed frequency metrics relying on frequency measurements provided by PMUs to certify the performance of grid-forming units providing frequency containment in normal and emergency operating conditions.

The next aspect that has been treated in the manuscript is the proposition and evaluation of the performance of a centralized OPF-driven UFLS scheme specifically developed for low-inertia power systems hosting large-scale BESSs. Extensive numerical evaluations have demonstrated the high prediction fidelity of the presented OPF-driven UFLS method. The proposed method is capable to prevent cascading relay tripping caused by nodal voltages and branch current limits violations while minimizing the amount of load shed thanks to correctly predicting the post-contingency nodal voltages and branch currents magnitudes. Furthermore, the proposed OPF-driven UFLS approach can reduce the EENS by properly considering the post-contingency response of large-scale BESSs. On the contrary, the traditional UFLS do not take advantage of the presence of largescale BESS, being myopic to the presence of these assets. In this respect, the proposed centralized UFLS approach leveraging the system real-time situational awareness enabled by PMUs/RTUs can be easily coupled with other emergency control and protection schemes to enhance the performance of emergency operational practices of TSO control rooms.

Finally, the manuscript has presented an investigation on the impact of synchrophasor estimation algorithms on RoCoF-based UFLS schemes. To this end, effective local UFLS and load-restoration schemes have been developed. The proposed schemes rely on PMU-based estimates of fundamental frequency and RoCoF. In this respect, two consolidated PMU-based RoCoF estimation algorithms are considered: the e-IpDFT and the cs-TFM, which rely on a static and a dynamic signal model, respectively. Both P- and M-class PMUs, as specified by the standard Std C37.118.1., are considered for each algorithm. The obtained results confirmed the benefit of PMU-based RoCoF measurements for UFLS applications and demonstrated that the performance of the control scheme depends on the adopted synchrophasor estimation algorithms and PMUs class. Given the strategic interest of implementing RoCoF-based UFLS relays, it is necessary to properly consider the RoCoF estimates differences associated to the synchrophasor estimation algorithms to achieve consistent and desirable behavior of the corresponding RoCoF-based applications under non-stationary operation conditions.

A Dynamic Models of IEEE 39-bus Power Systems

List of Symbols

Synchronous Machine

F	friction factor, Newton per meter per second $[N \cdot m \cdot s]$
H	inertia constant, second $[s]$
R_s	stator resistance, per-unit [p.u.]
$T_{do}^{'}$	d-axis transient open-circuit time constant, second $[s]$
$T_{do}^{''}$	d-axis subtransient open-circuit time constant, second $[s]$
$T_{qo}^{'}$	q-axis transient open-circuit time constant, second $[s]$
$T_{qo}^{''}$	q-axis subtransient open-circuit time constant, second $[s]$
X_l	leakage reactance, per-unit [p.u.]
X_d	d-axis synchronous reactance, per-unit [p.u.]
$X_d^{'}$	d-axis transient reactance, per-unit [p.u.]
$X_d^{''}$	d-axis subtransient reactance, per-unit [p.u.]
X_q	q-axis synchronous reactance, per-unit [p.u.]
$X_q^{'}$	q-axis transient reactance, per-unit [p.u.]
$X_q^{''}$	q-axis subtransient reactance, per-unit [p.u.]

R_p static droop, percentage [%]

Hydraulic Turbine and Governor System

K_p regulator gain

K_i regulator integral gain

T_M mechanical inertia constant, second [s]

T_w water inertia time, second [s]

Steam Turbine and Governor System

F_2 turbine torque fraction 2

F_3 turbine torque fraction 3

F_4 turbine torque fraction 4

F_5 turbine torque fraction 5

K_p regulator gain

T_2 steam turbine time constant 2, second [s]

T_3 steam turbine time constant 3, second [s]

T_4 steam turbine time constant 4, second [s]

T_5 steam turbine time constant 5, second [s]

T_{sm} steam turbine servomotor time constant, second [s]

T_{sr} steam turbine speed delay, second [s]

Synchronous Machine Excitation System

K_a voltage regulator gain

K_f damping filter gain

T_a voltage regulator time constant, second [s]

T_b transient gain reduction lead time constant, second [s]

T_c transient gain reduction lag time constant, second [s]

T_f damping filter time constant, second [s]

T_r low-pass filter time constant, second [s]

Wind Power Plant

C_{dc} capacitance of DC capacitor for back-to-back converter, per-unit [p.u.]

L_{choke} inductance of AC reactor for back-to-back converter, per-unit [p.u.]

L_m mutual inductance of asynchronous machine, per-unit [p.u.]

L_r rotor inductance of asynchronous machine, per-unit [p.u.]

L_r rotor inductance of asynchronous machine, per-unit [p.u.]

L_s stator inductance of asynchronous machine, per-unit [p.u.]

R_{choke} resistance of AC reactor for back-to-back converter, per-unit [p.u.]

R_r rotor resistance of asynchronous machine, per-unit [p.u.]

R_s stator resistance of asynchronous machine, per-unit [p.u.]

Converter Electrical Elements

C_{dc} DC-link capacitance, per-unit [p.u.]

C_{dcf} capacitance of DC filter, per-unit [p.u.]

f_{T1}, f_{T2} AC filter tuning frequency, hertz $[Hz]$

L_{dcf} inductance of DC filter, per-unit [p.u.]

L_r inductance of AC reactor, per-unit [p.u.]

L_{sr} inductance of DC smooth reactor, per-unit [p.u.]

Q_{f1}, Q_{f2} AC filter nominal reactive power, volt-ampere reactive $[var]$

R_{dcf} resistance of DC filter, per-unit [p.u.]

R_r resistance of AC reactor, per-unit [p.u.]

R_{sr} resistance of DC smooth reactor, per-unit [p.u.]

V_n^{ac} nominal voltage at AC side of the converter, [kV]

V_n^{dc} nominal Voltage at DC side of the converter, [kV]

List of Abbreviations

AVR automatic voltage regulator

BESS battery energy storage system

DFIG doubly-fed induction generator

EMTP electromagnetic transmission program

IGBT insulated-gate bipolar transistor

PLL phase locked loop

PMU phasor mesurement unit

RMS root mean square

SOC state of charge

SSM state space model

TTC three-time constant

A.1 Synchronous Generators

The conventional generation asset of this power grid consists of both hydro- and thermal-power plants.They are simulated by means of a six-order state-space model for the synchronous machine, a prime mover [91], a DC1A excitation system associated with an AVR [96]. All the generator models include a primary frequency regulator with a static droop coefficient $R_p = 5\%$. Table A.1 summarizes the types of the adopted synchronous generators.

Table A.1 – Synchronous generators summary.

Generation	Type
G1	Thermal Plant
G2-G6, G8-G10	Hydro Plant
G7	Hydro Plant

A.1.1 Synchronous Machines

The generator model provided in the original technical report of the IEEE 39-bus benchmark system [85] is essentially a four-order generator model, as it does not include the subtransient circuits. Therefore, we adopt a different model. Specifically, we use a six-order state-space model for the synchronous machine, whose synchronous and transient parameters (R_s, X_l, X_d, X_q, $X_d^{'}$, $X_q^{'}$, $T_{d0}^{'}$, $T_{q0}^{'}$) are taken from the original technical report [85], while the subtransient parameters ($X_d^{''}$, $X_q^{''}$, T_{d0}'', $T_{q0}^{''}$) are inspired from real-world test parameters, adapted from the IEEE Std. 1110™-2002(R2007) [88] and the EPRI technical reports [89, 90].

In [85], the per unit values are given with respect to the base power of 100 MW, whereas in Table A.2 we select the base power according to the IEEE Std. 115-1995 [153]:

$$Z_{base} = \frac{E_N^2}{S_N}$$

where E_N is the stator nominal line-to-line voltage and S_N is the three-phase apparent power of the the machine.

Table A.2 – Parameters for synchronous machines.

Unit		G1	G2	G3	G4	G5	G6	G7	G8	G9	G10
Capacity [MVA]		3000	1000	1000	1000	520	1000	1000	1000	1000	1000
Nominal Voltage [kV]		22	22	22	22	22	22	22	22	22	22
Synchronous Machine	H [s]	16.7	3.03	3.58	2.86	5.2	3.48	2.64	2.43	3.45	4.2
	Rs [p.u.]	0	0	0	0	0	0.006	0	0.001	0	0
	Xl [p.u.]	0.09	0.35	0.3	0.3	0.28	0.022	0.32	0.28	0.3	0.13
	Xd [p.u.]	0.6	2.95	2.5	2.62	3.48	2.54	2.95	2.90	2.1	1
	Xq [p.u.]	0.57	2.82	2.37	2.58	3.224	2.41	2.62	2.80	2.05	0.69
	X'd [p.u.]	0.18	0.7	0.53	0.44	0.686	0.5	0.49	0.57	0.57	0.31
	X'q [p.u.]	0.24	1.7	0.88	1.66	0.8632	0.81	1.86	0.91	0.59	0.4
	X"d [p.u.]	0.12	0.367	0.287	0.321	0.215	0.419	0.31	0.354	0.306	0.359/
	X"q [p.u.]	0.12	0.359	0.33	0.411	0.213	0.471	0.403	0.228	0.306	0.383
	T'do [s]	7	6.56	5.7	5.69	5.4	7.3	5.66	6.7	4.79	10.2
	T'qo [s]	0.7	1.5	1.5	1.5	1.5	0.4	1.5	1.5	1.96	0.2
	T"do [s]	0.029	0.041	0.041	0.07	0.031	0.008	0.007	0.021	0.04	0.052
	T"qo [s]	0.053	0.065	0.065	0.019	0.019	0.019	0.053	0.019	0.062	0.35

A.1.2 Turbine-governors

Hydraulic turbine and governor system

As shown in Figure A.1, the commonly-used standard hydro turbine governor model illustrated in [93, 154] is adopted. It consists of a PI governor, a servomotor, and a non-linear turbine-water column model that accounts for the effects of varying flow on the effective water starting time. Parameters $k_{p,gov}$ and $k_{i,gov}$ are the proportional and integral gains of the PI governor, k_a and T_a are the gain and time constant of the servomotor. According to [94], the response of the turbine governing system should be tuned to match the rotating inertia, the water column inertia, the turbine control servomotor timing and the characteristics of the connected electrical load. Therefore, as recommended in [94], we use:

$$\begin{aligned} T_M &= 2H \\ T_M : T_w &= 3:1 \end{aligned}$$

where, H is the generator inertia constant, T_M is the mechanical inertia constant, and T_W is water inertia time (also known as "water starting time"). The PI governor parameters are derived according to [95]:

$$\begin{aligned} 1/K_P &= 0.625 T_W / H \\ K_P / K_I &= 3.33 T_W \end{aligned}$$

Accordingly, the parameters for the hydraulic turbine and PI regulator are given in Table A.3.

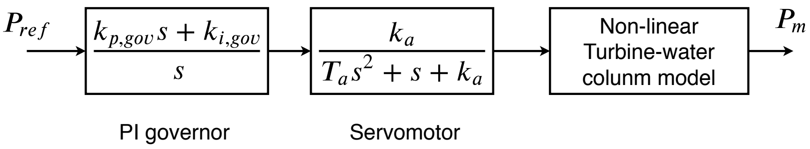

Figure A.1 – Diagram of the hydro-turbine governing system.

Table A.3 – Parameters for hydro turbine-governors.

Unit	Hydraulic Turbine		PI Regulator		Servo-motor	
	T_M [s]	T_W [s]	$K_{p,gov}$	$K_{i,gov}$	K_a	T_a
G2	6.06	2.02	2.4	0.36	1	0.2
G3	7.16	2.39	2.4	0.30	1	0.2
G4	5.72	1.90	2.4	0.38	1	0.2
G5	10.4	3.47	2.4	0.21	1	0.2
G6	6.96	2.32	2.4	0.31	1	0.2
G7	5.28	1.76	2.4	0.41	1	0.2
G8	4.86	1.62	2.4	0.4	1	0.2
G9	6.90	2.30	2.4	0.31	1	0.2
G10	8.40	2.80	2.4	0.26	1	0.2

Steam turbine and governor system

The steam turbine and governor model are adapted from [91], where the steam turbine system is presented as tandem-compound, single mass model and the speed governor consists of a proportional regulator, a speed delay and a servo motor controlling the gate opening. The parameters for the steam turbine-governor are taken from the typical values used, for instance, in [91, 92]. The parameters for the steam turbine and the speed governor is given in Table A.4.

A.1.3 Excitation Systems

The excitation system implements the IEEE DC type 1 exciter associated with an AVR [96]. The parameters are adapted from the IEEE task force technical report [86] and are provided in Table A.5.

Table A.4 – Parameters for the steam turbine-governor.

Unit	Steam Turbine								Speed Governor		
	T2 [s]	T3 [s]	T4 [s]	T5 [s]	F2	F3	F4	F5	K_p	T_{sr} [s]	T_{sm} [s]
G1	0	0.5	7	0.3	0	0.36	0.36	0.28	1	0.1	0.3

Table A.5 – Parameters for excitation systems.

Unit		G1	G2	G3	G4	G5	G6	G7	G8	G9	G10
Exciter	T_r [s]	0.01	0.01	0.01	0.01	0.01	0.01	0.01	0.01	0.01	0.01
	K_a	200	200	200	200	200	200	200	200	200	200
	T_a [s]	0.015	0.015	0.015	0.015	0.015	0.015	0.015	0.015	0.015	0.015
	T_b [s]	10	10	10	10	10	10	10	10	10	10
	T_c [s]	1	1	1	1	1	1	1	1	1	1
	K_f	0.001	0.001	0.001	0.001	0.001	0.001	0.001	0.001	0.001	0.001
	T_f [s]	0.1	0.1	0.1	0.1	0.1	0.1	0.1	0.1	0.1	0.1

A.2 Dynamic Loads

In order to reproduce a plausible dynamic load behavior, a EPRI LOADSYN model has been used [100]. Specifically, the load response to voltage and frequency variations is modeled according to the following time-domain functions:

$$P(t) = P_0(t)\left(\frac{V(t)}{V_0}\right)^{K_{pv}}[1+K_{pf}(f(t)-f_0)] \tag{A.1}$$

$$Q(t) = Q_0(t)\left(\frac{V(t)}{V_0}\right)^{K_{qv}}[1+K_{qf}(f(t)-f_0)] \tag{A.2}$$

where $P(t)$ and $Q(t)$ are the total three-phase load active and reactive power. The parameters K_{pv}, K_{pf}, K_{qv}, K_{qf} are obtained from typical load voltage and frequency parameters inferred from EPRI LOADSYN program [100]. In this regard, we represent $f(t)$, $V(t)$, $P_0(t)$, and $Q_0(t)$ as time-varying variables sampled with a resolution of 20 ms. We assume that $P_0(t)$ and $Q_0(t)$ are active and reactive power profiles at the rated frequency and voltage (i.e., 50 Hz and 345 kV). These demand profiles are derived from a monitoring system based on PMUs installed on the 125 kV sub-transmission system of the city of Lausanne, Switzerland [155]. Coherently with the other model variables, the measured time-series power data are sampled with a resolution of 20 ms. Since the nominal load values in the original IEEE 39-Bus power system are different from our measured data, the implemented time series of the nominal demand profiles (i.e., produce $P_0(t)$ and $Q_0(t)$) are obtained by re-scaling the measured time series.

The implementation of the EPRI LOADSYN model is illustrated in Figure A.2. A PLL and a RMS operator measure the bus frequency and voltage feeding the dynamic load model. In order to smooth the response of the PLL in transient conditions, a moving average operator is implemented. Specifically, the PLL-tracked frequency is updated every 1 ms, and then buffered for averaging. The overall buffer size is 240 samples, with an overlap size of 220 samples (i.e., the final frequency $f(t)$ is reported every 20 ms). On the other side, the bus voltage $V(t)$ is given by a RMS operator reporting every 20 ms. The RMS value is computed over a window length of 240 ms, as to be consistent with the frequency estimation. The voltage waveform used to feed the dynamic load model is the one at phase "a". The Load coefficients

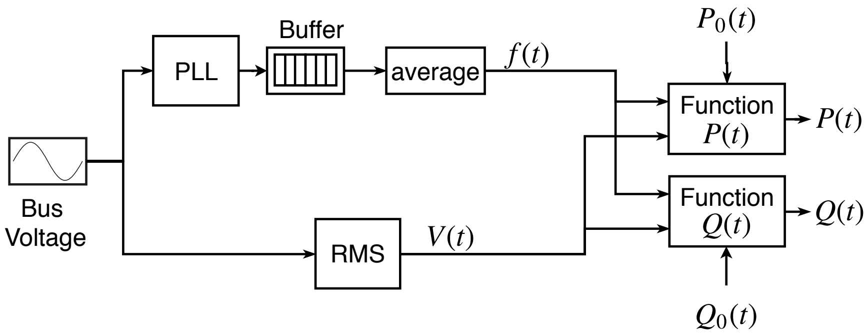

Figure A.2 – Diagram of the EPRI LOADSYN dynamic load model.

used in (A.2) are listed in Table A.6.

A.3 Transmission Lines and Transformers

The transmission line model is a ARTEMiS distributed parameter line with lumped losses [156]. The model is based on Bergeron's travelling wave method used by EMTP-RV [157]. The ARTEMiS distributed parameters line block is optimized for discrete real-time simulation and allows network decoupling. In Table A.7, the positive and zero-sequence resistance (R_1, R_0), inductance (L_1, L_0) and capacitance (C_1, C_0) are reported in per length (i.e. Ω/km, H/km, and F/km). It is worth to note that, the absolute value for the inductance and capacitance is computed from the per unit value provided in the original technical report [85] while using 50 Hz as base frequency.

Note about the transmission line: the IEEE 39-bus standard does not specify line length, therefore we choose some line length to obtain propagation speed just below the speed of light. The parameters of line 5-6 are different from those in the original New England 39-bus power grid due to constraints on the Artemis distributed parameter line for real-time simulation. Original parameters for line 5-6 are: $r_1 = 0.238\ \Omega$, $L_1 = 0.00821\ H$, $C_1 = 9.67 * 10^{-8}\ F$.

The three-phase transformers are modeled via suitably-connected single-phase transformers, which take into account the winding resistance (R_1, R_2) and leakage inductance (L_1, L_2), as well as the magnetization characteristics of the core, modeled by a linear (Rm, Lm) branch. As shown in Table A.8, in Config. II and Config. III, when replacing 4 synchronous generations with 4 wind plants, the transformers are modified accordingly. The Table reports the values in per unit with respect to each transformer's base power.

Table A.6 – Load buses and load coefficients

Load #	Bus #	kpf	kqf	kpv	kqv
1	3	1	-1.5	1.7	2.5
2	4	1.2	-1.6	0.5	2.5
3	7	1.5	-1.1	0.6	2.5
4	8	1	-1.7	1.7	2.6
5	12	0.9	-1.8	1.5	2.5
6	15	1	-1.5	1.7	2.5
7	16	0.7	-1.9	1.6	3.1
8	18	0.9	-1.3	1.5	2.8
9	20	1.3	-1.9	0.7	2.5
10	21	1	-1.7	1.7	2.6
11	23	0.8	-1.7	1.5	3
12	24	1.7	-0.9	1.5	2.5
13	25	0.9	-1.8	1.5	2.5
14	26	0.8	-1.6	1.6	2.9
15	27	1.5	-1.1	0.6	2.5
16	28	1.2	-1.6	0.5	2.5
17	29	1.3	-1.9	0.7	2.5
18	31	1	-1.7	1.7	2.6
19	39	0.8	-2.3	1.1	2.6

A.4 Wind Power Plants

A.4.1 Model of the Type-III DFIG Wind Turbine

The wind power plants are modeled as proposed in [97]. In particular, the power output is approximated by scaling up a detailed model of a single type-III wind turbine to match the total nominal capacity of the whole wind farm. The diagram of the overall system in shown in Figure A.3. Each wind generator model consists of a DFIG with an averaged back-to-back converter model [98]. For this analysis, the detailed aerodynamic model of wind turbine is not involved, as its effect is accounted already in the wind profiles.

The back-to-back voltage source converters are modeled as equivalent voltage sources. In this average converter model, the dynamics resulting from the interaction between the control system and the power system are preserved. As shown in Figure A.3, two grid-following controls are implemented in the back-to-back converters. The rotor-side converter controls active and reactive power through rotor current regulation whilist the stator-side converter regulates DC bus voltage and permits operation at a constant power factor (i.e., zero reactive power).

Details of the 4 wind power plants installed in Config. II and Config. III are give in Table A.9, including the locations, generation capacities and parameters for the asynchronous machines

Table A.7 – Parameters for transmission lines.

		Line Data						
From Bus	To Bus	Length [km]	R_1 [Ω/km]	R_0 [Ω/km]	L_1 [H/km]	L_0 [H/km]	C_1 [F/km]	C_0 [F/km]
1	2	134	0.0311	0.1243	0.0010	0.0029	1.164	0.5280
1	39	105	0.0113	0.0453	0.0008	0.0023	1.590	0.7240
2	3	49	0.0316	0.1263	0.0010	0.0029	1.169	0.5330
2	25	28	0.2975	1.1893	0.0010	0.0029	1.161	0.5290
3	4	53	0.0292	0.1166	0.0013	0.0039	0.9302	0.4266
3	18	42	0.0312	0.1247	0.0010	0.0030	1.133	0.5170
4	5	32.5	0.0293	0.1172	0.0012	0.0037	0.9200	0.4185
4	14	33	0.0288	0.1154	0.0012	0.0037	0.9333	0.4242
5	6	14	0.0340	0.1360	0.0010	0.0029	1.157	0.5290
5	8	32	0.0297	0.1190	0.0011	0.0033	1.028	0.4690
6	7	25.5	0.0280	0.1120	0.0011	0.0034	0.9882	0.4471
6	11	26.5	0.0314	0.1258	0.0010	0.0029	1.170	0.5320
7	8	15	0.0317	0.1269	0.0010	0.0029	1.160	0.5270
8	9	93	0.0294	0.1177	0.0012	0.0037	0.9118	0.4140
9	39	136	0.0087	0.0350	0.0006	0.0017	1.966	0.8940
10	11	14	0.0340	0.1360	0.0010	0.0029	1.157	0.5290
10	13	14	0.0340	0.1360	0.0010	0.0029	1.157	0.5290
13	14	32	0.0335	0.1339	0.0010	0.0030	1.200	0.5470
14	15	70	0.0306	0.1224	0.0010	0.0029	1.166	0.5300
15	16	31.5	0.0340	0.1360	0.0010	0.0028	1.210	0.5490
16	17	26	0.0320	0.1281	0.0011	0.0032	1.150	0.5230
16	19	61	0.0321	0.1249	0.0010	0.0030	1.110	0.5050
16	21	46	0.0207	0.0828	0.0009	0.0028	1.235	0.5610
16	24	15	0.0238	0.0952	0.0013	0.0037	1.013	0.4600
21	22	47	0.0203	0.0810	0.0090	0.0028	1.217	0.5530
22	23	33	0.0216	0.0866	0.0009	0.0028	1.245	0.5670
23	24	88	0.0298	0.1190	0.0013	0.0038	0.9148	0.4148
25	26	101	0.0377	0.1508	0.0010	0.0030	1.132	0.5150
26	27	46.5	0.0358	0.1433	0.0010	0.0030	1.148	0.5230
26	28	151	0.0339	0.1356	0.0010	0.0030	1.152	0.5240
26	29	200	0.0339	0.1357	0.0010	0.0030	1.146	0.5220
28	29	48	0.0347	0.1389	0.0010	0.0030	1.156	0.5250
							$*10^{-8}$	

Table A.8 – Parameters for transformers.

		Transformer				
From Bus	To Bus	Connection	Capacity $[MVA]$	R_1 R_2 [p.u.]	L_1 L_2 [p.u.]	Rm Lm [p.u.] [p.u.]
2	30	Dy11	1419	0 0	0.1284 0.1284	500 500
6	31	Dy11	1000	0 0	0.125 0.125	500 500
10	32	Dy11	1000	0 0	0.1 0.1	500 500
12	11	Dy11	110	0.0009 0.0009	0.0239 0.0239	500 500
12	13	Dy11	110	0.0009 0.0009	0.0239 0.0239	500 500
19	20	Dy11	880	0.0031 0.0031	0.0607 0.0607	500 500
19	33	Dy11	1000	0.0035 0.0035	0.0710 0.0710	500 500
20	34	Dy11	572	0.0026 0.0026	0.0515 0.0515	500 500
20	WP4	Dy11	750	0 0	0.0570 0.0750	500 500
22	35	Dy11	1000	0 0	0.0715 0.0715	500 500
23	36	Dy11	1000	0.0025 0.0025	0.1360 0.1360	500 500
25	37	Dy11	1000	0.0030 0.0030	0.1160 0.1160	500 500
25	WP2	Dy11	1200	30 30	0.1160 0.1160	500 500
29	38	Dy11	935	0.0037 0.0037	0.0729 0.0729	500 500
29	WP3	Dy11	1000	0 0	0.1000 0.1000	500 500
39	39G	Dy11	3000	0 0	0.3 0.3	500 500
39	WP1	Dy11	2000	0 0	0.1800 0.1800	500 500

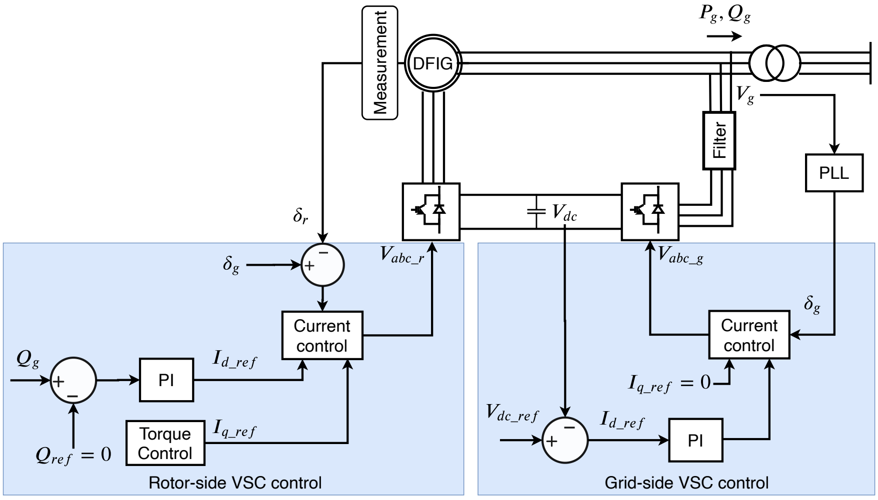

Figure A.3 – Diagram of wind power plant and controls.

Table A.9 – Parameters of the wind plants.

Unit	Type	Bus	Capacity [MVA]	Asynchronous Machine [p.u.]					Back-to-back Converter		
				Rs	Ls	Rr	Lr	Lm	R_{choke} [p.u.]	L_{choke} [p.u.]	C_{dc} [p.u.]
WP1	Type-III	39	1600	0.00706	0.171	0.005	0.156	2.9	0.003	0.3	3.1
WP2	Type-III	37	1300	0.00706	0.171	0.005	0.156	2.9	0.003	0.3	3.1
WP3	Type-III	38	900	0.00706	0.171	0.005	0.156	2.9	0.003	0.3	3.1
WP4	Type-III	34	700	0.00706	0.171	0.005	0.156	2.9	0.003	0.3	3.1

and back-to-back converters. The parameters in per unit are given by referring their own capacity as base power .

A.5 Converter-interfaced Battery Energy Storage System

A detailed model of a BESS is installed at bus 17 in the low-inertia 39-bus power system. As detailed below, it consists of the battery cell stack (necessary to model voltage dynamics on the converter DC bus), and the power converter, which is modelled at the level of the switching devices. figure A.4 presents a simplified diagram of the converter-interfaced BESS. Parameters for electrical elements at AC and DC side of the converter are listed in Table. A.10, where the per unit value are given with respect to their own system bases.

A.5.1 Battery Cell Stack

The voltage at the terminal of a battery is generally dynamic and it depends on the output current, state-of-charge, cells temperature, ageing conditions, and C-rate. In control applications, it is typically modelled with electric equivalent circuits, which trade detailed modelling

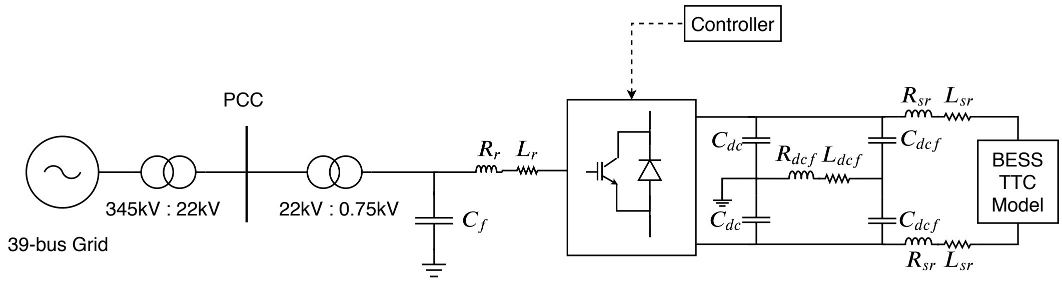

Figure A.4 – Diagram of converter-interfaced BESS.

Table A.10 – Parameters for electrical elements at AC and DC side.

Unit	Capacity [MVA]	DC							AC		
		V_n^{dc} [kV]	R_{sr} [p.u.]	L_{sr} [p.u.]	R_{dcf} [p.u.]	C_{dcf} [p.u.]	L_{dcf} [p.u.]	C_{dc} [p.u.]	V_n^{ac} [kV]	R_r [p.u.]	L_r [p.u.]
Converter	225	1.5	1.25×10^{-4}	0.05	7.19×10^{-4}	0.754	7.32×10^{-5}	4.32	0.75	0.005	0.15

of the electrochemical reactions for increased tractability, see e.g. [158, 159]. We adopt a grey-box model identified from measurements of a 720 kVA/560 kWh Lithium-titanate-oxide battery at EPFL [101]. The model is a third-order model with parameters that depend on the state-of-charge. Despite most of literature refers to two-time-constant models (i.e., second order models), it was shown in [101] that when considering voltage measurements at a second resolution, a third state is necessary to explain system dynamics. figure A.5 shows the three-time constant (TTC) equivalent circuit of the battery cell stack. The state-space representation of the model is:

$$\dot{x}(t) = Ax(t) + Bu(t) \tag{A.3}$$

$$y(t) = Cx(t) + Du(t) \tag{A.4}$$

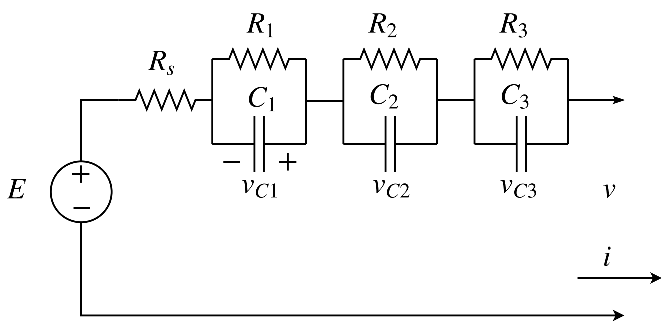

Figure A.5 – Three time constant equivalent circuit.

where

$$A = \begin{bmatrix} -\frac{1}{R_1C_1} & 0 & 0 \\ 0 & -\frac{1}{R_2C_2} & 0 \\ 0 & 0 & -\frac{1}{R_3C_3} \end{bmatrix} \tag{A.5}$$

$$B = \begin{bmatrix} 1/C_1 & 0 \\ 1/C_2 & 0 \\ 1/C_3 & 0 \end{bmatrix}, C = \begin{bmatrix} 1 & 1 & 1 \end{bmatrix}, D = \begin{bmatrix} R_s & E \end{bmatrix} \tag{A.6}$$

$$x = \begin{bmatrix} v_{C1} & v_{C2} & v_{C3} \end{bmatrix},\ u(t) = \begin{bmatrix} i & 1 \end{bmatrix}^T. \tag{A.7}$$

Model output $y(t)$ denotes the terminal voltage, and input i is the total DC current absorbed/provided by the battery. The elements of matrices A, B, and D are state-of-charge-dependent and can be identified from measurements, as described in [101, 102].

The large-scale BESS model (noted as $BESS_{aggre}$) implemented in the low-inertia 39-bus power system is developed on the basis of a TTC model whose parameters have been identified using real data from the 720kVA/560kWh BESS (noted as $BESS_{desl}$) available at EPFL-DESL [101]. The identified $BESS_{desl}$ parameters are shown in Table A.11. Since the power rating of the BESS that we use in this work (225 MVA) is larger than the nominal power of $BESS_{desl}$ (0.72MVA), the BESS model is scaled up and the parameters are adapted as described in the following.

First, the target power (225MVA) is achieved with a configuration considering 156 BESS connected on the same AC bus and each BESS composed by two cell stacks in series. Each cell stack connected in series is identical to the battery system at EPFL-DESL (i.e., $BESS_{desl}$). The two units are connected in series in order to increase the voltage on the DC bus. Considering that power electronic converters can conveniently handle voltage up to 2 kV and the open-circuit voltage of the original model [101] is 800 V at full charge, we consider that two units in series respects the most suitable configuration. Figure A.6 shows the configuration of the $BESS_{aggre}$, where the nominal DC voltage of the connected inverter is 1.5 kV. As batteries, converters and their controls are all considered identical, therefore they have been replaced by this equivalent model (see in Figure A.4), where all of the 156 stacks are connected in parallel on the same DC bus, interfaced with the AC grid through a single equivalent converter. The nominal power capacity and energy capacity of the modeled $BESS_{aggre}$ are 225 MVA and 176 MWh, respectively. The parameters of the $BESS_{aggre}$ TCC model is presented in the following.

By assuming that all the paralleled battery packs are identical, the voltage of the aggregated BESS is considered equal to the voltage of each battery pack. The parameters of the equivalent circuit models are obtained by doubling all the parameters reported in [101], except for capacitors, whose values were halved to retain the same time constants as those identified. Final parameters adopted for three-time constant model (A.4)-(A.7) are reported in in Table A.12. The arrows in the table imply that theses values vary linearly with the SOC in the indicated

Table A.11 – Parameters of 560 kWh Lithium Titanate Oxide BESS available at EPFL-DESL.

SOC [%]	**0-20**	**20-40**	**40-60**	**60-80**	**80-100**
E $[V]$	592.2	625.0	652.9	680.2	733.2
R_s $[\Omega]$	0.029	0.021	0.015	0.014	0.013
R_1 $[\Omega]$	0.095	0.075	0.090	0.079	0.199
C_1 $[F]$	8930	9809	13996	12000	11234
R_2 $[\Omega]$	0.04	0.009	0.009	0.009	0.10
C_2 $[F]$	909	2139	2482	2490	2505
R_3 $[\Omega]$	2.5e-3	4.9e-5	2.4e-4	6.8e-4	6.0e-4
C_3 $[F]$	544.2	789.0	2959.7	4500	6177.3

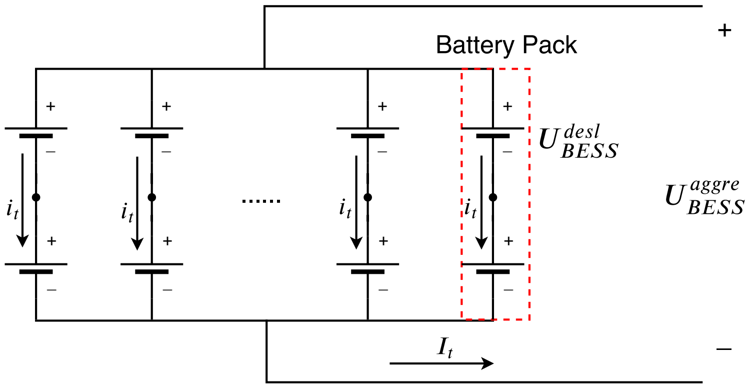

Figure A.6 – Configuration of the $BESS_{aggre}$.

Table A.12 – Parameters of the BESS connected to the HV transmission grid.

SOC[%]	**10→30**	**30→50**	**50→70**	**70→90**
E $[V]$	1184.4 → 1250.0	1250.0 → 1305.8	1305.8 → 1360.4	1360.4 → 1466.4
R_s $[\Omega]$	0.052 → 0.042	0.042 → 0.030	0.030 → 0.028	0.028 → 0.026
R_1 $[\Omega]$	0.190 → 0.150	0.150 → 0.180	0.180 → 0.158	0.158 → 0.398
C_1 $[F]$	4465.0 → 4904.5	4904.5 → 6998.0	6998.0 → 6000.0	6000.0 → 5617.0
R_2 $[\Omega]$	0.080 → 0.018	0.018 → 0.018	0.018 → 0.018	0.018 → 0.020
C_2 $[F]$	454.50 → 1069.5	1069.5 → 1241.0	1241.0 → 1245.0	1245.0 → 1252.5
R_3 $[\Omega]$	5.0e-3 → 9.8e-5	9.8e-5 → 4.8e-4	4.80e-4 → 13.6e-4	13.6e-4 → 12.0e-4
C_3 $[F]$	272.10 → 394.50	394.50 → 1479.8	1479.8 → 2250.0	2250.0 → 3088.7

range. The total BESS current $i_k = 156 \times i_{t,k}$ is used to compute the state-of-charge:

$$\mathrm{SOC}_{k+1} = \mathrm{SOC}_k + \frac{Ts}{3600}\frac{i_k}{C_{nom}} \tag{A.8}$$

where $T_s = 0.001$ s is the sampling time , C_{nom} =117 kAh is the BESS capacity, and $i_{t,k}$ is the current of each parallel battery pack at time k .

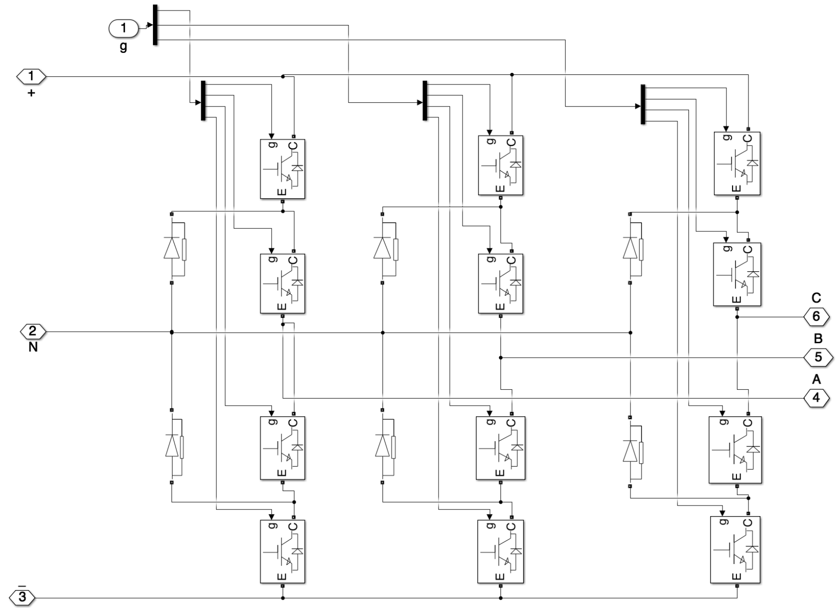

Figure A.7 – IGBT-based 3-level converter.

A.5.2 Three-level NPC Converter

The BESS is integrated into the IEEE 39-bus through an aggregated fully modeled three-level neutral-point clamped (NPC) converter. figure A.7 shows the original Simulink model of the 3-level converter, which can not be directly implemented in the real-time simulation model due to the fact that it involves too many switching devices in one state space nodal (SSN) group [160]. The solution is to distribute those switch devices into different SSN groups as shown in Figure A.8. The three bridge arms (one arm refers to the red rectangle in Figure A.7) of the 3-level converter are respectively included into subsystem "3-level NPC 1", "3-level NPC 2 " and "3-level NPC 3". Each arm interface with AC and DC side through two ARTMiS-SSN interfance blocks that are used to define nodes and groups of SSN solver.

A.5.3 Converter Controls

As the adopted converter controls have been described in Section. 3.3, the values of those parameters used in the converter controls that applied are listed in Table. A.13.

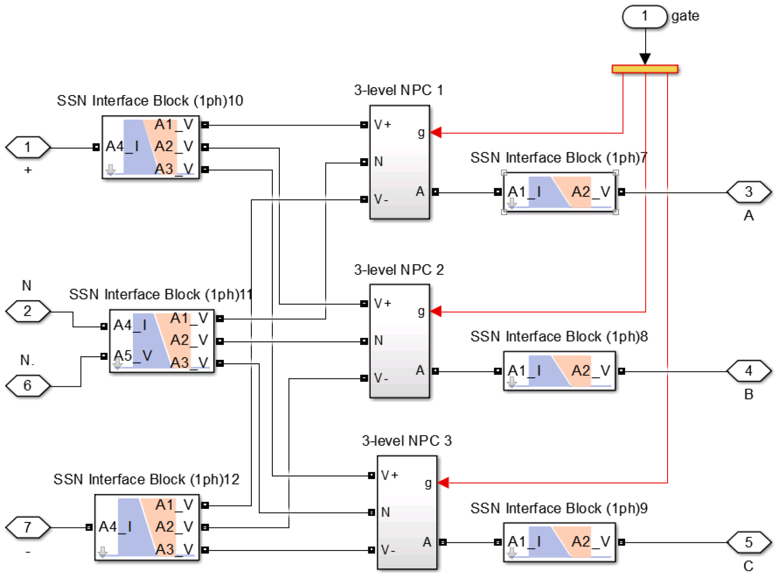

Figure A.8 – IGBT-based 3-level converter model in RT simulation.

Table A.13 – List of parameters values used in the grid-forming and grid-following controls.

<table>
<tr><th colspan="2">Grid-forming dontrol with doupled functionalities</th><th colspan="2">Grid-forming control with decoupled functionalities</th><th colspan="2">Grid-following control in grid-supporting mode</th></tr>
<tr><td>m_p</td><td>5%</td><td>m_p</td><td>5%</td><td>$k^{grid-following}_{f-p}$ [MW/Hz]</td><td>90</td></tr>
<tr><td rowspan="2">n_q [V/Mvar]</td><td rowspan="2">0.33</td><td rowspan="2">n_q [V/Mvar]</td><td rowspan="2">0.33</td><td>$k^{grid-following}_{v-q}$ [MVar/V]</td><td>1.5</td></tr>
<tr><td>ΔV_{tr} [p.u.]</td><td>±0.005</td></tr>
<tr><td>ω_{LP} [rad/s]</td><td>31.4</td><td>H_{GFM} [s]</td><td>0.3185</td><td>ω_{LF} [rad/s]</td><td>157</td></tr>
<tr><td>T_1 [s]</td><td>0.0333</td><td rowspan="2">k_p</td><td rowspan="2">0.02</td><td>$k_{p,pll}$</td><td>60</td></tr>
<tr><td>T_2 [s]</td><td>0.0111</td><td>$k_{i,pll}$</td><td>1400</td></tr>
</table>

Bibliography

[1] CAISO, "Frequency response phase 2," California ISO, Tech. Rep., Dec. 2016.

[2] AEMO, "Renewable integration study: Stage 1 report - enabling secure operation of the nem with very high penetrations of renewable energy," Australian Energy Market Operator, Tech. Rep., April 2020.

[3] B. Dunn, H. Kamath, and J.-M. Tarascon, "Electrical energy storage for the grid: A battery of choices," *Science*, vol. 334, no. 6058, pp. 928–935, 2011.

[4] W. J. Cole and A. Frazier, "Cost projections for utility-scale battery storage," National Renewable Energy Lab.(NREL), Golden, CO (United States), Tech. Rep., 2019.

[5] A. Reza Reisi, M. Hassan Moradi, and S. Jamasb, "Classification and comparison of maximum power point tracking techniques for photovoltaic system: A review," *Renewable and Sustainable Energy Reviews*, vol. 19, pp. 433–443, 2013.

[6] J. A. Baroudi, V. Dinavahi, and A. M. Knight, "A review of power converter topologies for wind generators," *Renewable Energy*, vol. 32, no. 14, pp. 2369 – 2385, 2007.

[7] J. Beerten, O. Gomis-Bellmunt, X. Guillaud, J. Rimez, A. van der Meer, and D. Van Hertem, "Modeling and control of hvdc grids: A key challenge for the future power system," in *2014 Power Systems Computation Conference*, Aug 2014, pp. 1–21.

[8] B. Kroposki, B. Johnson, Y. Zhang, V. Gevorgian, P. Denholm, B.-M. Hodge, and B. Hannegan, "Achieving a 100% renewable grid: Operating electric power systems with extremely high levels of variable renewable energy," *IEEE Power and Energy Magazine*, vol. 15, no. 2, pp. 61–73, 2017.

[9] G. Denis, T. Prevost, P. Panciatici, X. Kestelyn, F. Colas, and X. Guillaud, "Review on potential strategies for transmission grid operations based on power electronics interfaced voltage sources," in *2015 IEEE Power Energy Society General Meeting*, 2015, pp. 1–5.

[10] Agora Energiewende and EMBER, "The european power sector in 2020: Up-to-date analysis on the electricity transition," Tech. Rep., January 2021.

[11] Y. Sun, S. V. Wachche, A. Mills, and O. Ma, "2018 renewable energy grid integration data book," National Renewable Energy Lab.(NREL), Golden, CO (United States), Tech. Rep., 2020.

[12] AEMO, "Renewable integration study: Stage 1 report appendix b:frequency control," Australian Energy Market Operator, Tech. Rep., March 2020.

[13] E. Ørum, M. Kuivaniemi, M. Laasonen, A. I. Bruseth, E. A. Jansson, A. Danell, K. Elkington, and N. Modig, "Future system inertia," *ENTSOE, Brussels, Tech. Rep*, pp. 1–58, 2015.

[14] N. Modig, R. Eriksson, L. Haarla, P. Ruokolainen, M. Kuivaniemi, K. Hornnes, P. Vada, S. Meybodi, and D. Karlsson, "Technical requirements for fast frequency reserve provision in the nordic synchronous area," ENTSO-E, Inertia 2020 Working Group, Tech. Rep., 2019.

[15] E. Rehman, M. Miller, J. Schmall, and S. Huang, "Dynamic stability assessment of high penetration of renewable generation in the ercot grid," ERCOT, Austin, Tx, Tech. Rep., 2018.

[16] AEMO, "Inertia requirements methodology: Inertia requirements and shortfalls," Operational Analysis and Engineering, AEMO, Tech. Rep.

[17] N. Miller, D. Lew, and R. Piwko, "Technology capabilities for fast frequency response," *GE Energy Consulting, Tech. Rep*, vol. 3, pp. 10–60, 2017.

[18] AEMO, "Initial operation of the hornsdale power reserve battery energy storage system," 2018.

[19] VISTRA Energy, "2018 annual sustainability report," Tech. Rep., 2018.

[20] ERCOT, "Development of energy storage resources and distribution generation resources in ercot," October 2020, Accessed on: 11/8/2021. [Online]. Available: http://www.ercot.com/content/wcm/lists/215407/ESRs_and_DGRs_FINAL_10-13-20.pdf

[21] AEMO, "Review of the black system south australia report – system event of 28 september 2016," Australian Energy Market Operator, Tech. Rep., March 2017.

[22] ERCOT, "Inertia:basic concepts and impact on the ercot grid," Electricity Reliability Council of Texas, Tech. Rep.

[23] EirGrid and SONI, "Ensuring a secure, reliable and efficient power system in a changing environment," Tech. Rep., 2011.

[24] AEMO, "Final report-queensland and south australia system separation on 25 august 2018," *AEMO Information & Support Hub, Tech. Rep., Australia*, 2019.

[25] RG-CE System Protection & Dynamics Sub Group, “Frequency stability evaluation criteria for the synchronous zone of continental europe,” ENTSO-E, Tech. Rep., 2016.

[26] AEMO, “Maintaining power system security with high penetrations of wind and solar generation,” Tech. Rep., October 2019.

[27] ERCOT, “Future ancillary services in ercot,” Electric Reliability Council of Texas, Tech. Rep., 2013.

[28] EirGrid and SONI, “All island tso facilitation of renewables studies,” *Dublin, Ireland*, 2010.

[29] Hawaii Natural Energy Institute, “Development of real-time closed-loop control algorithms for grid-scale battery energy storage systems,” August 2014.

[30] P. Tielens and D. Van Hertem, “The relevance of inertia in power systems,” *Renewable and Sustainable Energy Reviews*, vol. 55, pp. 999–1009, 2016.

[31] D. Groß and F. Dörfler, “On the steady-state behavior of low-inertia power systems,” *IFAC-PapersOnLine*, vol. 50, no. 1, pp. 10 735–10 741, 2017, 20th IFAC World Congress.

[32] F. Milano, F. Dörfler, G. Hug, D. J. Hill, and G. Verbič, “Foundations and challenges of low-inertia systems (invited paper),” in *2018 Power Systems Computation Conference (PSCC)*, June 2018, pp. 1–25.

[33] P. V. Brogan, R. J. Best, D. J. Morrow, K. McKinley, and M. L. Kubik, “Effect of bess response on frequency and rocof during underfrequency transients,” *IEEE Transactions on Power Systems*, vol. 34, no. 1, pp. 575–583, Jan 2019.

[34] A. Adrees, J. V. Milanović, and P. Mancarella, “Effect of inertia heterogeneity on frequency dynamics of low-inertia power systems,” *IET Generation, Transmission Distribution*, vol. 13, no. 14, pp. 2951–2958, 2019.

[35] U. Datta, A. Kalam, and J. Shi, “The relevance of large-scale battery energy storage (bes) application in providing primary frequency control with increased wind energy penetration,” *Journal of Energy Storage*, vol. 23, pp. 9 – 18, 2019.

[36] M. Paolone, T. Gaunt, X. Guillaud, M. Liserre, S. Meliopoulos, A. Monti, T. Van Cutsem, V. Vittal, and C. Vournas, “Fundamentals of power systems modelling in the presence of converter-interfaced generation,” *Electric Power Systems Research*, vol. 189, p. 106811, 2020.

[37] A. Mehrizi-Sani and R. Iravani, “Potential-function based control of a microgrid in islanded and grid-connected modes,” *IEEE Transactions on Power Systems*, vol. 25, no. 4, pp. 1883–1891, Nov 2010.

[38] J. Rocabert, A. Luna, F. Blaabjerg, and P. Rodríguez, “Control of power converters in ac microgrids,” *IEEE Transactions on Power Electronics*, vol. 27, no. 11, pp. 4734–4749, Nov 2012.

[39] M. Langwasser, G. De Carne, M. Liserre, and M. Biskoping, “Primary frequency regulation using hvdc terminals controlling voltage dependent loads,” *IEEE Transactions on Power Delivery*, vol. 36, no. 2, pp. 710–720, 2021.

[40] M. Raza, E. Prieto-Araujo, and O. Gomis-Bellmunt, “Small-signal stability analysis of offshore ac network having multiple vsc-hvdc systems,” *IEEE Transactions on Power Delivery*, vol. 33, no. 2, pp. 830–839, 2018.

[41] B. Pawar, E. I. Batzelis, S. Chakrabarti, and B. C. Pal, “Grid-forming control for solar pv systems with power reserves,” *IEEE Transactions on Sustainable Energy*, vol. 12, no. 4, pp. 1947–1959, 2021.

[42] Y. Jiao and H. Nian, “Grid-forming control for dfig based wind farms to enhance the stability of lcc-hvdc,” *IEEE Access*, vol. 8, pp. 156 752–156 762, 2020.

[43] J. L. R. Amenedo, S. A. Gómez, J. Alonso-Martinez, and M. G. De Armas, “Grid-forming converters control based on the reactive power synchronization method for renewable power plants,” *IEEE Access*, vol. 9, pp. 67 989–68 007, 2021.

[44] J. Z. Zhou, H. Ding, S. Fan, Y. Zhang, and A. M. Gole, “Impact of short-circuit ratio and phase-locked-loop parameters on the small-signal behavior of a vsc-hvdc converter,” *IEEE Transactions on Power Delivery*, vol. 29, no. 5, pp. 2287–2296, 2014.

[45] R. Rosso, M. Andresen, S. Engelken, and M. Liserre, “Analysis of the interaction among power converters through their synchronization mechanism,” *IEEE Transactions on Power Electronics*, vol. 34, no. 12, pp. 12 321–12 332, 2019.

[46] R. Rosso, S. Engelken, and M. Liserre, “Robust stability investigation of the interactions among grid-forming and grid-following converters,” *IEEE Journal of Emerging and Selected Topics in Power Electronics*, vol. 8, no. 2, pp. 991–1003, 2020.

[47] P. Unruh, M. Nuschke, P. Strauß, and F. Welck, “Overview on grid-forming inverter control methods,” *Energies*, vol. 13, no. 10, 2020.

[48] J. Matevosyan, B. Badrzadeh, T. Prevost, E. Quitmann, D. Ramasubramanian, H. Urdal, S. Achilles, J. MacDowell, S. H. Huang, V. Vital, J. O’Sullivan, and R. Quint, “Grid-forming inverters: Are they the key for high renewable penetration?” *IEEE Power and Energy Magazine*, vol. 17, no. 6, pp. 89–98, 2019.

[49] J. Driesen and K. Visscher, “Virtual synchronous generators,” in *2008 IEEE Power and Energy Society General Meeting - Conversion and Delivery of Electrical Energy in the 21st Century*, 2008, pp. 1–3.

[50] J. Liu, Y. Miura, and T. Ise, “Comparison of dynamic characteristics between virtual synchronous generator and droop control in inverter-based distributed generators,” *IEEE Transactions on Power Electronics*, vol. 31, no. 5, pp. 3600–3611, 2016.

[51] B. Li and L. Zhou, “Power decoupling method based on the diagonal compensating matrix for vsg-controlled parallel inverters in the microgrid,” *Energies*, vol. 10, no. 12, 2017.

[52] H. Beck and R. Hesse, “Virtual synchronous machine,” in *2007 9th International Conference on Electrical Power Quality and Utilisation*, 2007, pp. 1–6.

[53] M. Yu, A. J. Roscoe, C. D. Booth, A. Dysko, R. Ierna, J. Zhu, N. Grid, and H. Urdal, “Use of an inertia-less virtual synchronous machine within future power networks with high penetrations of converters,” in *2016 Power Systems Computation Conference (PSCC)*, 2016, pp. 1–7.

[54] Y. Chen, R. Hesse, D. Turschner, and H. Beck, “Improving the grid power quality using virtual synchronous machines,” in *2011 International Conference on Power Engineering, Energy and Electrical Drives*, 2011, pp. 1–6.

[55] Q. Zhong and G. Weiss, “Synchronverters: Inverters that mimic synchronous generators,” *IEEE Transactions on Industrial Electronics*, vol. 58, no. 4, pp. 1259–1267, 2011.

[56] R. Rosso, J. Cassoli, G. Buticchi, S. Engelken, and M. Liserre, “Robust stability analysis of lcl filter based synchronverter under different grid conditions,” *IEEE Transactions on Power Electronics*, vol. 34, no. 6, pp. 5842–5853, 2019.

[57] M. Guerrero, L. G. de Vicuna, J. Matas, M. Castilla, and J. Miret, “A wireless controller to enhance dynamic performance of parallel inverters in distributed generation systems,” *IEEE Transactions on Power Electronics*, vol. 19, no. 5, pp. 1205–1213, 2004.

[58] H2020 MIGRATE Project,WP3, “Control and operation of a grid with 100 converter-based devices, Deliverable 3.2: Local control and simulation tools for large transmission systems,” available online https://www.h2020-migrate.eu/.

[59] E. Rokrok, T. Qoria, A. Bruyere, B. Francois, and X. Guillaud, “Classification and dynamic assessment of droop-based grid-forming control schemes: Application in hvdc systems,” *Electric Power Systems Research*, vol. 189, p. 106765, 2020.

[60] D. Raisz, T. T. Thai, and A. Monti, “Power control of virtual oscillator controlled inverters in grid-connected mode,” *IEEE Transactions on Power Electronics*, vol. 34, no. 6, pp. 5916–5926, 2019.

[61] T. T. Thai, D. Raisz, A. Monti, F. Ponci, and A. Ahmadifar, “Voltage harmonic reduction using virtual oscillator based inverters in islanded microgrids,” in *2018 18th International Conference on Harmonics and Quality of Power (ICHQP)*, 2018, pp. 1–6.

[62] T. Qoria, E. Rokrok, A. Bruyere, B. François, and X. Guillaud, "A pll-free grid-forming control with decoupled functionalities for high-power transmission system applications," *IEEE Access*, vol. 8, pp. 197 363–197 378, 2020.

[63] "IEEE guide for the application of protective relays used for abnormal frequency load shedding and restoration," *IEEE Std C37.117-2007*, pp. 1–55, Aug 2007.

[64] R. d Silva, "Review of aemo's pscad modelling of the power system in south australia," *Power Systems Consultants, Final JA6921*, 2017.

[65] AEMO, "Final report–queensland and south australia system separation on 25 august 2018," *AEMO Information & Support Hub, Tech. Rep., Australia*, 2019.

[66] J. NERC and W. S. Report, "900 mw fault induced solar photovoltaic resource interruption disturbance report," February 2017.

[67] B. Delfino, S. Massucco, A. Morini, P. Scalera, and F. Silvestro, "Implementation and comparison of different under frequency load-shedding schemes," in *2001 Power Engineering Society Summer Meeting*, vol. 1, July 2001, pp. 307–312 vol.1.

[68] "IEEE guide for the application of protective relays used for abnormal frequency load shedding and restoration," *IEEE Std C37.117-2007*, pp. 1–55, Aug 2007.

[69] ENTSO-E, "Technical background and recommendations for defence plans in the continental Europe synchronous area," in *Tech. Rep.*, 2010.

[70] J. R. Jones and W. D. Kirkland, "Computer algorithm for selection of frequency relays for load shedding," *IEEE Computer Applications in Power*, vol. 1, no. 1, pp. 21–25, Jan 1988.

[71] F. Ceja-Gomez, S. S. Qadri, and F. D. Galiana, "Under-frequency load shedding via integer programming," *IEEE Transactions on Power Systems*, vol. 27, no. 3, pp. 1387–1394, Aug 2012.

[72] M. Karimi, P. Wall, H. Mokhlis, and V. Terzija, "A new centralized adaptive underfrequency load shedding controller for microgrids based on a distribution state estimator," *IEEE Transactions on Power Delivery*, vol. 32, no. 1, pp. 370–380, Feb 2017.

[73] J. Tang, J. Liu, F. Ponci, and A. Monti, "Adaptive load shedding based on combined frequency and voltage stability assessment using synchrophasor measurements," *IEEE Trans on Pow Sys*, vol. 28, no. 2, pp. 2035–2047, May 2013.

[74] A. Derviškadić, Y. Zuo, G. Frigo, and M. Paolone, "Under frequency load shedding based on pmu estimates of frequency and rocof," in *2018 IEEE PES Innovative Smart Grid Technologies Conference Europe (ISGT-Europe)*, 2018, pp. 1–6.

[75] M. Ghaderi Darebaghi and T. Amraee, "Dynamic multi-stage under frequency load shedding considering uncertainty of generation loss," *IET Generation, Transmission Distribution*, vol. 11, no. 13, pp. 3202–3209, 2017.

[76] T. Amraee, M. G. Darebaghi, A. Soroudi, and A. Keane, "Probabilistic under frequency load shedding considering RoCoF relays of distributed generators," *IEEE Transactions on Power Systems*, vol. 33, no. 4, pp. 3587–3598, July 2018.

[77] C. Zhao, E. Mallada, S. Low, and J. Bialek, "A unified framework for frequency control and congestion management," in *2016 Power Systems Computation Conference (PSCC)*, June 2016, pp. 1–7.

[78] "Ieee guide for the application of protective relays used for abnormal frequency load shedding and restoration," *IEEE Std C37.117-2007*, pp. 1–55, 2007.

[79] G. Frigo, A. Derviškadić, Y. Zuo, and M. Paolone, "Pmu-based rocof measurements: Uncertainty limits and metrological significance in power system applications," *IEEE Transactions on Instrumentation and Measurement*, vol. 68, no. 10, pp. 3810–3822, 2019.

[80] H. Bevrani, G. Ledwich, and J. J. Ford, "On the use of df/dt in power system emergency control," in *2009 IEEE/PES Pow Sys Conf*, March 2009, pp. 1–6.

[81] L. Sigrist, "A UFLS scheme for small isolated power systems using rate-of-change of frequency," *IEEE Trans on Pow Sys*, vol. 30, no. 4, pp. 2192–2193, July 2015.

[82] C. P. Reddy, S. Chakrabarti, and S. C. Srivastava, "A sensitivity-based method for under-frequency load-shedding," *IEEE Transactions on Power Systems*, vol. 29, no. 2, pp. 984–985, March 2014.

[83] A. Derviškadić, Y. Zuo, G. Frigo, and M. Paolone, "Under frequency load shedding based on PMU estimates of frequency and ROCOF," in *2018 IEEE ISGT Europe*, Oct 2018, pp. 1–6.

[84] Y. Zuo, M. Paolone, and F. Sossan, "Effect of voltage source converters with electrochemical storage systems on dynamics of reduced-inertia bulk power grids," *Electric Power Systems Research*, vol. 189, p. 106766, 2020.

[85] R. Byerly, D. Sherman, and R. Bennon, "Phase II: frequency domain analysis of low-frequency oscillations in large electric power systems. Volume 1." Westinghouse Electric Corp., Pittsburgh, PA (USA). Advanced Systems, Tech. Rep., 1982.

[86] R. Ramos, I. Hiskens *et al.*, "Benchmark systems for small-signal stability analysis and control," IEEE Power and Energy Society, Tech. Rep. PES-TR18, August 2015.

[87] DESL-EPFL, "Extension of the IEEE 39-bus Test Network for the Study of Fundamental Dynamics of Modern Power System," 2019, Accessed on: 11/8/2021. [Online]. Available: https://github.com/DESL-EPFL/Extension-of-the-IEEE-39-bus-Test-Networkfor-the-Study-of-Fundamental-Dynamicsof-Modern-Power-System.git

[88] "Ieee guide for synchronous generator modeling practices and applications in power system stability analyses," *IEEE Std 1110-2002 (Revision of IEEE Std 1110-1991)*, pp. 1–72, 2003.

[89] "Determination of synchronous machine stability study models. volume 1," Westinghouse Electric Corp., Pittsburgh, PA (USA). Advanced Systems, Tech. Rep., 1981.

[90] "Determination of synchronous machine stability study models. volume 2," Westinghouse Electric Corp., Pittsburgh, PA (USA). Advanced Systems, Tech. Rep., 1981.

[91] "Dynamic models for steam and hydro turbines in power system studies," *IEEE Transactions on Power Apparatus and Systems*, no. 6, pp. 1904–1915, 1973.

[92] P. Kundur, N. J. Balu, and M. G. Lauby, *Power system stability and control.* McGraw-hill New York, 1994, vol. 7.

[93] P. Pourbeik *et al.*, "Dynamic models for turbine-governors in power system studies," *IEEE Task Force on Turbine-Governor Modeling*, 2013.

[94] "Ieee guide for the application of turbine governing systems for hydroelectric generating units - redline," *IEEE Std 1207-2011 (Revision to IEEE Std 1207-2004) - Redline*, pp. 1–139, June 2011.

[95] "Hydraulic turbine and turbine control models for system dynamic studies," *IEEE Transactions on Power Systems*, vol. 7, no. 1, pp. 167–179, Feb 1992.

[96] "Ieee draft recommended practice for excitation system models for power system stability studies," *IEEE P421.5/D38*, pp. 1–202, Jan 2015.

[97] C. Dufour and J. Belanger, "A real-time simulator for doubly fed induction generator based wind turbine applications," in *2004 IEEE 35th APESC*, vol. 5, June 2004, pp. 3597–3603.

[98] R. Pena, J. C. Clare, and G. M. Asher, "Doubly fed induction generator using back-to-back pwm converters and its application to variable-speed wind-energy generation," *IEE Proceedings - Electric Power Applications*, vol. 143, no. 3, pp. 231–241, May 1996.

[99] D.-E. Kim and M. A. El-Sharkawi, "Dynamic equivalent model of wind power plant using an aggregation technique," *IEEE Transactions on Energy Conversion*, vol. 30, no. 4, pp. 1639–1649, 2015.

[100] "Load representation for dynamic performance analysis (of power systems)," *IEEE Trans on Power System*, vol. 8, no. 2, pp. 472–482, May 1993.

[101] F. Sossan, E. Namor, R. Cherkaoui, and M. Paolone, "Achieving the dispatchability of distribution feeders through prosumers data driven forecasting and model predictive control of electrochemical storage," *IEEE Transaction on Sustainable Energy*, vol. 7, no. 4, pp. 1762–1777, Oct 2016.

[102] E. Namor, F. Sossan, E. Scolari, R. Cherkaoui, and M. Paolone, "Experimental assessment of the prediction performance of dynamic equivalent circuit models of grid-connected battery energy storage systems," in *IEEE ISGT*, 2018.

[103] G. Denis, T. Prevost, P. Panciatici, X. Kestelyn, F. Colas, and X. Guillaud, "Improving robustness against grid stiffness, with internal control of an ac voltage-controlled vsc." in *IEEE PESGM*, July 2016, pp. 1–5.

[104] ENTSO-E, "Network code for requirements for grid connection applicable to all generators," Tech. Rep., June 2012.

[105] S. Golestan, J. M. Guerrero, and J. C. Vasquez, "Three-phase plls: A review of recent advances," *IEEE Transactions on Power Electronics*, vol. 32, no. 3, pp. 1894–1907, 2017.

[106] S. Golestan, M. Ramezani, J. M. Guerrero, F. D. Freijedo, and M. Monfared, "Moving average filter based phase-locked loops: Performance analysis and design guidelines," *IEEE Transactions on Power Electronics*, vol. 29, no. 6, pp. 2750–2763, 2014.

[107] Y. Zuo, Z. Yuan, F. Sossan, A. Zecchino, R. Cherkaoui, and M. Paolone, "Performance assessment of grid-forming and grid-following converter-interfaced battery energy storage systems on frequency regulation in low-inertia power grids," *Sustainable Energy, Grids and Networks*, vol. 27, p. 100496, 2021.

[108] A. Z. Amin, "Renewable energy prospects for the european union," International Renewable Energy Agency (IRENA) and European Commission, Tech. Rep., Feb 2018.

[109] P. Mancarella, S. Puschel, L. Zhang, H. Wang, M. Brear, T. Jones, M. Jeppesen, R. Batterham, R. Evans, and I. Mareels, "Power system security assessment of the future national electricity market," *University of Melbourne*, 2017.

[110] S. Camal, A. Michiorri, and G. Kariniotakis, "Optimal offer of automatic frequency restoration reserve from a combined pv/wind virtual power plant," *IEEE Transaction on Power System*, vol. 33, no. 6, pp. 6155–6170, 2018.

[111] S. Camal, A. Michiorri, and G. Kariniotakis, "Forecasting Extremes of Aggregated Production from a RES Virtual Power Plant," in *Proceedings of the Wind Energy Science Conference 2019*. Cork, Ireland: EAWE - European Academy of Wind Energy, Jun. 2019.

[112] L. Zanni, A. Derviškadić, M. Pignati, C. Xu, P. Romano, R. Cherkaoui, A. Abur, and M. Paolone, "Pmu-based linear state estimation of lausanne subtransmission network: Experimental validation," in *21st PSCC*, July 2020.

[113] F. Abbaspourtorbati and M. Zima, "The swiss reserve market: Stochastic programming in practice," *IEEE Transactions on Power Systems*, vol. 31, no. 2, pp. 1188–1194, 2016.

[114] J. Abrell, "The swiss wholesale electricity market," Swiss Competence Center for Energy Research, Tech. Rep., May 2016.

[115] ENTSO-E, "Continental europe operation handbook," OpHB-Team, Tech. Rep., 2016.

[116] A. A. Khatir, R. Cherkaoui, and M. Zima, "Literature survey on fundamental issues of frequency control reserve (fcr) provision," *Swiss Electric Research*, 2010.

[117] ENTSO-E, "Policy 1 – load-frequency control and performance," UCTE Operation Handbook, OpHB-Team, Tech. Rep., 2016.

[118] Power System Dynamic Performance Committee and others, "Dynamic models for turbine-governors in power system studies," *IEEE Power & Energy Society*, 2013.

[119] P. Romano, M. Pignati, and M. Paolone, "Integration of an IEEE Std. C37.118 compliant PMU into a real-time simulator," in *2015 IEEE Eindhoven PowerTech*, June 2015, pp. 1–6.

[120] Y. Zuo, A. Derviškadić, and M. Paolone, "Opf-driven under frequency load shedding inlow-inertia power grids hosting large-scalebattery energy storage systems," in *2021 IEEE Madrid PowerTech*, June 2021, pp. 1–6.

[121] Q. Walger, Y. Zuo, A. Derviškadić, G. Frigo, and M. Paolone, "Opf-based under frequency load shedding predicting the dynamic frequency trajectory," *Electric Power Systems Research*, vol. 189, p. 106748, 2020.

[122] AEMO, "Black system south australia 28 september 2016."

[123] LSPOWER, " LS Power Energizes Largest Battery Storage Project in the World, The 250 MW Gateway Project in California," 2020, Accessed on:11/8/2021. [Online]. Available: https://www.lspower.com/

[124] L. Zanni, A. Derviškadić, M. Pignati, C. Xu, P. Romano, R. Cherkaoui, A. Abur, and M. Paolone, "PMU-based linear state estimation of lausanne subtransmission network: Experimental validation," *Electric Power Systems Research (EPSR), special issue of the 2020 Power Systems Computation Conference (PSCC)*, pp. 1–7, June 2020.

[125] A. Derviškadić, P. Romano, M. Pignati, and M. Paolone, "Architecture and experimental validation of a low-latency phasor data concentrator," *IEEE Transactions on Smart Grid*, vol. 9, no. 4, pp. 2885–2893, July 2018.

[126] M. Paolone, J.-Y. L. Boudec, S. Sarri, and L. Zanni, *Advances in Power System Modelling, Control and Stability Analysis.* F. Milano, Ed. Edison, NJ, USA: IET, 2015, ch. 6: Static and recursive PMU-based state estimation processes for transmission and distribution power grids.

[127] European Commission, "Establishing a guideline on electricity transmission system operation," *Official Journal of the European Union*, August 2017.

[128] ENTSO-E, "Technical background for the low frequency demand disconnection requirements," European Network of Transmission System Operators for Electricity, Tech. Rep., 2014.

[129] F. Saccomanno, *Electric Power Systems: Analysis and Control.* Wiley-IEEE Press, 2003, ch. 4: Dynamic Behavior of the Synchronous Machine.

[130] F. Conte, S. Massucco, M. Paolone, G. P. Schiapparelli, F. Silvestro, and Y. Zuo, "Frequency stability assessment of modern power systems: Models definition and parameters identification," *Sustainable Energy, Grids and Networks*, vol. 23, p. 100384, 2020.

[131] "Standard load models for power flow and dynamic performance simulation," *IEEE Transactions on Power Systems*, vol. 10, no. 3, pp. 1302–1313, Aug 1995.

[132] K. Christakou, J. Y. Le Boudec, M. Paolone, and D. Tomozei, "Efficient computation of sensitivity coefficients of node voltages and line currents in unbalanced radial electrical distribution networks," *IEEE Transactions on Smart Grid*, vol. 4, no. 2, pp. 741–750, June 2013.

[133] Y. Zuo, G. Frigo, A. Derviškadić, and M. Paolone, "Impact of synchrophasor estimation algorithms in ROCOF-based under-frequency load-shedding," *IEEE Transactions on Power Systems*, 2019.

[134] "IEEE Standard for Synchrophasor Measurements for Power Systems," *IEEE Std C37.118.1-2011 (Revision of IEEE Std C37.118-2005)*, pp. 1–61, Dec 2011.

[135] "IEEE Standard for Synchrophasor Measurements for Power Systems – Amendment 1: Modification of Selected Performance Requirements," *IEEE Std C37.118.1a-2014 (Amendment to IEEE Std C37.118.1-2011)*, pp. 1–25, April 2014.

[136] A. Derviškadić, P. Romano, and M. Paolone, "Iterative-interpolated dft for synchrophasor estimation: A single algorithm for p- and m-class compliant pmus," *IEEE Transactions on Instrumentation and Measurement*, vol. 67, no. 3, pp. 547–558, 2018.

[137] P. Romano and M. Paolone, "Enhanced interpolated-dft for synchrophasor estimation in fpgas: Theory, implementation, and validation of a pmu prototype," *IEEE Trans on Instr and Meas*, vol. 63, no. 12, pp. 2824–2836, Dec 2014.

[138] M. Bertocco, G. Frigo, C. Narduzzi, C. Muscas, and P. A. Pegoraro, "Compressive sensing of a taylor-fourier multifrequency model for synchrophasor estimation," *IEEE Trans on Instr and Meas*, vol. 64, no. 12, pp. 3274–3283, Dec 2015.

[139] W. Uijlings and J. Timpert, "Rocof alternative solutions technology assessment," *DNV GL Energy Advisory*, 2015.

[140] A. G. Phadke and B. Kasztenny, "Synchronized phasor and frequency measurement under transient conditions," *IEEE Trans on Pow Del*, vol. 24, no. 1, pp. 89–95, Jan 2009.

[141] A. J. Roscoe and al., "The case for redefinition of frequency and ROCOF to account for AC power system phase steps," in *2017 IEEE AMPS*, Sept 2017, pp. 1–6.

[142] G. Frigo, D. Colangelo, A. Derviškadić, M. Pignati, C. Narduzzi, and M. Paolone, "Definition of accurate reference synchrophasors for static and dynamic characterization of pmus," *IEEE Trans on Instrum and Meas*, vol. 66, no. 9, pp. 2233–2246, Sep. 2017.

[143] W. Dickerson, “Effect of PMU analog input section performance on frequency and ROCOF estimation error,” in *2015 IEEE AMPS*, Sept 2015, pp. 31–36.

[144] A. Riepnieks and H. Kirkham, “Rate of change of frequency measurement,” in *2016 57th International Scientific Conference on Power and Electrical Engineering of Riga Technical University (RTUCON)*, Oct 2016, pp. 1–5.

[145] A. Derviškadić, G. Frigo, and M. Paolone, “Beyond phasors: Modeling of power system signals using the hilbert transform,” *IEEE Transactions on Power Systems*, vol. 35, no. 4, pp. 2971–2980, 2020.

[146] I. Kamwa, S. R. Samantaray, and G. Joos, “Wide frequency range adaptive phasor and frequency PMU algorithms,” *IEEE Trans on Smart Grid*, vol. 5, no. 2, pp. 569–579, March 2014.

[147] Y. Wang, I. R. Pordanjani, W. Li, W. Xu, and E. Vaahedi, “Strategy to minimise the load shedding amount for voltage collapse prevention,” *IET Generation, Transmission Distribution*, vol. 5, no. 3, pp. 307–313, March 2011.

[148] ENTSO-E, “Rate of change of frequency (ROCOF) withstand capability,” Tech. Rep., January 2018.

[149] GE Energy, “Analysis of wind generation impact on ercot ancillary services requirements,” Tech. Rep., March 2008.

[150] K. Coughlin and J. H. Eto, “Analysis of wind power and load data at multiple time scales,” Lawrence Berkeley National Laboratory (LBNL), Berkeley, CA (United States), Tech. Rep., 2010.

[151] T. Sadamoto, A. Chakrabortty, T. Ishizaki, and J. Imura, “Dynamic modeling, stability, and control of power systems with distributed energy resources: Handling faults using two control methods in tandem,” *IEEE Control Systems Magazine*, vol. 39, no. 2, pp. 34–65, April 2019.

[152] G. Frigo, A. Derviškadić, Y. Zuo, A. Bach, and M. Paolone, “Taylor-fourier pmu on a real-time simulator: Design, implementation and characterization,” in *2019 IEEE Milan PowerTech*, 2019, pp. 1–6.

[153] “Ieee guide: Test procedures for synchronous machines,” *IEEE Std 115-1983*, pp. 1–90, Sep. 1983.

[154] J. Feltes, V. Koritarov, L. Guzowski, Y. Kazachkov, B. Lam, C. Grande-Moran, G. Thomann, L. Eng, B. Trouille, P. Donalek *et al.*, “Review of existing hydroelectric turbine-governor simulation models,” Argonne National Lab.(ANL), Argonne, IL (United States), Tech. Rep., 2013.

[155] A. Derviškadić, P. Romano, M. Pignati, and M. Paolone, "Architecture and experimental validation of a low-latency phasor data concentrator," *IEEE Trans on Smart Grid*, vol. 9, no. 4, pp. 2885–2893, July 2018.

[156] Opal-RT technologies Inc, *RT-LAB software, User Guide*, OPAL-RT, Accessed on: 11/8/2021. [Online]. Available: https://www.opal-rt.com

[157] H. W. Dommel, "Digital computer solution of electromagnetic transients in single-and multiphase networks," *IEEE Transactions on Power Apparatus and Systems*, vol. PAS-88, no. 4, pp. 388–399, April 1969.

[158] M. Chen and G. Rincon-Mora, "Accurate electrical battery model capable of predicting runtime and i-v performance," *IEEE Transactions on Energy Conversion*, vol. 21, June 2006.

[159] B. Y. Liaw, G. Nagasubramanian, R. G. Jungst, and D. H. Doughty, "Modeling of lithium ion cells—a simple equivalent-circuit model approach," *Solid State Ionics*, vol. 175, 2004.

[160] C. Dufour, J. Mahseredjian, and J. Belanger, "A combined state-space nodal method for the simulation of power system transients," *IEEE Transactions on Power Delivery*, vol. 26, no. 2, pp. 928–935, April 2011.

YIHUI ZUO

PERSONAL DETAILS

Date of birth: 17/01/1992

Native Place: Sichuan, China

Phone: +41 78 679 95 52

Email: yihui.zuo@eplf.ch

EDUCATION

EPFL - École Polytechnique Fédérale de Lausanne May 2017 - Present
PhD in Electrical Engineering, Distributed Electrical Systems Laboratory *Lausanne, Switzerland*

- Thesis title "Impact of Battery Energy Storage Systems on the Dynamic Behavior of Low-inertia Power Grids" (supervisor: Prof. Mario Paolone, co-supervisor: Prof. Fabrizio Sossan). The Thesis has been partially financed by the H2020 project "Optimal System-Mix Of flexibility Solution for European electricity" (OSMOSE).

North China Electric Power University September 2013 - March 2016
Master in Electrical Engineering *Beijing, China*

- Thesis title "Modulation Control Strategy Research on Large-Scale Wind Power Transmission with HVDC" (supervisor: Prof. Minxiao Han).
Overall GPA: 92.2/100

North China Electric Power University September 2009 - July 2013
Bachelor in Electrical Engineering *Beijing, China*

Overall GPA: 3.8/4

SELECTED PUBLICATIONS

1. Y. Zuo, Z. Yuan, F. Sossan, A. Zecchino, R. Cherkaoui, M. Paolone, "Performance Assessment of Grid-forming and Grid-following Converter-interfaced Battery Energy Storage Systems on Frequency Regulation in Low-inertia Power Grids," Sustainable Energy, Grids and Networks, vol. 27, p. 100496, 2021.
2. Y. Zuo, M. Paolone, F. Sossan, "Effect of Voltage Source Converters with Electrochemical Storage Systems on Dynamics of Reduced-inertia Bulk Power Grids," Electric Power Systems Research, vol. 189, p. 106766, 2020.
3. Y. Zuo, G. Frigo, A. Derviškadić, M. Paolone, "Impact of Synchrophasor Estimation Algorithms in ROCOF-based Under-frequency Load-Shedding," IEEE Transactions on Power Systems, 2019.

Journal papers

1. Y. Zuo, Z. Yuan, F. Sossan, A. Zecchino, R. Cherkaoui, M. Paolone, "Performance Assessment of Grid-forming and Grid-following Converter-interfaced Battery Energy Storage Systems on Frequency Regulation in Low-inertia Power Grids," Sustainable Energy, Grids and Networks, vol. 27, p. 100496, 2021.

2. Y. Zuo, M. Paolone, F. Sossan, “Effect of Voltage Source Converters with Electrochemical Storage Systems on Dynamics of Reduced-inertia Bulk Power Grids,” Electric Power Systems Research, vol. 189, p. 106766, 2020.
3. Q.Walger, Y. Zuo, A. Derviškadić, G. Frigo, M. Paolone, “OPF-based Under Frequency Load Shedding Predicting the Dynamic Frequency Trajectory,” Electric Power Systems Research, vol. 189, p. 106748, 2020.
4. F. Conte, S. Massucco, M. Paolone, G. Piero Schiapparelli, F. Silvestro, Yihui Zuo, ”Frequency Stability Assessment of Modern Power Systems: Models Definition and Parameters Identification,” Sustainable Energy, Grids and Networks, vol 23, p. 100384, 2020.
5. Y. Zuo, G. Frigo, A. Derviškadić, M. Paolone, “Impact of Synchrophasor Estimation Algorithms in ROCOF-based Under-frequency Load-Shedding,” IEEE Transactions on Power Systems, 2019.
6. G. Frigo, A. Derviškadić, Y. Zuo, M. Paolone, “PMU-Based ROCOF Measurements: Uncertainty Limits and Metrological Significance in Power System Applications,” IEEE Transaction on Instrumentation and Measurements, 2019.

Conference papers

7. Y. Zuo, A. Derviškadić, M. Paolone, “OPF-driven Under Frequency Load Shedding in Low-inertia Power Grids Hosting Large-scale Battery Energy Storage Systems,” in 2021 IEEE Madrid PowerTech, June 2021, pp. 1–6.
8. G. Frigo, A. Derviškadić, Y. Zuo, A. Bach, M. Paolone, “Taylor-fourier PMU on a Real-time Simulator: Design, Implementation and Characterization,” in 2019 IEEE Milan PowerTech, June 2019, pp. 1–6.
9. Y. Zuo, F. Sossan, M. Bozorg, M. Paolone, ”Dispatch and Primary Frequency Control With Electrochemical Storage: A System-wise Verification,” in 2018 IEEE PES Innovative Smart Grid Technologies Conference Europe (ISGT-Europe), 2018, pp. 1-6.
10. A. Derviškadić, Y. Zuo, G. Frigo, M. Paolone, “Under Frequency Load Shedding Based on PMU Estimates of Frequency and ROCOF,” in 2018 IEEE ISGT Europe, Oct 2018, pp. 1–6.

PRESENTATION AT SEMINARS

1. Y. Zuo, A. Derviškadić, M. Paolone,”Prevention of Large-scale Blackouts in Modern Power Systems”, Presented at the 16th International Conference on Critical Information Infrastructures Security, Lausanne, Switzerland, September 27-29, 2021.
2. Y. Zuo, A. Derviškadić, G. Frigo, M. Paolone, ”OPF-driven UFLS application in low-inertia power grids hosting large-scale battery energy storage systems”, Presented at OPAL-RT’s 13th Conference on Real-Time Simulation Innovation, Online Conference, September 16-17, 2021.
3. Y. Zuo, A. Derviškadić, G. Frigo, M. Paolone, ”PMU Measurement for OPF-based UFLS Application”, Presented at OPAL-RT’s 12th Conference on Real-Time Simulation Innovation, Online Conference, June 19, 2020.
4. Y. Zuo, G. Frigo, A. Derviškadić, M. Paolone, ”Inertia-less IEEE 39-bus grid for UFLS applications”, Presented at OPAL-RT’s 11th Conference on Real-Time Simulation Innovation, Aarau, Switzerland, September 17, 2019.

AWARD

Best Poster Award at the 2019 SCCER-FURIES Annual Conference: G. Frigo, A. Derviškadić, Y. Zuo, M. Paolone, "ROCOF-based Under Frequency Load Shedding, October 12st, 2019.

LANGUAGE SKILL

Chinese	Mother tongue
English	Professional proficiency
French	Learner

SUPERVISED STUDENT PROJECT

- Q. Walger, "OPF-based Under Frequency Load Shedding using Phasor Measurement Units," Master semester project, Summer, 2018-2019.
- N. Bornet, "Integration of a Phasor Measurement Unit into a Real-Time Simulator for Harmonic Analysis," Master semester project, Summer, 2018-2019.
- J. Fernandez, "Islanding Tests of Grid-forming and Grid-following Converters in Low-inertia Power Grid," Master thesis project, Summer, 2019-2020.

PEER REVIEWS

- IEEE Transactions on Power Systems
- IEEE Open Access Journal of Power and Energy
- IEEE Power Engineering Letters
- Electric Power systems Research
- International Journal of Electrical Power and Energy Systems
- Sustainable Energy, Grids and Networks